Efficient wave-optical simulations for the modeling of micro-optical elements

Dissertation

zur Erlangung des akademischen Grades
doctor rerum naturalium (Dr. rer. nat.)

vorgelegt dem Rat der Physikalisch-Astronomischen Fakultät der
Friedrich-Schiller-Universität Jena

von M.Sc. Sören Schmidt
geboren am 03.08.1987 in Schleiz

1. Gutachter: Prof. Dr. Herbert Gross, Friedrich-Schiller-Universität Jena

2. Gutachter: Prof. Dr. Karl-Heinz Brenner, Universität Heidelberg

3. Gutachter: apl. Prof. Dr. Uwe Detlef Zeitner, Fraunhofer-Institut für Angewandte Optik und Feinmechanik

Tag der Abgabe: 21.03.2018

Tag der Disputation: 28.06.2018

Effiziente wellenoptische Simulationsmethodiken zur Modellierung mikro-optischer Elemente

Die stetige Entwicklung optischer Technologien hat in vielen Bereichen den modernen technischen Fortschritt geebnet. So ist beispielsweise die Herstellung moderner Computerchips und die Datenübertragung des Internets untrennbar mit der Entwicklung von innovativen Lithografieverfahren und Glasfasernetzwerken verbunden. Darüber hinaus hat die kontinuierliche Weiterentwicklung optischer Fertigungsprozesse es ermöglicht, die Funktionalität optischer Komponenten immer weiter zu erhöhen. Auf Grundlage dieser Entwicklungen können nahezu beliebig komplexe optische Komponenten höchster Qualität realisiert werden. Dies ermöglicht es neuartige Freiheitsgrade in der Auslegung und Konzeption optischer Systeme zu verwenden. Die Herausforderung besteht jedoch darin, diese neuen Möglichkeiten gezielt in der Optimierung optischer Systeme ausnutzen zu können. Dies erfordert die stetige Weiterentwicklung numerischer Simulationswerkzeuge, um diese optischen Systeme zu modellieren, zu charakterisieren und zu designen.

Ein Ziel dieser Arbeit ist es verbesserte numerische Techniken zur Modellierung mikro-optischer Systeme einzuführen und zu diskutieren. Darüber hinaus ist ein weiteres Ziel dieser Arbeit, das Potential dieser verbesserten Simulationsmethoden sowohl zur Charakterisierung als auch dem Design mikro-optischer Komponenten zu untersuchen.

Im ersten Abschnitt der Arbeit wird die zugrundeliegende numerische Methodik vorgestellt. Insbesondere werden Simulationsansätze für mikro-optische Systeme diskutiert. Diese Systeme sind durch charakteristische Strukturgrößen im Bereich von einigen bis zu mehreren hundert Lichtwellenlängen definiert. In diesem Bereich können rigorose Simulationsverfahren, wie beispielsweise die *finite difference time domain method* oder die *rigorously coupled wave analysis*, typischerweise nicht angewendet werden. Die Speicheranforderungen und der Rechenaufwand sind für diese Art von Simulationsszenarien selbst mit heutigen Computerressourcen zu aufwendig. Alternativ müssen approximierende Verfahren verwendet werden, welche effizientere Simulationen ermöglichen.
In einem ersten Schritt werden verschiedene Ansätze eingeführt, analysiert und diskutiert. In einem weiteren Schritt werden vielversprechende Algorithmen gezielt weiterentwickelt, um deren Recheneffizienz zu steigern. Dies kann den Anwendungsbereich der Simulationsmethodiken stark erweitern und eröffnet tiefere Einsichten über die Wechselwirkung von Licht mit mikrostrukturierten Komponenten. Dies ermöglicht die Entwicklung neuartiger Charakterisierungs- und Designansätze für mikro-optische Komponenten, welche im zweiten Hauptteil der Arbeit diskutiert werden. Hierfür, wird im ersten Schritt die Charakterisierung mikro-optischer Komponenten diskutiert. Zum Einem wird das Einschreibeverfahren von Faser-Bragg Gittern analysiert und zum Anderen ein Charakterisierungsverfahren optischer Fasern diskutiert.

Während der Herstellung von Faser-Bragg Gittern können ungewollte Störungen in der Glasmatrix auftreten, welche eine charakteristische und reproduzierbare Symmetrie zeigen. Um ein besseres Verständnis der zugrundeliegenden Ursachen der Störungen zu erhalten, wird der Einschreibevorgang der Faser-Bragg Gitter numerisch modelliert. Auf Grundlage der Simulationsergebnisse kann eine umfassende Erklärung für das Auftreten der Störungen der Glasmatrix gefunden werden und eine Lösungsstrategie entwickelt werden.

Im darauffolgenden Kapitel wird ein zerstörungsfreies Messverfahren zur Charakterisierung optischer Fasern vorgestellt. Dieses Konzept kann prinzipiell in den Herstellungsprozess optischer Fasern integriert werden und damit die Überwachung von Faserparametern ermöglichen. Hierfür wird ein in-line holografisches Messverfahren verwendet und die zu untersuchende Faser mit einem kohärenten Laserstrahl seitlich beleuchtet. Auf einem entfernten Detektor wird die Beugungsantwort der Faser gemessen und ausgewertet. Zusätzlich wird der gesamte Messaufbau numerisch modelliert. Der direkte Vergleich zwischen den Simulationen und den Messungen ermöglicht die Charakterisierung der untersuchten Faser. Auf Grundlage der Simulationen können auch systematische Einflussfaktoren evaluiert werden, welche die Genauigkeit der Charakterisierung beeinflussen. Auf dieser Grundlage können verschiedene methodische Verbesserungen des Messaufbaus realisiert werden.

Im letzten Kapitel der Arbeit wird ein integriertes Strahlformungskonzept vorgestellt, welches komplexe Beleuchtungsverteilungen in einem hochgradig miniaturisierten Ansatz ermöglicht. Hierfür wird eine Freiformfläche designt, welche die Strahlformung der Grundmode der Faser in die gewünschte Zielverteilung ermöglicht. Der optische Designprozess wird gezielt optimiert, um Probleme klassischer diffraktiver Strahlformung zu umgehen. Insbesondere wird die Unterdrückung von Falschlicht der nullten und höheren Beugungsordnungen gezielt analysiert. Die final designten Oberflächen werden mit Hilfe der Multiphotonen Lithografie monolithisch auf der Faserspitze realisiert. Dieser Ansatz ermöglicht die Nutzung von strukturierter Beleuchtung in vorher unzugänglichen Raumregionen, was beispielsweise für endokopische Messverfahren von besonderem Interesse ist.

Contents

Part I

Introduction

The continuous development of optical technologies paves the way for modern technical progress in many different scientific and economic areas. The ability to exchange information across continental boundaries almost at the speed of light is intrinsically linked to the development of fiber-optic networks for data transmission. Alternatively, the observation and detection of gravitational waves requires unprecedented precision to resolve tiny fluctuations in space. These possibilities are exceptionally provided by high-end laser interferometric techniques.
These advancements of modern optical technologies allow to increase the functionality of optical devices. They enable to realize optical components between the very nanoscopic regime and macroscopic scales without symmetries and with extraordinary accuracies. For instance, modern lithography processes enable the realization of intricate nanoscopic structures, which allows to manipulate light on smallest subwavelength scales [1,2]. Moreover, modern fabrication processes, such as femtosecond two-photon direct laser writing even enable 3d-printing of micro-optical structures on arbitrary substrates. This can open up novel avenues in the miniaturization and integration of optical components [3]. Finally, modern diamond turning manufacturing processes allow for the fabrication of large optical components without an underlying rotational symmetry, which opens up the field of freeform optics [4]. While these different fabrication technologies enable the realization of optical components with nearly an arbitrary degree of freedom, the ability to take direct advantage out of these developments is intrinsically linked to profound numerical simulation tools to analyze, model and design these systems. Consequently, these demands trigger the steady development and improvement of algorithms, which advances the optical design process and therewith the functionality of related devices.

In addition, algorithms are no longer just important parts in the toolbox of an optical designer. In particular, the algorithmic post-processing of recorded data is of growing importance for the overall functionality of optical devices. This marks a paradigm shift and algorithmic development work emerges to one of the driving forces of technological progress in optical research and industry. Nowadays, the numerical post-processing of measurements allows either to reduce the complexity of an optical system and/or to increase the quality of gathered information. These ideas are often referred to as computational sensing or -imaging and become state-of-the-art technologies. In particular, every modern camera features digital correction steps not only to improve the quality of images but also to enhance the functionality of the camera itself. For instance, in panoramic imaging a sequence of individual images under different viewing angles are computationally processed and merged to a single panoramic image with a wide field of view. Hence, a respectively simple camera lens is used to mimic the behavior of an expensive and complex wide angle lens. In addition, there also is a strong scientific research focus to go way beyond state-of-the-art concepts and which aims to further reduce the complexity of high performant imaging devices. In particular, modern computational imaging approaches can overcome the necessity of traditional camera lenses at all. Over the years, a huge amount of these so-called lensless imaging concepts emerged [5–9], but they share a similar underlying idea. In each of these cases, no direct image of the scene is captured by the sensor and the requested information is only gathered in an encrypted manner. A subsequent post-processing of these measurements allows to decrypt the respective information by solving the so-called inverse imaging problem.

This is achieved by relying on an underlying physical model to describe the imaging process and a proper calibration of the setup. This conceptual idea has the potential to enable imaging processes that were previously unthinkable. To this end, the ability to look through a frosted glass window, i.e., a translucent surface, is shortly discussed in the following. In this case, inherent scattering processes on the glass surface are likely to destroy any information about the scene behind the window and therewith any recovery of the scene seems impossible. However, this is not the case in reality and the frosted glass window does not destroy the underlying information than rather encrypt it. To be more precise, every individual object point in the scene will produce a distinct speckle pattern behind the window under coherent illumination. One might interpret this speckle pattern as a coherent point spread function of the system. By measuring the entire number of distinct point spread functions one can model the entire image formation process. This allows to solve the inverse imaging problem and therewith enables the reconstruction of the hidden scene by using coherent illumination [10–15]. Thus, looking through a frosted glass window and grasping information as if the window would be transparent actually becomes possible in the framework of computational imaging. This particular example highlights the opportunities, which an algorithmic post-processing of measurements can open up. Consequently, computational sensing is nowadays not only used in the framework of lensless imaging but actually throughout the entire spectrum of optical applications. For instance, in nano-optics the interpretation of measurements is often only possible by relying on subsequent simulations of the entire structure. Moreover, modern microscopic methods to overcome the fundamental resolution limit as defined by Abbe are entirely founded on a computational imaging approach [16–18]. In addition, algorithmic post-processing of measured data forms the basis in holographic imaging approaches [19, 20] and is of essential importance in optical quality assurance and the metrology of optical surfaces [21, 22].
Nevertheless, beside the stunning aspects which become possible by computational imaging concepts, there are still many challenges and there is a high potential to improve the individual approaches. In particular, solutions of the inverse imaging problem are founded on specific models to describe the image formation process. Hence, the overall accuracy is directly influenced by the quality of this underlying model. However, an improvement of the model is a trade off in between its accuracy, i.e., the physical modeling depth, and the computational effort to solve the inverse imaging problem. As a consequence, a refinement is often unfeasible as the rising computational effort becomes too demanding. To overcome these challenges, there is a strong need to improve the algorithms, which model the underlying physical aspects.

It is one aim of this thesis to introduce and to discuss improved numerical techniques to model micro-optical systems. Moreover, it is a second aim of this thesis to also investigate the potential of these improved simulation methodologies to solve inverse problems for the characterization of micro-optical components. In particular, the ability to resolve the origin of glass matrix distortions during fiber Bragg grating inscriptions will be discussed. Moreover, a computational sensing concept to characterize optical fibers will be introduced. Finally, it is a third aim of this thesis to also discuss the design of micro-optical systems. In particular, an

integrated illumination concept is introduced, which can take direct advantage of the abilities provided by two-photon direct laser writing.

The individual numerical modeling techniques, which are considered in this thesis are introduced in part II. In particular, simulations in the micro-optical regime are considered, where feature sizes of the investigated components are in the range of a few up to several hundred times the wavelength of light. In this case, rigorous simulation techniques such as the finite difference time domain method or the rigorously coupled wave analysis can typically not be applied. The memory requirements and the computational effort for these kind of simulation scenarios are too demanding even with nowadays computational resources [23]. To overcome these issues the computational complexity of the simulations needs to be reduced. These aspects are thoroughly discussed in chapter 1 of this thesis, which follows to this introduction. There, a general overview about the different simulation techniques in a micro-optical regime is given. In a first step, suitable approximations are introduced and their validity is discussed. This is the scalar optical approximation and the unidirectional modeling of inhomogeneous media. In a subsequent step, individual state-of-the-art algorithms for micro-optical simulations are introduced. First, this is the thin-element approximation as a combined wave- and geometrical optical model. Then, the wave propagation method and different beam propagation methods are introduced as extended modeling concepts to overcome the restrictions of the thin-element approximation.
In the appending chapter 2, a reformulation of the wave propagation method is introduced, which allows to increase the simulation speed for piecewise homogeneous media significantly. This reformulated algorithm is evaluated in comparison to the beam propagation methods to assess the ability to overcome apparent limitations of the thin-element approximation. In a representative scenario the individual algorithms are compared against rigorous simulations with respect to accuracy, sampling requirements, and computational performance. These insights can provide new opportunities for the modeling of micro-optical structures and are used, for instance, in chapter 4 to establish a computational sensing concept for the characterization of optical fibers. Moreover, to further increase the computational performance of the wave propagation method, it is specialized into a rotationally symmetric formulation to exploit this kind of underlying symmetry. This so-called Hankel-WPM is well suited to analyze e.g. micro-optical lenses and is assessed by evaluating diffractive lenses. On the one hand, this example allows to evaluate the reformulated algorithm. On the other hand, it is of practical importance, as diffractive lens concepts are of indispensable value for the steady miniaturization of optics. Moreover, diffractive influences are assessed, which are not predicted within the TEA formalism. These insights allow for a deeper understanding of diffractive lenses and diffractive optical elements in general. This can pave the way for improved design algorithms, which are discussed detailed in chapter 5. Overall, these improved numerical simulation tools allow to gain deeper insights about micro-optical elements, which can trigger the improvement or even the development of novel applications. These aspects are discussed detailed in part III of this thesis.

Chapter 3 discusses fiber Bragg gratings (FBGs), which are of special importance in integrated sensing concepts [24–26]. In particular, the inscription of FBGs is considered and special emphasis is placed on glass matrix distortions that might occur during their inscription.
FBGs are structural modifications of the refractive index along the optical axis of a fiber. They

allow to tailor the spectral transmission and reflection characteristics of the fiber by carefully realizing specifically designed refractive index profiles along the optical axis. This is achieved by a side illumination technique of the fiber, where an intensity modulated light sheet inscribes these structural modifications into a photosensitive core. However, beside these intended changes of the glass matrix also unwanted modifications can occur, which can influence the mechanical and optical properties of the fiber. These glass matrix defects show a distinct and reproducible symmetry and the origin was not understood in depth. By numerically modeling the FBG inscription process and by comparing these results to microscopic measurements of inscribed fibers, the origin of these glass matrix defects is revealed. These simulations allow for a better understanding of the situation, which even enables the development of a possible solution strategy.

The appending chapter 4 focuses on a non-invasive computational sensing technique to characterize optical fibers. This metrological concept is potentially suited to be integrated into the manufacturing process of optical fibers, which could enable a real-time monitoring of fiber parameters during their manufacturing. To this end, an inline holographic measurement setup is used, where the investigated fiber is side illuminated by a coherent beam. At the position of a distant detector the diffraction response of the fiber is measured and evaluated. In contrast to ordinary in-line holographic measurements, high index contrasts, e.g., between glass and air, are involved in this scenario. As a consequence, usual approximations considered for the evaluation of holographic measurements cannot be applied here. Hence, to overcome these apparent restrictions an alternative evaluation concept is required. Here, simulations of the entire structure are directly compared to the measurements. By changing characteristic parameters of the fiber in the simulations, e.g., the core diameter, an optimal match is examined. The potential and suitability of the approach is examined by investigating and assessing different fibers. Overall, this proposed methodology can overcome the restrictions of conventional evaluation models in diffractive imaging concepts. This is of particular importance for modern holographic measurement principles [20, 27, 28].

Finally, in chapter 5 an integrated beam shaping concept is introduced, which allows to realize complex illumination patterns in a highly integrated approach. To this end, a freeform surface is realized monolithically on the tip of an optical fiber to redistribute the fundamental eigenmode into a desired illumination. A novel design methodology is discussed to overcome apparent limitations in conventional diffractive beam shaping. In particular, the suppression of zeroth order false light and ghost images due to the excitation of higher diffraction orders is examined. The fabrication of these designed micro-optical freeform elements is challenging and the potential of two-photon direct laser writing is assessed to realize these surface profiles with a required accuracy.

Overall, this approach can allow for a high degree of miniaturization of illumination concepts without critical adjustments. In addition, the mechanical flexibility of the fiber is maintained and the approach can enable the application of structured illumination in previously inaccessible domains. These abilities could be of particular importance, for instance, in structured light microscopy, endoscopy, and laser-based material processing.

Part IV summarizes the main results of this thesis in respect to the challenges of optical design and modeling in a micro-optical regime. Fundamental conclusions are drawn, presenting a major step on the route to further increase the functionality of micro-optical systems.

Part II

Numerical Modeling of Micro-Optical Elements

1 Fundamentals

In this chapter the theoretical foundation of the algorithms is introduced, which are used to simulate micro-optical structures within this thesis. The fundamental basis are, of course, Maxwell's Equations which ultimately describe the nature and interaction of light with matter. Their numerical solution results in high computational demands. On the one hand, the simulation volume needs to be discretized, where the wavelength λ defines the characteristic measure. On the other hand, all vectorial field components, namely the three electric and magnetic ones, have to be considered simultaneously. These aspects limit the application of rigorous solutions to respective small simulation volumes even with nowadays standard computational resources. As an example, the widespread Finite-Difference-Time-Domain (FDTD) method is mentioned, which numerically solves Maxwell's Equations on a Cartesian grid in the time-domain [29]. The length scales of the simulation volume are typically in the order of several wavelengths in three dimensions[1]. Alternatively, there exist many other rigorous solution techniques, i.e., the greens-tensor-technique [31] or solvers in the spectral frequency domain [32]. These algorithms are more appropriate for specific scenarios but share similar limitations regarding the simulation volume. To overcome these limitations, the computational complexity of rigorous simulations needs to be reduced. To this end, often underlying symmetries are exploited, which are shortly mentioned in the following. On the one hand, for periodic structures the Fourier-Modal-Method (FMM) or the rigorously coupled wave-analysis (RCWA) are used, which rely on the Bloch-theorem [33]. Then, the simulation of a periodic unit-cell is sufficient to characterize the response of the structure. As a typical example, gratings or periodic meta materials are mentioned here. Furthermore, structures with a translational invariance along one dimension, i.e., the optical axis, are effectively modeled by relying on eigenmode solvers. These algorithms are typically used for nanowires or optical fibers of any kind. Moreover, the interaction of light with rotationally symmetric structures, e.g., core-shell particles, is efficiently described by Mie-theory. The mutual interaction of individual spherical nano particles is modeled by coupled Mie-theory [34]. This approach provides the backbone to simulate, e.g., Huygens meta-surfaces [35]. Nevertheless, the individual simulation techniques are still demanding. In order to decrease the complexity for a numerical simulation, approximations have to be considered within Maxwell's Equations.

In particular, there are two important approximations: On the one hand, the vectorial electromagnetic character of light is neglected. On the other hand, the limit of a vanishing wavelength $\lambda \longrightarrow 0$ is treated. The prior leads to the scalar optical description of light. In this case, it is fundamentally assumed that an optical component does not affect or interact with the polarization state of an incoming beam. This approximation remains mostly valid for micro-optical components. There, characteristic length scales, i.e., changes in the topology of the component, are larger than the considered wavelength of light. It is especially this regime, which will be considered in the following chapter and the entire thesis.
A vanishing wavelength $\lambda \longrightarrow 0$ equals the fundamental limit of geometrical optics where any influence of diffraction is neglected. While this assumption seems to be a strong restriction, it

[1] In the literature simulations with size dimensions of more than 100 wavelengths are reported by relying on several independent and stitched simulations [30]. Nevertheless, the effort for these kind of simulations is high. Special care has to be taken into account to combine the individual fields of the independent simulations.

actually constitutes a valid approximation in many practical cases. Then, the phase of the wave at a specific point is connected to the optical path length of individual rays. In other words, the wavefronts are defined as the surfaces of constant optical path length. Furthermore, the amplitude of the wave is related to the local density of rays at a given point[2]. This allows to interchange between ray- and wave-optical simulations. This connection establishes the foundation of the most important approximation to simulate micro-optical components. Namely, this is the thin-element approximation (TEA). In this framework, a wave is propagated to the position of the element. Then, the impact of the micro-optical component is approximated as an induced phase delay an incoming wavefront is altered. This treatment is founded on a geometric optical viewpoint. As a consequence, any influence of diffraction occurring inside the component is neglected. Then, the retarded wave is propagated further in space. In order to model and simulate micro-optical components with a higher accuracy, extended algorithms are required. It is the aim of this chapter to introduce and discuss these algorithms. In particular, uni-directional algorithms are considered to simulate micro-optical systems. These algorithms consider the evolution of light in an optical system in forward direction only and neglect any kind of backward propagating field components such as reflections. This aspect is in common with classical sequential ray-tracing, where reflected field components are similarly neglected. In addition, diffraction is considered in these algorithms. Hence, they are extended formulations of geometric optical approximations, like the thin-element approximation. Moreover, these algorithms can also be extended by different concepts to also model backward propagating field components [33].

The following chapter will be organized as follows: First, in Sec. 1.1 the formal transition from Maxwell's equations to the scalar optical description will be discussed, while afterwards the unidirectional approach will be introduced. Second, in Sec. 1.2 the thin-element approximation will be derived and be discussed in detail. Finally, in Sec. 1.3 and 1.4 the beam propagation methods (BPM) and the wave propagation method (WPM) will be introduced, which will be considered for extended simulations beyond the thin-element approximation.

1.1 General statement of the problem

1.1.1 Maxwell's equations

Throughout the thesis all simulations are considered in the spectral domain, i.e., for monochromatic light characterized by the angular frequency ω. Therefore, Maxwell's Equations (MWEQ) are introduced in its spectral formulation and the subsequent notations and discussions follow mainly the standard textbooks [40–42]. In the absence of free charges and currents they read as

$$\begin{aligned} \nabla \times \mathbf{E}(\mathbf{r},\omega) &= \;\; i\omega\mathbf{B}(\mathbf{r},\omega)\;, \qquad \nabla \cdot \mathbf{B}(\mathbf{r},\omega) = 0\;, \\ \nabla \times \mathbf{H}(\mathbf{r},\omega) &= -i\omega\mathbf{D}(\mathbf{r},\omega)\;, \qquad \nabla \cdot \mathbf{D}(\mathbf{r},\omega) = 0\;. \end{aligned} \tag{1.1}$$

[2]This statement belongs to conventional ray-tracing programs, i.e., Zemax, where the intensity of a given field is encrypted through the local density of rays. However, there are several extended approaches, i.e., differential ray-tracing [36, 37] or path integration methods [38, 39].

The complex and time dependent electric field, analogue for the remaining field components, is connected to its spectral conjugate via a Fourier-transform pair

$$\begin{aligned} \boldsymbol{\mathcal{E}}(\mathbf{r},t) &= \frac{1}{\sqrt{2\pi}}\int_{-\infty}^{\infty}\mathbf{E}(\mathbf{r},\omega)e^{-i\omega t}d\omega \ , \\ \mathbf{E}(\mathbf{r},\omega) &= \frac{1}{\sqrt{2\pi}}\int_{-\infty}^{\infty}\boldsymbol{\mathcal{E}}(\mathbf{r},t)\ e^{i\omega t}dt \ . \end{aligned}$$

The individual electromagnetic field components are not independent from each other and are connected via material relations specific to a considered problem. At optical frequencies most materials are non-magnetic

$$\mathbf{B}(\mathbf{r},\omega) = \mu_0\mathbf{H}(\mathbf{r},\omega) \ ,$$

where μ_0 is the vacuum permeability. Moreover, only linear, local and isotropic materials will be considered. Then the dielectric response is given as

$$\mathbf{D}(\mathbf{r},\omega) = \epsilon_0\epsilon(\mathbf{r},\omega)\mathbf{E}(\mathbf{r},\omega) \ .$$

Here ϵ_0 denotes the vacuum permittivity and $\epsilon(\mathbf{r},\omega)$ the dielectric function characterizing the specific material. These relations are connected to the refractive index $n(\mathbf{r},\omega)$ of a material via $\epsilon(\mathbf{r},\omega) = n(\mathbf{r},\omega)^2$. Based on these material relations MWEQ reduce to

$$\begin{aligned} \nabla\times\mathbf{E}(\mathbf{r},\omega) = \quad & i\omega\mu_0\mathbf{H}(\mathbf{r},\omega) \ , \quad & \nabla\cdot\mathbf{H}(\mathbf{r},\omega) = 0 \ , \\ \nabla\times\mathbf{H}(\mathbf{r},\omega) = & -i\omega\epsilon_0\epsilon(\mathbf{r},\omega)\mathbf{E}(\mathbf{r},\omega) \ , & \nabla\cdot(\epsilon(\mathbf{r},\omega)\mathbf{E}(\mathbf{r},\omega)) = 0 \ . \end{aligned} \tag{1.2}$$

Relying on the product rules and standard identities of the nabla-operator calculus the MWEQ according Eqn. 1.2 can be transformed into an inhomogeneous wave equation for both the electric and magnetic field components individually. These equations for the electric and magnetic fields read as [43]

$$\Delta\mathbf{E}(\mathbf{r},\omega) + \frac{\omega^2}{c^2}\epsilon(\mathbf{r},\omega)\mathbf{E}(\mathbf{r},\omega) = -\nabla\cdot\left(\frac{\nabla\epsilon(\mathbf{r},\omega)}{\epsilon(\mathbf{r},\omega)}\cdot\mathbf{E}(\mathbf{r},\omega)\right) \ , \tag{1.3}$$

$$\mathbf{H}(\mathbf{r},\omega) + \frac{\omega^2}{c^2}\epsilon(\mathbf{r},\omega)\mathbf{H}(\mathbf{r},\omega) = (\nabla\times\mathbf{H})\times\frac{\nabla\epsilon(\mathbf{r},\omega)}{\epsilon(\mathbf{r},\omega)} \ . \tag{1.4}$$

This approach can reduce the complexity to solve Maxwell's Equations, as in this case only three of the six field components are coupled with each other. In particular, one needs only a solution to either one of these equations. Then, from the knowledge of either the electric or the magnetic field components the respectively missing ones are directly derived relying on Eqns. 1.2. Nevertheless, the right hand side of equations 1.3 and 1.4 still couple the individual electric or magnetic field components. This makes a general solution difficult and only for special cases a further decoupling is possible. These situations are shortly discussed in the following. This is the case for an inhomogeneous medium invariant along one dimension, e.g., $\partial_y\epsilon(x,y,z) = 0$. Then, for an initial field $\mathbf{H} = H\mathbf{e}_y$ the right hand sides of Eqn. 1.4 vanish and reduces to a

Helmholtz equation. Moreover, if the electric field is polarized along the y-dimension $\mathbf{E} = E\mathbf{e}_y$, Eqn. 1.3 similarly reduces to the Helmholtz equation, which is given in this case as

$$\Delta E(x, z, \omega) + \frac{\omega^2}{c^2}\epsilon(x, z, \omega)E(x, z, \omega) = 0 \ . \tag{1.5}$$

These two individual cases are referred to as TM- and TE-polarization respectively. Together they form the complete set of solutions in two dimensions. In other words, every two dimensional incoming field can be decomposed into these two polarization states. Therefore, Maxwell's equations can be solved in two dimensions based on two individual solutions of a scalar Helmholtz equation.

Additionally, Eqn. 1.3 and 1.4 decouple for a constant dielectric permitivity $\epsilon(\mathbf{r}, \omega) = \epsilon$, i.e., a medium characterized by a constant refractive index $n = \sqrt{\epsilon}$. Then, the inhomogeneous wave equation for the electric field components reduces to

$$\Delta\mathbf{E}(\mathbf{r}, \omega) + \frac{\omega^2}{c^2}n^2(\omega)\mathbf{E}(\mathbf{r}, \omega) = 0 \ . \tag{1.6}$$

In this case, no cross-coupling terms are occurring and the individual field components can be treated separately. A complete set of solutions are plane waves $\mathbf{E}(\mathbf{r}, \omega) = \tilde{\mathbf{E}}(\omega)e^{i\mathbf{kr}}$, where the magnitude of the wave number $|\mathbf{k}| = \sqrt{k_x^2 + k_y^2 + k_z^2} = \frac{\omega}{c}n(\omega)$ is fixed. The wavelength λ, i.e., the distance of 2π phase changes along the propagation direction, is connected to the absolute value of the wave vector via $|\mathbf{k}| = k_0 n = \frac{2\pi}{\lambda_0}n$, where k_0 and λ_0 are respectively the wave vector and wavelength in vacuum. Moreover, the individual field components have still to obey the full set of Maxwell's Eqn. 1.2. The requirement of a vanishing divergence of the electric field $\nabla\mathbf{E}(\mathbf{r}, \omega) = 0$ requires the wave vector $\mathbf{k}$ to be orthogonal to the electric field $\mathbf{k} \cdot \mathbf{E} = 0$. Thus, only two of the three electric field components can be chosen independently. Given $\tilde{E}_x$ and $\tilde{E}_y$, the component $\tilde{E}_z$ is uniquely defined by the relation

$$\tilde{E}_z = -\frac{k_x\tilde{E}_x + k_y\tilde{E}_y}{k_z} \ . \tag{1.7}$$

Moreover, also the magnetic field components $\mathbf{H}$ are uniquely defined by exploiting the remaining MWEQ. Thus, only two out of the six electromagnetic field components can be chosen independently. These two individual solutions of the homogeneous space are referred to as the individual polarization states of light. Due to the linearity of the Helmholtz equation, every linear combination of plane waves remains a valid solution of Eqn. 1.6. Therefore, these waveforms provide a set of fundamental eigensolutions in a homogeneous space. To calculate the entire electromagnetic field distribution in space only two field components need to be known in an initial plane, i.e., $E_x(x, y, z_0)$ and $E_y(x, y, z_0)$. Then the field components in a parallel plane at distance Δz are given as

$$\begin{aligned}
\tilde{E}_{x,y}(k_x,k_y,z_0) &= \int E_{x,y}(x,y,z_0)e^{-i(k_x x+k_y y)}dxdy && = \mathcal{F}\left\{E_{x,y}(x,y,z_0)\right\} \ , \\
E_{x,y}(x,y,z_0+\Delta z,\omega) &= \int \tilde{E}_{x,y}(k_x,k_y,z_0)e^{ik_z\Delta z}e^{i(k_x x+k_y y)}dk_x dk_y && = \mathcal{F}^{-1}\left\{\tilde{E}_{x,y}(k_x,k_y,z_0)e^{ik_z\Delta z}\right\} \ , \\
&= \mathcal{F}^{-1}\left\{\mathcal{F}\left\{E_{x,y}(x,y,z_0)\right\}e^{ik_z\Delta z}\right\} && k_z = \sqrt{k_0^2 n^2 - k_x^2 - k_y^2} \ .
\end{aligned} \tag{1.8}$$

Eqns. 1.8 allow to propagate an initial field given in a plane $E_{x,y}(x,y,z=0)$ to an arbitrary distance. This approach is referred to angular spectrum of plane wave decomposition (ASPW) and is efficiently implemented by relying on the numerical fast Fourier transform. To derive the remaining electromagnetic field components the MWEQ are used

$$E_z(\mathbf{r}) = \mathcal{F}^{-1}\left\{\frac{k_x\tilde{E}_x + k_y\tilde{E}_y}{k_z}\right\} \ , \qquad \mathbf{H} = \frac{1}{i\omega\mu_0}\nabla\times\mathbf{E} \ . \tag{1.9}$$

Nevertheless, away from these special cases of a invariant or a homogeneous medium, rigorous solutions to Eqn. 1.3 are difficult to find. The major difficulty is connected to the right hand side of Eqn. 1.3, which couples the electric field components. Therefore, it is preferable to neglect the right hand side of this equation whenever possible. This approximation usually is referred as scalar optics. In a strict sense, this assumption remains valid if the inhomogeneous medium varies slowly, i.e., $\nabla\epsilon(\mathbf{r},\omega) \ll 1$. However, often optical components are piecewise homogeneous, i.e., optical fibers, lenses or nano structured materials. In every of these cases the gradient of the permitivity distribution diverges at the material interfaces and it is hard to judge on the validity to neglect the RHS at all. On the one hand, experience shows us that the eigenmode of a classical optical fiber is described accurate enough by a scalar approach. On the other hand, the interaction of light with nano structured materials needs to be considered on rigorous grounds. Thus, the pertinent question is connected to the conditions a scalar approximation remains valid. In general, this is far from being trivial. To approach an answer to this question an alternate viewpoint is introduced in the following to judge the validity of a scalar approximation. This enables a more intuitive understanding about this situation.

1.1.2 Scalar wave equation

The RHS of Eqn. 1.3 couples the individual electric field components. In general, this affects an initial polarization state of a wave will and it will be changed due to the optical system. Only for the two special cases previously discussed the initial polarization state will be preserved. Thus, the RHS of the equation is referred to as depolarization term in the following. As a consequence, if the change in the polarization of an initial field due to an optical component is sufficiently small, the neglection of the right hand side in Eqn. 1.3 remains valid. This corresponds to two fundamental assumptions:

(*i*) The considered optical system does not show a distinctive response depending upon the incident polarization.

(*ii*) There is no cross coupling between individual polarization components.

Often, the impact of an optical system on the polarization is characterized by the Jones matrix $\hat{J}$. It describes the response of the component onto the initial polarization states, e.g., linearly x- and y-polarized fields $E^{\text{in}}_{x,y}(x, y, z_{\text{in}})$. Then, the modified polarization components of the fields $E^{\text{out}}_{x,y}(x, y, z_{\text{out}})$ are given by

$$\begin{pmatrix} E^{\text{out}}_x(x, y, z_{\text{out}}) \\ E^{\text{out}}_y(x, y, z_{\text{out}}) \end{pmatrix} = \begin{pmatrix} J_{xx}(x, y) & J_{xy}(x, y) \\ J_{yx}(x, y) & J_{yy}(x, y) \end{pmatrix} \begin{pmatrix} E^{\text{in}}_x(x, y, z_{\text{in}}) \\ E^{\text{in}}_y(x, y, z_{\text{in}}) \end{pmatrix} .$$

The two enforced requirements result in $J_{xx} = J_{yy} = J$, i.e., an independent response upon the incident polarization state, and $J_{xy} = J_{yx} = 0$, i.e., no cross polarization terms. Clearly, these aspects can be verified by experimental methods, i.e., by measuring spatially resolved the Jones-matrix. Although the enforced requirements are never fulfilled in a strict mathematical sense considering Maxwell's Equations, they remain approximately fulfilled within a predominant part of micro-optics. In this regime optical structures have characteristic length scales in the order of multiple wavelengths and polarization influences are often negligible. In this case, the governing equation to model the optical system is then given by

$$\Delta\mathbf{E}(\mathbf{r}, \omega) + k_0^2 n^2(\mathbf{r}, \omega)\mathbf{E}(\mathbf{r}, \omega) = 0 \quad . \tag{1.10}$$

This equation is referred to as semi-vectorial formulation of scalar optics in the following. In this framework, the vectorial character of light is not neglected. The major assumption belongs to the polarization independent behavior of the component. Hence, the change of the polarization of an initial field caused by the optical system is ignored. Within this semi-vectorial scalar optical description, the remaining field components are derived from the two individual polarizations, e.g., $E^{\text{out}}_{x,y}(\mathbf{r}, \omega)$, relying on Eqn. 1.9.
In case, one of the polarization components is dominating, Eqn. 1.10 can be further simplified. In this case it is sufficient to only consider the dominating field component in Eqn. 1.10

$$\Delta\mathrm{E}(\mathbf{r}, \omega) + k_0^2 n^2(\mathbf{r}, \omega)\mathrm{E}(\mathbf{r}, \omega) = 0 \quad . \tag{1.11}$$

This regime is usually considered as scalar optics. Nevertheless, due to the decoupled structure of Eqn. 1.10 the remaining field components are derived straight forward.
Until now, conditions were discussed that justify a scalar optical description of optical systems. Moreover, this viewpoint can also provide interesting implications for the assessment of nano-structured systems. In particular, meta-lenses and related components are of growing importance [2]. They are composed of specially designed subwavelength structures. Similarly to conventional diffractive optical elements (DOEs) these devices allow to manipulate an incoming wavefront on demand. In addition, they can also enable to tailor dispersive or polarization properties [44]. To model these components, it is well known, that rigorous simulations are required to correctly describe the interaction of these structures with the incoming wave [2]. While these devices can enable a polarization multiplexing, however, for various applications such as meta-lenses a polarization independent functionality is desired. In other words, in these cases a scalar behavior is desired. However, this intention contrasts the necessity of solutions to the full set of Maxwell's equations. In particular, the need of rigorous simulations implies, that the components will affect

an initial polarization. As a consequence, at least cross-polarization terms $J_{xy,yx} \neq 0$ will emerge. This excitation of cross-polarization terms should lower the overall diffraction efficiency of these devices. Hence, in contrast to classical DOEs these meta-devices should not reach the theoretical diffraction efficiency of 100% in the individual polarization states.

Finally, to get a coarse feeling for errors introduced by neglecting the depolarization term, a representative example is discussed in the following: The eigenmodes of an artificial fiber with a refractive index of the core $n_{\text{core}} = 1.5$ surrounded by air $n = 1$ considered at a wavelength of $\lambda = 632$ nm are compared between a rigorous approach and a scalar one. The core has an elliptical shape with a major axis of $a = 2$ µm and a minor axis of $b = 1$ µm. These are typical, or even small, size dimensions in micro-optical simulations, i.e., with feature sizes in the range of just a couple of wavelengths. Moreover, a typical index-contrast between glass and air is considered.

The broken symmetry, i.e., the elliptical fiber core, lifts the degenerated character of the mainly x- and y-polarized eigenmodes and induces a certain anisotropy. This effect is of full vectorial nature and not considered within the semi-vectorial extension of a scalar approach. Hence, analyzing connected eigenmodal properties, allows to assess the errors induced by the approximations. The individual eigenmodes, numbered by the index k, can be written in the form $\boldsymbol{E}_k(\mathbf{r},\omega) = \mathbf{e}_k(x,y,\omega)\, e^{i\frac{2\pi}{\lambda} n^k_{\text{eff}}(\omega) z}$, where $\mathbf{e}_k(x,y,\omega)$ is the vectorial eigenmodal field profile and $n^k_{\text{eff}}(\omega)$ the effective mode-index. In Fig. 1.1 the comparison between the rigorous and the scalar solution for the mainly x-polarized eigenmodes is shown. For the scalar case, an eigenmode solver is used, which relies on Eqn. 1.11. In addition, the E_y component is set to zero and

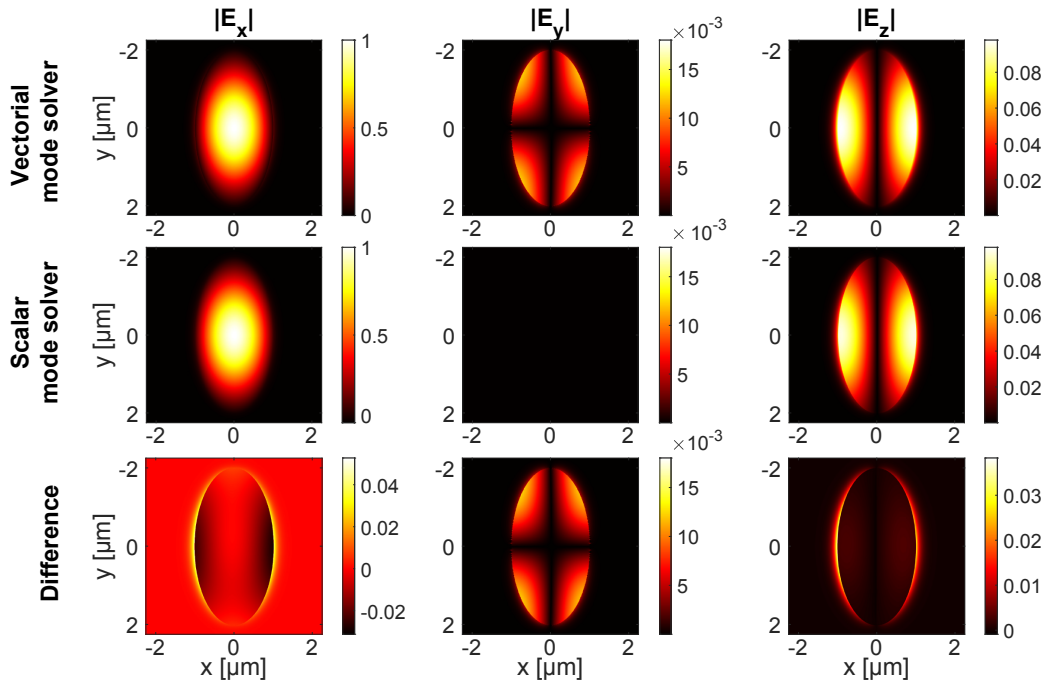

Figure 1.1: Top: Mainly x-polarized vectorial eigenmode of an elliptical fiber with a major- and minor-axis of $a = 4$ µm and $b = 2$ µm. The fiber is characterized by a refractive index of $n = 1.5$ surrounded by air $n = 1$. Middle: A scalar eigenmode solver was used to calculate the eigenmode. The longitudinal E_z component is retrieved by Eqn. 1.12. Bottom: Differences between the individual modal field profiles $|E_i^{\text{Vec}}| - |E_i^{\text{Scal}}|$ are evaluated.

the longitudinal E_z component is retrieved using the divergence theorem $\nabla \cdot \mathbf{E} = 0$ for the homogenous parts of the fiber

$$E_z = i \frac{\partial_x E_x + \partial_y E_y}{\frac{2\pi}{\lambda} n_{\text{eff}}(\omega)} \ . \tag{1.12}$$

By comparing the eigenmodal field profiles of the vectorial and the semi-vectorial extension of the scalar approach an amplitude error can be evaluated. It gets evident that there is an high similarity and relative deviations are in the range of 10^{-2} recognizable for the E_y field component. To also assess phase errors, the effective mode indices of the mainly x- and y-polarized vectorial eigenmode will be compared to the scalar one. The respective indices for vectorial eigenmodes are given as $n_{\text{eff}}^{\text{x-pol}} = 1.4888$, $n_{\text{eff}}^{\text{y-pol}} = 1.4896$ and for the scalar one as $n_{\text{eff}}^{\text{scal}} = 1.4891$. Therefore, respective errors are in the range 10^{-4}. While the errors in the range of one percent in the amplitudes will be acceptable in a majority of scenarios, this situation differs for the phase errors. The absolute error in phase accumulates with the propagation in z-direction and most notably a change in the polarization state of the initial field will occur. A phase error of 2π by relying on the scalar eigenmode is connected to a propagation distance of more than 10mm. This could be problematic within the usual working areas of fiber optics. However, in micro-optics often optical components are considered, which have only a very small longitudinal extension in the low micrometer regime along the z-direction, i.e., diffractive optical elements or diffractive lenses. In these regimes this induced phase error is mostly negligible.

Finally, to assess the limits of a scalar model, additional simulations are performed. To this end, the eigenmodes of varying elliptical waveguides are evaluated. In particular, the index contrast and the ratio between the minor and major axis are kept constant in accordance to the previous example. Then, the minor axis is varied in between $a = .2\mu\text{m}$ and $a = 3\mu\text{m}$ and the eigenmodes are calculated for a wavelength of $\lambda = 632\text{nm}$. The calculates modes are normalized by their overall power and the amplitude error

$$\epsilon_{\text{Amplitude}} = 0.5 \int \left(\left| \left| E_x^{\text{Vec}} \right|^2 - \left| E_x^{\text{Scal}} \right|^2 \right| + \left| \left| E_y^{\text{Vec}} \right|^2 - \left| E_y^{\text{Scal}} \right|^2 \right| + \left| \left| E_z^{\text{Vec}} \right|^2 - \left| E_z^{\text{Scal}} \right|^2 \right| \right) \ , \tag{1.13}$$

is evaluated. A maximum value of one is achieved in case the modes are entirely disjunct. Moreover, the phase error is evaluated by assessing the ratio of the effective mode indices between the vectorial and the scalar solution $\epsilon_{\text{Phase}} = \frac{n_{\text{eff}}^{\text{x,y-pol}}}{n_{\text{eff}}^{\text{scal}}}$. These results are shown in Fig. 1.2. It turns out, that the amplitude errors $\epsilon_{\text{Amplitude}}$ fall below a value of five percent for diameters of approximately 1.5 wavelengths and this error might be acceptable in a majority of scenarios. Nevertheless, the phase errors accumulate with the propagation distance and their overall influence is problem specific. For the considered scenarios in this thesis, where respectively thin micro-optical elements are investigated, this phase error is negligible.
This rather heuristic example was discussed in order to evaluate the validity of the scalar approximation. It seems questionable to neglect the depolarization term at all in a strict mathematical sense. However, regarding the proposed example, it seems to be sufficient also in the wider range of typical micro-optical elements.

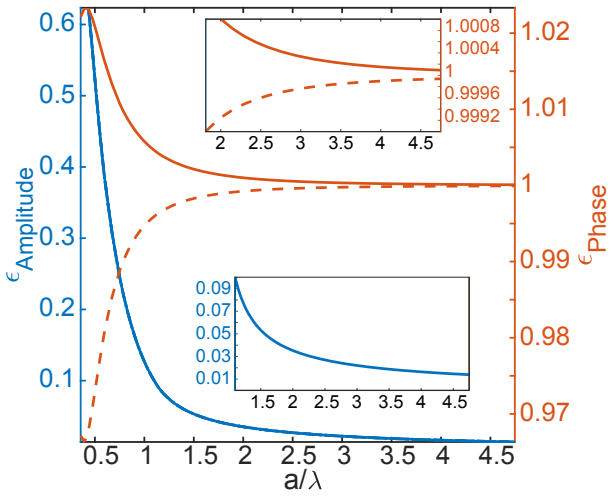

Figure 1.2: Blue: Evaluation of the amplitude error $\epsilon_{\text{Amplitude}}$ for the mainly x-polarized vectorial eigenmode in comparison to the scalar one. Orange: Evaluation of the phase error ϵ_{Phase} for the individual vectorial eigenmodes in comparison to the scalar one. The solid line corresponds to the mainly y-polarized eigenmode and the dotted one to the mainly x-polarized one. Note, the minor axis is scaled in wavelengths.

1.1.3 Unidirectional modeling of inhomogeneous media

In this section the unidirectional approximation of scalar optics will be discussed. Then, any backward propagating field components such as reflected fields are neglected. Therefore, resonant structures, where the interaction of forward and backward propagating field components is essential, cannot be treated within this approximation. To introduce the formal separation of forward and backward propagating field components, Eqn. 1.10 is rewritten as

$$\begin{aligned} \left(\partial_z^2 + \mathcal{H}_T\right) E_{x,y} &= 0 \quad , \\ \mathcal{H}_T &= \partial_x^2 + \partial_y^2 + k_0^2\, n^2(x,y,z) \quad , \end{aligned} \tag{1.14}$$

where $\mathcal{H}_T$ is the transverse Helmholtz operator. One may formally rewrite Eqn. 1.14 as [45–47]

$$\left(i\sqrt{\mathcal{H}_T} + \partial_z\right)\left(i\sqrt{\mathcal{H}_T} - \partial_z\right) E_{x,y} = 0 \; .$$

Here, the square root Helmholtz operator $\sqrt{\mathcal{H}_T}$ is introduced, being formally defined in terms of a power-series. Moreover, it is assumed that the commutator $[\partial_z, \sqrt{\mathcal{H}_T}]$ can be neglected, which physically implies that back reflections within the inhomogeneous medium are ignored. Then, the forward Helmholtz-Equation is identified as [45–48]

$$\partial_z E_{x,y} = i\sqrt{\mathcal{H}_T} E_{x,y} \; , \tag{1.15}$$

which obeys a formal solution according to

$$E_{x,y}(x,y,z_0+z) = e^{iz\sqrt{\mathcal{H}_T}} E_{x,y}(x,y,z_0) \; . \tag{1.16}$$

In the previous chapter, plane waves and eigenmodes were shortly discussed. These rigorous solutions are fundamental eigensolutions of Eqn. 1.15. The amplitudes are given by the eigenfunctions and the propagation constants as corresponding eigenvalues. It is the aim of section 1.3 and 1.4 to find and discuss further approximate solutions of either Eqn. 1.15 or 1.16. This leads to the Beam-Propagation-Methods (BPM) and the Wave-Propagation-Method (WPM) to simulate inhomogeneous structures. Before these algorithms are introduced, the following

section discusses the thin-element approximation. This simulation technique corresponds to the most-widespread algorithm to assess micro-optical elements.

1.2 Thin-element approximation

In this section the thin-element approximation (TEA) will be discussed. Then, micro-optical structures are simulated as a combined ray- and wave-optical approach. On the one hand, in homogeneous subspaces, i.e., before and behind the component, the beam is propagated by wave optical algorithms. On the other hand, the impact of the component itself is approximated by a geometric-optical approach. To discuss this concept in more depth, the connection between a geometric and wave-optical picture needs to be introduced in more detail.
For a vanishing wavelength $\lambda \longrightarrow 0$ geometrical- and wave optics converge to the same limit. On the one hand, the direction vector $\mathbf{n}$ of the rays is proportional to the gradient of the phase $\mathbf{n} \propto \nabla\varphi$ of the wave. On the other hand, the phase value $\varphi(\mathbf{r})$ of this wave is identified as the optical path length OPL of a given ray along its trajectory

$$\varphi(\mathbf{r}) = \frac{2\pi}{\lambda}\mathrm{OPL} = \frac{2\pi}{\lambda}\int_T n(s(\mathbf{r}))ds \quad , \tag{1.17}$$

where T denotes this trajectory of the ray path and $n(s(\mathbf{r}))$ denotes the local refractive index as a function of propagation length s along the curve T. This connection between the phase of a wave and the geometrical rays allows to interchange and switch between them. This aspect lies the foundation of the thin-element approximation (TEA). The effect of a micro-optical element for the outgoing wave $E_{\mathrm{out}}(x, y, z_0)$ is approximated as a transmission function $t(x, y)$ which changes the incoming wave $E_{\mathrm{out}}(x, y, z_0) = t(x, y)E_{\mathrm{in}}(x, y, z_0)$ assuming an optical element of vanishing thickness. If the micro-optical element is non-absorbing only the incoming phase is altered by the micro-optical element and the transmission function takes the form $t(x, y) = e^{i\Delta\varphi(x,y)}$. To derive this phase change $\Delta\varphi(x, y)$, an incoming collimated beam parallel to the z-axis is considered. For a sufficiently thin micro-optical element, one might approximate the trajectory T in Eqn. 1.17 as a straight line. Hence, any ray bending inside the component is neglected. Then, the change in the wavefront induced by a micro-optical element is described as

$$\Delta\varphi(x, y) = \frac{2\pi}{\lambda}\int_{z_0}^{z_1} n(x, y, \tilde{z})d\tilde{z} \quad , \tag{1.18}$$

where z corresponds to the fundamental propagation direction. For the important case of a surface profile $z(x, y)$ realized on a substrate characterized by a refractive n_{sub} in a surrounding medium n_{surr} Eqn. 1.18 reduces to

$$\Delta\varphi(x, y) = \frac{2\pi}{\lambda}(n_{\mathrm{sub}} - n_{\mathrm{surr}})z(x, y) + \mathrm{const.} \quad . \tag{1.19}$$

The constant term in Eqn. 1.19 does not affect the physical simulations and it will be neglected in the following.
Fig. 1.3 visualizes the aspect of the neglected ray bending inside the micro-optical component, which in the following is analyzed in more detail. In reality, refraction causes a redirection of the ray and the real optical path length is different. Clearly, the error induced by the TEA is

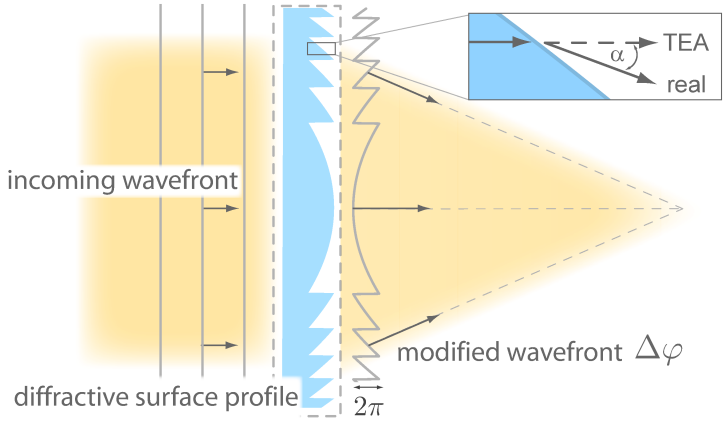

Figure 1.3: Schematic sketch to illustrate the thin-element approximation. The impact of a micro-optical element is described as the induced phase delay an incoming wavefront is altered by the component. This phase delay is approximated as the optical path length difference for a ray parallel to the optical axis.

connected to both the thickness of the element and the deflection angles. To get an estimate for the error of the TEA one could consider the maximum length difference appearing at largest deflection angle $\alpha_{\max}$, e.g., defined by the numerical aperture NA, and the full thickness of the element d. The two rays then have a difference in length of

$$\Delta d = d_{\text{real}} - d_{\text{TEA}} = \frac{d}{\cos(\alpha_{\max})} - d = d\left(\frac{1}{\sqrt{1-NA^2}} - 1\right) \quad .$$

Consequently, the maximum error in the optical phase is given as

$$\Delta\varphi_{\max} = \frac{2\pi}{\lambda} \quad \max[n_{\text{sub}}, n_{\text{surr}}] \quad d\left(\frac{1}{\sqrt{1-NA^2}} - 1\right) \quad .$$

In the following, a hypothetical diffractive optical element (DOE) is assessed, which features a numerical aperture of NA= 0.3. Referring to conventional diffractive optical elements, this belongs to a rather large numerical aperture, where angles of up to $\alpha \approx 17°$ are involved. Moreover, the DOE is assumed to be characterized by refractive indices of $n_{\text{sub}} = 1.5$, $n_{\text{surr}} = 1.0$ and working in first diffraction order. Then, the structures induce a maximum phase delay of one wavelength and the maximum height is characterized as $d = \frac{\lambda}{\Delta n}$. For this scenario the maximum wavefront error due to the application of the TEA is approximately $\frac{\lambda}{7}$. In addition, the TEA assumes incoming collimated light parallel to the optical axis, which causes additional inaccuracies. These errors can be resolved, in principle, by relying on a proper geometric optical consideration. In particular, the local plane interface approximation resolves the errors due to neglected ray bending [49, 50]. Moreover, in this framework also amplitude changes can be considered by properly evaluating the ray redistribution [51, 52]. Nevertheless, these extensions still rely on geometric optical principles and intrinsically neglect any influence of diffraction, which occur inside the component. Overcoming these limitations require improved numerical models. It will be shown in Sec. 2.4.1 that steep edges in the surface profile induce diffraction effects, which can reduce the overall performance of the component - An effect that is completely neglected in the TEA.

Nevertheless, despite the shortcomings of the TEA it is indispensable for the design of diffractive optical elements. It establishes a direct analytic connection between the optical properties of a wave, e.g., its phase, and the topology of a sample. This allows to design functional micro-optical structures efficiently. In particular, phase-retrieval algorithms [53] can

be used. Then the phase change $\Delta\varphi$ is calculated by which an incident wavefront must be changed, so that an incoming intensity distribution is converted into an almost arbitrary target distribution. The actual surface profile of the component is calculated by the TEA from the retrieved phase $\Delta\varphi$. However, in reality the performance of a device might by lower than predicted by the application of the TEA. To cope these challenges, models beyond the TEA are required to assess the as-built performance realistically. Then, the phase-retrieval algorithms should be tuned to keep the final design within the limits of the TEA. These aspects are discussed detailed within a practical example in chapter 5, where an integrated illumination concept is introduced, which can overcome the limitations of classical diffractive beam shaping.The algorithms, which enable an improved modeling of micro-optical elements are discussed in the following Sec. 1.3 and 1.4.

1.3 Beam propagation methods

In this section the beam propagation methods (BPMs) will be shortly reviewed. These algorithms are well established for the simulation and analysis of integrated photonic devices such as waveguides. Over the years, a huge variety of different formulations emerged, which allows to efficiently model different scenarios. Here, the formulations that were introduced by Hadley [48,54] are considered, which are known as Padé-BPMs. These are the most wide-spread ones for modeling paraxial and non-paraxial phenomena[3]. As these methods are state-of-the-art, only the essential aspects will be reviewed in the following. For further details the book of Kawano *et al.* [57] and the technical background section of the commercial OptiBPM software manual [58] is referred, which provide a great overview.

The individual beam propagation methods were formally developed for guided wave phenomena. For their derivation, a slowly varying envelope approximation is typically considered to separate high-frequency oscillations in the amplitude and phase evolution from the slowly varying ones. To this end, a wave of the form $E(\mathbf{r},\omega) = \mathcal{E}(\mathbf{r},\omega)e^{ik_0 n_{\mathrm{ref}} z}$ is considered, where an effective reference index n_{ref} describes the highly oscillatory part $e^{ik_0 n_{\mathrm{ref}} z}$. Substitution into Eqn. 1.15 gives

$$\partial_z \mathcal{E}(\mathbf{r},\omega) = i\left(\sqrt{\mathcal{P} + k_0^2 n_{\mathrm{ref}}^2} - k_0 n_{\mathrm{ref}}\right)\mathcal{E}(\mathbf{r},\omega) \quad , \tag{1.20}$$

where $\mathcal{P} = k_0^2\left(n(x,y,z)^2 - n_{\mathrm{ref}}^2\right) + \Delta_\perp$. Within Eqn. 1.20 a square root operator $\sqrt{\mathcal{P} + k_0^2 n_{\mathrm{ref}}^2}$ emerges, being formally defined in terms of a power-series. It was the achievement of Hadley in [48,54] to show that a Padé-series yields the best accuracy with the fewest terms of expansion for this purpose. It was suggested to rewrite Eqn. 1.20 into a Padé-series of order (K,L) with expansion coefficients $a_k,\ b_k$ as

$$\left(\sqrt{\mathcal{P} + k_0^2 n_{\mathrm{ref}}^2} - k_0 n_{\mathrm{ref}}\right) = i\frac{\mathcal{N}}{\mathcal{D}} = i\frac{\sum_{k=0}^{K} a_k \mathcal{P}^k}{\sum_{k=0}^{L} b_k \mathcal{P}^k} \quad . \tag{1.21}$$

[3] Another important formulation was introduced by Feit and Fleck [55], known as the Fast-Fourier transform BPM. However, this formulation was mentioned by Chung and Dagli in [56] to be inferior compared to the lowest-order formulation of the Padé BPM. Therefore, the fast Fourier transform BPM is not considered in the following.

Thus, every additional expansion order provides a more accurate approximation of the field evolution operator. The Padé-approximates describe the transition from paraxial- to wide-angle BPM formulations and they are summarized as follows [48], where $k_{\mathrm{ref}} = k_0 n_{\mathrm{ref}}$:

Order (K,L)	(1,0)	(1,1)	(2,2)	(3,3)
Expression	$\frac{\mathcal{P}}{2k_{\mathrm{ref}}}$	$\frac{\frac{\mathcal{P}}{2k_{\mathrm{ref}}}}{1+\frac{\mathcal{P}}{4k_{\mathrm{ref}}^2}}$	$\frac{\frac{\mathcal{P}}{2k_{\mathrm{ref}}}+\frac{\mathcal{P}^2}{4k_{\mathrm{ref}}^3}}{1+\frac{3\mathcal{P}}{4k_{\mathrm{ref}}^2}+\frac{\mathcal{P}^2}{16k_{\mathrm{ref}}^4}}$	$\frac{\frac{\mathcal{P}}{2k_{\mathrm{ref}}}+\frac{\mathcal{P}^2}{2k_{\mathrm{ref}}^3}+\frac{3\mathcal{P}^3}{32k_{\mathrm{ref}}^5}}{1+\frac{5\mathcal{P}}{4k_{\mathrm{ref}}^2}+\frac{3\mathcal{P}^2}{8k_{\mathrm{ref}}^4}+\frac{\mathcal{P}^3}{64k_{\mathrm{ref}}^6}}$

In order to derive a field propagation algorithm, the longitudinal derivative ∂_z is approximated in Eqn. 1.20 as

$$\partial_z \mathcal{E}(x,y,z,\omega) = \frac{\mathcal{E}(x,y,z+\Delta z,\omega) - \mathcal{E}(x,y,z,\omega)}{\Delta z} \quad .$$

This corresponds to a second-order approximation of the derivative at the position $z + \frac{\Delta z}{2}$. Therefore the electric field vector $\mathcal{E}(\mathbf{r},\omega)$ on the right-hand side of Eqn. 1.20 is evaluated at this intermediate position

$$\mathcal{E}\left(x,y,z+\frac{\Delta z}{2},\omega\right) \approx \frac{1}{2}(\mathcal{E}(x,y,z+\Delta z,\omega) + \mathcal{E}(x,y,z,\omega)) \quad .$$

Then, Eqn. 1.20 and 1.21 can be rewritten in the form

$$\frac{\mathcal{E}(x,y,z+\Delta z,\omega) - \mathcal{E}(x,y,z,\omega)}{\Delta z} = i\frac{N}{2D}(\mathcal{E}(x,y,z+\Delta z,\omega) + \mathcal{E}(x,y,z,\omega)) \quad ,$$

or equivalently

$$(2D - i\Delta z N)\,\mathcal{E}(x,y,z+\Delta z,\omega) = (2D + i\Delta z N)\,\mathcal{E}(x,y,z,\omega) \quad . \tag{1.22}$$

To propagate an initial beam the operator matrix $(2D - i\Delta z N)$ needs to be inverted. This typically requires the solution of large sparse matrix equations. This can slow down the computations. Alternatively, direct marching schemes like the forward-euler scheme would be desirable. However, these schemes can result in numerical instabilities and the implicit ones are usually preferred [58].

Padé(1,1) in two dimensions

In the following, the numerical BPM algorithm for the first-order Padé(1,1) approximate in two dimensions, i.e., one longitudinal z and one transverse x-dimension, will be outlined. Then Eqn. 1.22 is given as

$$\underbrace{\left(1+\frac{1-ik_{\mathrm{ref}}\Delta z}{4k_{\mathrm{ref}}^2}\mathcal{P}\right)}_{\hat{L}}\mathcal{E}(x,z+\Delta z,\omega) = \underbrace{\left(1+\frac{1+ik_{\mathrm{ref}}\Delta z}{4k_{\mathrm{ref}}^2}\mathcal{P}\right)}_{\hat{R}}\mathcal{E}(x,z,\omega) \quad ,$$

$$\mathcal{P} = \partial_x^2 + k_0^2\left(n(x,z)^2 + n_0^2\right) \quad .$$

These relations can be solved numerically by approximating the second order derivative by

$$\partial_x^2 \mathcal{E}(x,z,\omega) = \frac{\mathcal{E}(x-\Delta x,z,\omega) - 2\mathcal{E}(x,z,\omega) + \mathcal{E}(x+\Delta x,z,\omega)}{(\Delta x)^2} \ .$$

The operators $\hat{L}$ and $\hat{R}$ are then represented in real space by sparse matrices. In two dimensions, these matrices are tridiagonal with the diagonal terms

$$L_{i,i} = 1 + \frac{1+\alpha i k_{\mathrm{ref}}\Delta z}{4k_{\mathrm{ref}}^2}\left(-\frac{1}{(\Delta x)^2} + k_0^2\left(n(x,z)^2 + n_0^2\right)\right) \quad ,$$

and the constant off diagonal terms

$$L_{i,i+1} = L_{i,i-1} = \frac{1+\alpha i k_{\mathrm{ref}}\Delta z}{4k_{\mathrm{ref}}^2}\left(\frac{1}{2(\Delta x)^2}\right) = \text{const.} \quad .$$

For the operator $\hat{L}$ the substitution α stands for $\alpha = +1$. The above relations also hold for the operator $\hat{R}$ for $\alpha = -1$. An initial field $\mathcal{E}(x, z_0, \omega)$ known in the plane $z = z_0$ can be iteratively propagated along the $+z$-direction through the medium by inverting the tridiagonal matrix $\hat{L}$ which gives rise to the recurrence formula

$$\mathcal{E}(x, z+\Delta z, \omega) = \hat{L}^{-1}\hat{R}\,\mathcal{E}(x,z,\omega) \quad . \tag{1.23}$$

Due to the tridiagonal structure of the arising matrices, the inversions are efficiently calculated by the Thomas-algorithm [59]. In particular, this algorithm is a simplified form of Gaussian elimination taking advantage of the tridiagonal structure. Then, the matrix inversions have a complexity $\mathcal{O}(n)$, where (n, n) is the size of the matrix.

Boundary conditions

One important additional aspect is the consideration of proper boundary conditions, i.e., the treatment of the off-diagonals $L_{0,-1}$, $L_{N,N+1}$. If the field is set to zero, $E = 0$, outside the computational grid, the boundary acts as an ideal reflector. This leads to unphysical behaviors as soon as the propagated field reaches this boundary. Instead, one would like to allow the radiation to escape the computational domain without any reflections. To this end, several boundary conditions have been developed in the past. The three most common ones are absorbing boundary conditions (ABC) [60], transparent boundary conditions (TBC) [61, 62] and perfectly matched layers (PMLs) [63]

The ABC artificially reduces the field components close to the boundary by multiplying the field after each computational step with a transmission function $t(x)$, which damps the field magnitude close to the boundary. The function $t(x)$ is often chosen as

$$t(x) = \begin{cases} Ae^{-\frac{|x|-x_b}{x_{\max}}} - A + 1, & x_b < |x| < x_{\max} \\ 1, & |x| < |x_b| \end{cases} \ , \tag{1.24}$$

where $A < 1$.

For TBCs it is assumed that the field values in close proximity to the boundary is described accurately enough by a plane wave. Then the boundary value is estimated from the knowledge of

the field close to the boundary. PMLs can be viewed as an artificial anisotropic medium, which is especially designed to avoid reflections occurring at the interface between this medium and the actual computational domain. Hence an incoming wave enters this medium without back-reflection. Additionally, this medium is absorbing and damps the wave. Hence, this boundary condition is ideal to imitate an unbounded and open computational domain. Nevertheless, the numerical effort is the highest for this approach. Within this thesis the ABC boundary conditions are considered. They provide good performance at low computational cost.

Higher Padé orders

For higher Padé orders higher powers of the operator $\mathcal{P}$ arise. This requires the numerical approximation of higher order derivatives, which leads to an increased bandwidth of the resulting band matrices $\hat{L}$ and $\hat{R}$. Then, the very efficient Thomas-algorithm can no longer be applied for the required matrix inversions. To resolve this issue, Hadley proposed the multi step method for wide-angle beam propagation [54]. The main idea belongs to the decomposition of a Padé(n,n)-approximate into a factorized version of Padé(1,1) approximates by formally rewriting terms of the form

$$\mathcal{E}(x,y,z+\Delta z,\omega) = \frac{\sum_{k=0}^{N} a_k \mathcal{P}^k}{\sum_{k=0}^{N} b_k \mathcal{P}^k}\mathcal{E}(x,y,z,\omega) = \frac{\prod_{k=0}^{N}\left(1+c_k\mathcal{P}\right)}{\prod_{k=1}^{N}\left(1+c_k^*\mathcal{P}\right)}\mathcal{E}(x,y,z,\omega) \quad . \tag{1.25}$$

This requires the solution of a N-th order algebraic equation to determine the coefficients c_k. Finally, every Padé(1,1) operator term acts individually on the field, which suggests to propagate an initial field in a sequence of N steps to the next plane

$$\mathcal{E}_{\frac{k+1}{N}}\left(x,y,z+\Delta z,\omega\right) = \frac{\left(1+c_k\mathcal{P}\right)}{\left(1+c_k^*\mathcal{P}\right)}\mathcal{E}_{\frac{k}{N}}\left(x,y,z+\Delta z,\omega\right) \quad . \tag{1.26}$$

This procedure reduces the propagation of an initial field in a higher-order Padé approximation to a sequence of N Padé(1,1)-propagation steps. In two dimensions, for each of the N steps, the efficient Thomas-algorithm can be used to perform the necessary matrix inversions, which can speed up the simulations considerably.

Three-dimensional simulations

For three-dimensional simulations the operator $\mathcal{P} = k_0^2\left(n(x,y,z)^2 - n_{\text{ref}}^2\right) + \partial_x^2 + \partial_y^2$ gives rise to an increased bandwidth of the matrices, which in fact become only block-diagonal. Thus, the application of the efficient Thomas-algorithm is not possible. In order to decrease the numerical complexity of the inversions, the individual Padé operator terms may be approximated by [64]

$$\begin{aligned}
1+c_k\mathcal{P} &= 1+c_k\Big(k_0^2\left(n(x,y,z)^2-n_{\text{ref}}^2\right)+\partial_x^2+\partial_y^2\Big) \\
&\approx \left(1+c_k\mathcal{T}_x\right)\left(1+c_k\mathcal{T}_y\right) \quad , \\
\mathcal{T}_x &= \left(\frac{k_0^2}{2}\left(n(x,y,z)^2-n_{\text{ref}}^2\right)+\partial_x^2\right) \quad , \\
\mathcal{T}_y &= \left(\frac{k_0^2}{2}\left(n(x,y,z)^2-n_{\text{ref}}^2\right)+\partial_y^2\right) \quad .
\end{aligned}$$

This procedure is known as the alternating direction implicit method (ADI) and it decouples the individual transverse dimensions, i.e, x and y. As a consequence, the individual matrices

$1 + c_k \mathcal{T}_{x,y}$ become tridiagonal in shape and an iterative solution procedure similar to the multi step method in 2D is suggested. Then, the propagation of the initial field is realized by relying on the Thomas algorithm. Despite this advantage, there, nevertheless, appears a splitting error of the form $c_k \mathcal{T}_x \mathcal{T}_y$. This error can reduce the accuracy of the Padé approximate. Only for the paraxial Padé(1,0)-BPM this error reduces with $\mathcal{O}(\Delta z^2)$ and by a sufficient small step size Δz it becomes negligible. For the higher order Padé-formulations this splitting error is of zeroth order [65] and the ADI-splitting cannot be applied. Thus, Padé-based BPMs in three dimensions have a substantially increased computational complexity and overcoming these limitations remains an area of current research. Several efforts have been devoted to overcome appearing splitting errors, while relying on iterative or approximate techniques [33, 65–69]. To invert the resulting sparse matrices, it is well established to rely on iterative indirect solvers like BiCGStab [70]. While these iterative matrix-solvers provide an increased computational performance in comparison to direct solvers, a finite residual error remains due to the iterative process. Nevertheless, these residual errors can be controlled and therefore nearly arbitrary small errors can be achieved.

It can be summarized at this stage, that the BPMs have a substantially decreased computational performance to model non-paraxial phenomena in three dimensions. In these cases the BPMs cannot be formulated as iterative solutions of tridiagonal matrices for which efficient solution techniques, i.e., the Thomas-algorithm, exist. Instead, algorithms need to be used which have an increased computational complexity and thus increase the computational runtime. To this end, it is desirable to estimate a lowest order BPM formulation for a given optical system in advance. In Sec. 2.3.1 this issue will be addressed, which rather easily allows to choose a valid BPM-formulation. Moreover, in this section also sampling requirements of the BPMs are addressed, which was omitted here. However, alternative algorithms are desirable which certainly can overcome the shortcomings of the BPMs.

1.4 Wave propagation method

An alternative approach to propagate light through an inhomogeneous media was proposed by Brenner *et al.* [71] named the wave propagation method (WPM). It was introduced in order to overcome the paraxial restrictions of the standard formulations of the BPMs, i.e., the fast Fourier transform-BPM and the Padé(1,0)-BPM. The algorithm is a direct extension of the angular spectrum of plane-wave decomposition as given in Eqn. 1.8 and suggests to propagate an initial field through the optical system by locally varying the propagation constant in a given plane z_0 according to the refractive index distribution $k_z(x, y, k_x, k_y) = \sqrt{k_0^2 n(x, y, z_0)^2 - k_x^2 - k_y^2}$. Then the field distribution in a subsequent plane is described as

$$\begin{aligned} E(x, y, z_0 + \Delta z) &= \int \tilde{E}(k_x, k_y, z_0) e^{ik_z \Delta z} e^{i(k_x x + k_y y)} dk_x dk_y \quad , \\ \tilde{E}(k_x, k_y, z_0) &= \mathcal{F}^{-1}\left\{E(x, y, z_0, \omega)\right\} \quad , \\ k_z(x, y, k_x, k_y) &= \sqrt{k_0^2 n(x, y, z_0)^2 - k_x^2 - k_y^2} \quad . \end{aligned} \tag{1.27}$$

The WPM algorithm might be viewed as direct extension of geometrical optics. For an inhomogeneous medium every plane wave characterized by the wave-vector $\mathbf{k} = (k_x, k_y, k_z)^T$ locally

obeys the dispersion relation $|\mathbf{k}|^2 = k_0^2\, n^2(x, y, z_0)$. Hence, individual plane waves are propagated locally into the directions $\mathbf{k}$ as dictated by the analytic dispersion relation. This suggests an accurate propagation of the phase of an initial beam throughout the inhomogeneous medium. Moreover, across interfaces the transverse wave-vector $(k_x, k_y)^T$ remains preserved and the longitudinal component k_z gets adapted. This ensures, the correct application of the law of refraction. Within this perspective the WPM seems to be ideally suited for the simulation of challenging micro-optical scenarios. These abilities were verified by discussing representative application scenarios, e.g., by Brenner and Singer in [71, 72]. There, the characteristics of gradient index lenses were investigated and compared to analytic results. These findings indicate correct phase propagation for angles of up to 85° degrees. These abilities of the algorithm motivated further development and resulted into a vectorial extension of the scalar formulation [73]. For instance, this algorithm is able to predict cross-polarization influences in high numerical aperture systems.

Based upon these insights the WPM seems to be an ideal candidate to overcome the restrictions of the TEA. Hence, this algorithm will be assessed in detail against the different formulations of the BPMs in the following chapter and a more detailed discussion about sampling requirements and boundary conditions is omitted here. There, also a derivation of the algorithm from a rigorous background is provided. This was previously missing and an analytic estimation of errors was not available in a strict sense. Moreover, based on a reformulation, the algorithm can be accelerated for piecewise homogeneous media.

2 Improved Modeling Beyond the Thin-Element Approximation

In this chapter the methodology for the improved modeling of micro-optical elements is developed. In particular, the wave propagation method is reformulated for piecewise homogeneous structures, which enables a serious advantage in runtime since it allows to use fast Fourier transforms. This derivation is shown in Sec. 2.2. Moreover, this reformulated algorithm is assessed in comparison to the individual formulations of the Padé beam propagation methods for a challenging scenario including both high-index contrasts and non-paraxial conditions. Thus, the chosen example will be representative to assess the applicability to overcome the limitations of the TEA. These results are discussed in Sec. 2.3. Moreover, in Sec. 2.3.1 certain pitfalls and difficulties connected to BPM simulations will be discussed and a methodology is proposed to estimate the required Padé-order and sampling density based on first order principles. Finally, in Sec. 2.4 the algorithm of the WPM is specialized into a rotationally symmetric formulation. This can increase the computational performance further and in Sec. 2.4.1 the algorithm is used to analyze false light of diffractive lenses. It turns out, that the rings of segmentation of the diffractive lens profile induce diffractive effects, which are not predicted within the TEA formalism. These aspects are discussed in detail, as they are also of particular importance within the design of general diffractive optical elements.

A part of these results was developed together with Simon Thiele from the *Institut für technische Optik* in Stuttgart. To be precise, he provided the rotationally symmetric Comsol model, which was used to evaluate false light of diffractive lenses in Sec. 2.4.1. Moreover, results presented in Sec. 2.3.1 were developed together with Asis Saad Rodriguez in the framework of a guided research, which resulted in his Research labwork thesis [74].
Several parts of the results in the upcoming chapter have been published in Optics Express in [75] and in Optics Letters in [76].

2.1 Error assessment of the wave propagation method

In this section, errors of the WPM-algorithm will be assessed. To this end, a theoretical derivation of the algorithm is evaluated first. Afterwards, these issues are discussed in a representative example.
The intrinsic coupling of Fourier- and spatial variables in the WPM-algorithm (see Eqn. 1.27) is unusual and makes a derivation of the algorithm intricate. The theory of pseudo-differential operators [77, 78] is required and provides the theoretical foundation of the algorithm [79]. Details about the derivation are provided within Appendix A. It turns out, that the algorithm corresponds to the zeroth expansion order of a pseudo-differential operator series [77–79].

In the following the results are shortly discussed for the two dimensional case, i.e., one transverse and one longitudinal dimension, to achieve a compact notation. The leading error contribution $\Delta k_z^0(x, k_x)$ according to Eqn. A7 in Appendix A is connected to the propagation

constant $k_z(x, k_x)$ within Eqn. 1.27. For a single propagation step in the inhomogeneous medium $n_{z_0}(x) = n\,(x, z_0)$ it reads as

$$\Delta k_z^0(x, k_x) \sim i\,\frac{{k_0}^2\, n_{z_0}(x)\;k_x\,\partial_x n_{z_0}(x)}{k_z(k_x, x)^3}\quad . \tag{2.1}$$

This error becomes large for strong index changes perpendicular to the optical axis, i.e., $\partial_x n_z(x) \neq 0$, and for non-paraxial conditions, i.e., $k_z \longrightarrow 0$. For propagating field components, where the imaginary part of the wave vector is zero $\Im\{k_z\} = 0$, the error term is purely imaginary and thus only affects the amplitude of the field upon propagation. As a consequence, the phase propagation is correct in leading order. Thus, the WPM can indeed be identified as an ideal candidate to overcome the limitations of the TEA, where essentially the induced phase change $\Delta\varphi$ of a micro-optical component is of interest.

In order to assess the error in more detail, a representative example is discussed in the following. The field evolution of an initial Gaussian beam with a waist of $\sigma = 2\mu$m at a wavelength $\lambda = 1\mu$m in a slab waveguide with a width of $w = 40\mu$m and a refractive index of the $n_{\text{core}} = 1.5$ surrounded by air $n_{\text{sub}} = 1.0$ is considered. Thus, the example is characterized by an high-index contrast of typical glass to air interfaces. The field distribution is shown in Fig. 2.1 (a) in comparison to the same scenario simulated by the Padé(4,4)-BPM in Fig. 2.1 (d). It gets evident that both the WPM and the BPM are in good agreement for propagation distances $z \leq 2500\mu$m. The algorithms predict the self-imaging point, similar to the Talbot effect, at the

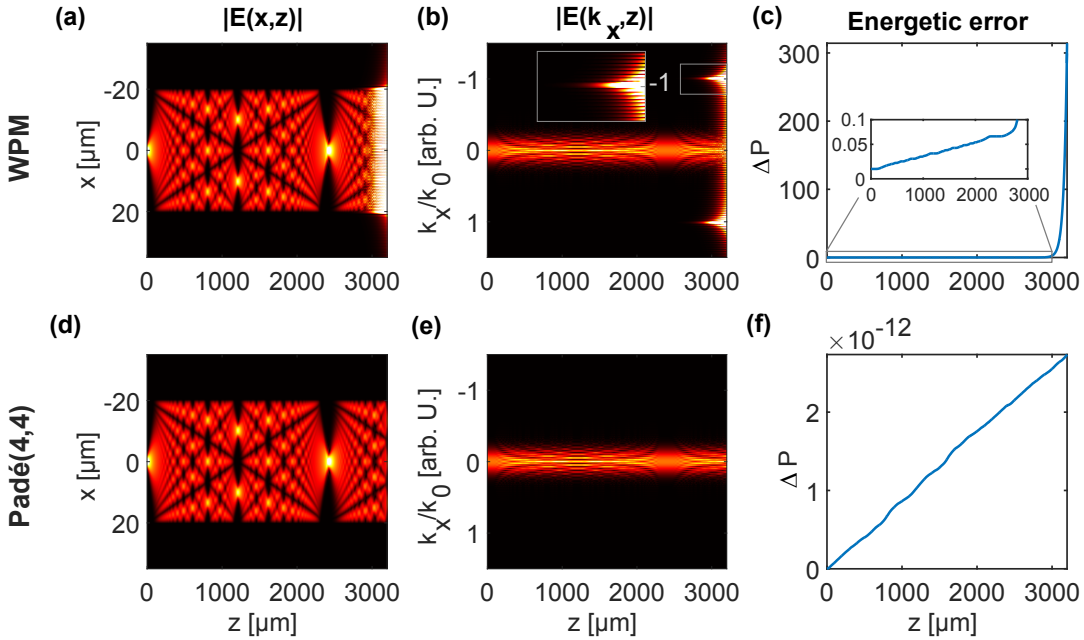

Figure 2.1: Field distribution in a slab wave guide with a width of $w = 40\mu$m characterized by a refractive indices of $n_{\text{core}} = 1.5$ and $n_{\text{sub}} = 1.0$ for an initial gaussian beam with a waist of $\sigma = 2\mu$m at a wavelength $\lambda = 1\mu$m. Respectively, in the top and bottom row the simulation results of the WPM and the Padé(4,4) BPM are compared. (a),(d): The direct field distributions are shown. (b),(e): The transverse Fourier spectra of the field distribution are shown. (c),(f): The energetic error according to Eqn. 2.2 is displayed (Note the different scales between the WPM and BPM simulations).

same position. Nevertheless, at distances of approximately $z = 3000\mu$m the WPM gets unstable and a tremendous field enhancement takes place. In order to evaluate this aspect in more detail Fig. 2.1 (b) and (d) shows the Fourier-spectra $|E(k_x, z)|$ and Fig. 2.1 (e) and (f) the relative power error

$$\Delta P(z) = \frac{\int |E(x,z)|^2 dx - \int |E(x,0)|^2 dx}{\int |E(x,0)|^2 dx} \ . \tag{2.2}$$

The instability is along with the spurious rise of spatial frequencies close to the cutoff frequency $k_z \longrightarrow 0$, i.e., $k_x \longrightarrow k_0$, where Eqn. 2.1 gets singular (see inset in Fig. 2.1 (b)). To regularize the WPM, an artificial damping $\kappa(k_x, k_y)$ with $\Im\{\kappa(k_x, k_y)\} > 0$ can be introduced to damp wave components with high spatial frequencies, k_x and k_y, above a certain threshold value close to the spatial cutoff-frequency. Therefore, the propagation factor is replaced by $k_z(k_x, k_y) \longrightarrow k_z(k_x, k_y) + \kappa(k_x, k_y)$. Introducing this kind of artificial absorption function $\kappa(k_x, k_y)$ can stabilize the algorithm, but, nevertheless, is motivated on a rather heuristic base. Therefore, the application of this procedure is not recommended in general. Instead, higher Padé-order BPMs should be used in cases where the WPM tends to get unstable. Therefore, within all of the examples discussed in the following chapters 2-5 the damping term $\kappa(k_x, k_y)$ is set to zero and skipped in the following.

While this currently gives the impression the BPMs are superior in comparison to the WPM, this is not the case in general. The major strength of the WPM algorithm gets evident for the simulation of micro-optical elements that are otherwise described by the thin-element approximation. For these scenarios the amplitude errors are negligible and the accurate phase propagation characteristics enables accuracies close to rigorous calculations. Moreover, based on a reformulation of the algorithm the computational performance is increased substantially for piecewise homogeneous structures. This aspect is discussed in the following.

2.2 Accelerated algorithm of the wave propagation method

The wave propagation method (WPM) was introduced in Sec. 1.4 and corresponds to an adapted formulation of the angular spectrum of plane wave decomposition (ASPW) for the modeling of inhomogeneous media. While the ASPW can formally be written in terms of Fourier transformations, which allows to implement the procedure by relying on FFTs, this is not possible for the WPM algorithm. In particular, the dependence of the propagation constant $k_z(x, y, k_x, k_y)$ on the spatial variables $(x, y)^T$ prohibits the application of FFTs. Instead, time consuming direct integrations need to be used. Nevertheless, while explicitly excluding gradient-index media and restricting to step index structures, the algorithm can be reaccelerated relying on FFTs. This reformulation will be shown in this section.

Often, actually mostly, micro-optical systems can be decomposed into a finite number M of pairwise disjoint and homogeneous subregions with index n_m. Then, the index distribution $n_{z_0}(x, y) = n(x, y, z_0)$ in a given layer at distance z_0 can be rewritten in the form $n_{z_0}(x, y) = \sum_{m=1}^{M} n_m \Theta_m^{z_0}(x, y)$, where

$$\Theta_m^{z_0}(x,y) = \begin{cases} 1 & n_{z_0}(x,y) = n_m \ , \\ 0 & n_{z_0}(x,y) \neq n_m \ , \end{cases} \tag{2.3}$$

is the characteristic function of the subregion m. This enables to rewrite Eqn. 1.27 as a weighted sum over M propagation steps inside a homogeneous medium with index n_m. Then the WPM can be interpreted in terms of fast Fourier transforms:

$$\begin{aligned} E(x,y,z_0+\Delta z) &= \sum_m \Theta_m^{z_0}(x,y)\mathcal{F}^{-1}\left\{e^{ik_z^m(k_x,k_y)\Delta z}\mathcal{F}\left\{E(x,y,z_0)\right\}\right\} \quad , \\ k_z^m(k_x,k_y) &= \sqrt{{k_0}^2 n_m^2 - {k_x}^2 - {k_y}^2} \quad . \end{aligned} \tag{2.4}$$

This approach can strongly increase the computational performance of the algorithm. Instead of $\mathcal{O}(N^{2D})$ operations in the case of a direct integration of Eqn. 1.27, the modified WPM requires only $\mathcal{O}(M\,N^D\,log(N))$ operations, where M is the discrete number of refractive indices, N the number of grid points and D the number of transverse dimensions.

From a numerical point of view the efficient implementation of the WPM is connected to two individual steps. On the one hand, the ASPW needs to be implemented, which is straight forward. On the other hand, the characteristic function according to Eqn. 2.3 needs to be evaluated. This requires in every propagation step to search within the numerical array of the current refractive index distribution $n_{z_0}(x_i, y_j) = n_{i,j}$ for the individual refractive indices n_m. There are two ways to treat the task and only one is computationally efficient. On the one hand, a logical matrix $\hat{m}$ for every individual refractive index n_m is set up, for which $n_{i,j} = n_m$ leads to a logical 1. Then, the logical matrix is used within the additional steps. On the other hand, a list of matrix-indices (i, j) is build up, which satisfy the condition $n_{i,j} = n_M$. This is the same as converting the logical matrix $\hat{m}$ into its respective indices (i, j). While the prior is referred to as logical indexing in Matlab, the latter is called "find-generated numerical indexing". If logical indexing is applicable, as in the considered case, it should be preferred in any case [80].
The applicability of fast Fourier transforms in the algorithm restricts the choice of boundary conditions for the simulations. In particular, only the absorbing boundary conditions can be applied straight forward and are considered within all the following simulations. As a downside, these boundary conditions require an adaption of the absorption strength A and the width in Eqn. 1.24 specific to the investigated scenario. Beside these additional efforts these boundary conditions are stable and perform well. In the following this reformulated algorithm will be used to assess the performance in terms of accuracy and computational runtime in comparison to the different Padé-BPMs.

2.3 Assessment of the algorithms

Within the previous sections 1.3, 1.4, and 2.2 the algorithms of the BPMs, the original and the reformulated WPM were introduced. All the methods similarly intend to solve the scalar Helmholtz-equation in a unidirectional way. In the following, these algorithms are assessed regarding their ability to overcome the limitations of the TEA. From a pure theoretical point of view it is hard to judge on their performance and especially to compare one against the other. Therefore, in the following a representative example is discussed, which puts these algorithms through their paces. They are evaluated concerning accuracy, sampling requirements and computational runtime. Memory requirements will not be considered. In particular, within the

simulations only the field $E(x, y, z_n)$ in a previous slice z_n needs to be known to calculate the new one at position z_{n+1}. As a consequence, memory requirements are not an issue and only of minor importance. The individual algorithms are investigated for two dimensional simulations, i.e., one transverse x- and one longitudinal z-dimension. In these cases the BPMs do not suffer from additional inaccuracies caused by the iterative matrix-equation solvers (BiCGStab) used within the three dimensional Padé BPMs (see also Sec. 1.3).

In particular, the focusing characteristics of micro-optical lenses of high numerical aperture and high index contrasts are investigated. To this end, the focal field distributions of cylindrical lenses with varying diameters are evaluated. This scenario is challenging, as non-paraxial conditions are involved simultaneously with high index contrasts. The results of the individual algorithms are referred to rigorous simulations of the entire structure. Therefore, the Helmholtz-Equation in two dimensions is solved rigorously for an inhomogeneous refractive index distribution $n(x, z)$. This corresponds to a solution of Maxwells-Equations for the electric field in TE-polarization, i.e., the polarization vector is parallel to the translation invariant dimension [33]. In particular, a COMSOL model is used for these simulations. COMSOL is a commercial finite element analysis software specialized to solve various predefined physical equations or arbitrary user-defined systems of partial differential equations. Here, these solutions are used as a reference for the comparison with the BPMs and the WPM. In Figs. 2.2 (a)–(c) the focal field distributions of a Gaussian beam with a wavelength of $\lambda = 632\,\text{nm}$ and a waist of $\omega_0 = 15\,\mu\text{m}$ focused through

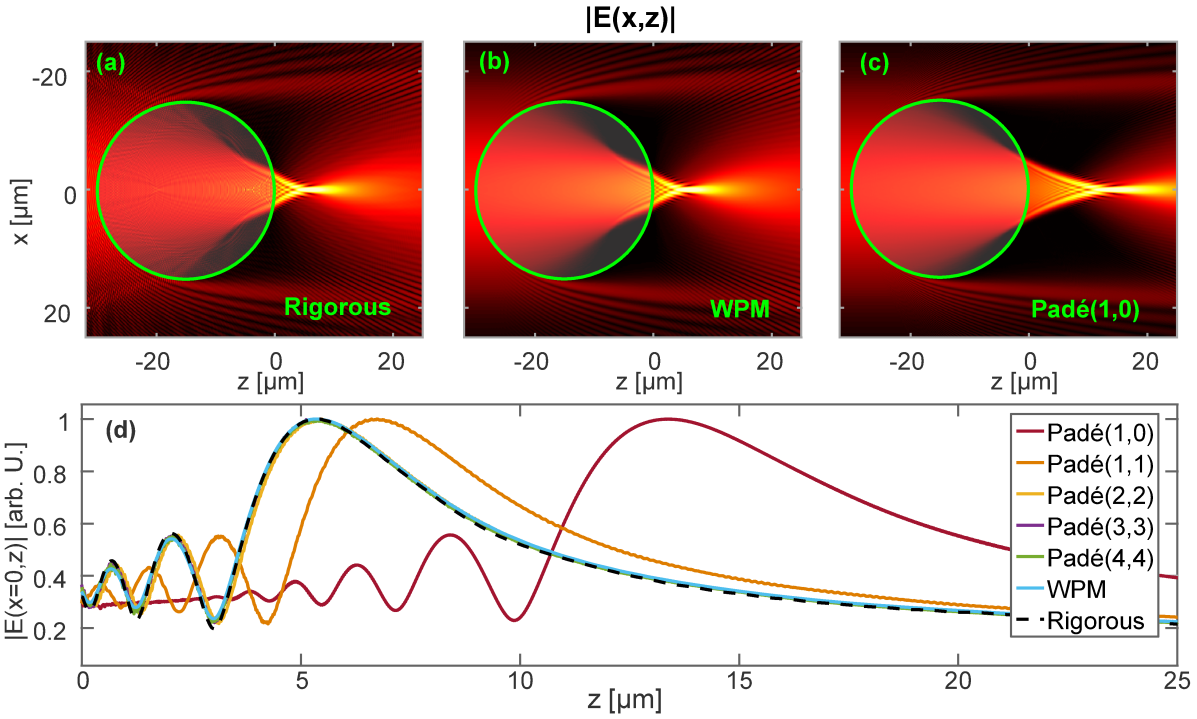

Figure 2.2: Focal field distributions for a Gaussian beam with wavelength $\lambda = 632\,\text{nm}$ and a waist of $\omega_0 = 15\,\mu\text{m}$ focused through a cylindrical rod lens made out of a glass described by a refractive index of $n = 1.5$ with a radius of $r = 15\,\mu\text{m}$ (NA ≈ 0.8). Respectively, in subfigures (b) and (c) the simulations with the WPM and the Padé(1,0) are compared to the rigorous simulation in subfigure (a). In subfigure (d) the normalized field-distributions on the optical axis are compared between the various algorithms.

a cylindrical rod lens described with a refractive index of $n = 1.5$ and a radius of $r = 15\,\mu\text{m}$ are shown. Within these simulations a lateral and longitudinal step size of $\Delta x = \Delta z = \frac{\lambda}{50}$ was chosen. Although in the considered example a strict definition of the numerical aperture is not possible, a notable amount of energy is still connected to spatial frequencies corresponding to a numerical aperture NA$= \frac{k_x}{k_0}$ of approximately NA≈ 0.8 . Behind and inside the micro-optical lens, deviations from the rigorous simulation are found. These are due to back-reflections at the lens surfaces, which are neglected in the unidirectional BPM and WPM algorithms. Nevertheless, the focal region is accurately described by the WPM. This is not the case for the standard Padé(1,0) BPM, where a shift in the focal position is observed. To analyze the shift in the back-focal-distance in more detail, Fig. 2.2 (d) shows the normalized field profile on axis. It becomes evident, that already for the Padé(1,1) BPM formulation the error is strongly reduced and nearly vanishing for the higher order methods. Within the higher order BPMs these effects are reduced, as further corrections beyond the paraxial approximation are considered.

To analyze the error in the focus position in more detail, the back focal distance (BFD), i.e., the maximum intensity on the optical axis, is evaluated for varying radii of the micro-optical lenses (see Fig.2.3 (a)). Here the waist of the incident beam was chosen equal to the radius of the cylindrical lens, which keeps the numerical aperture approximately constant. It turns out,

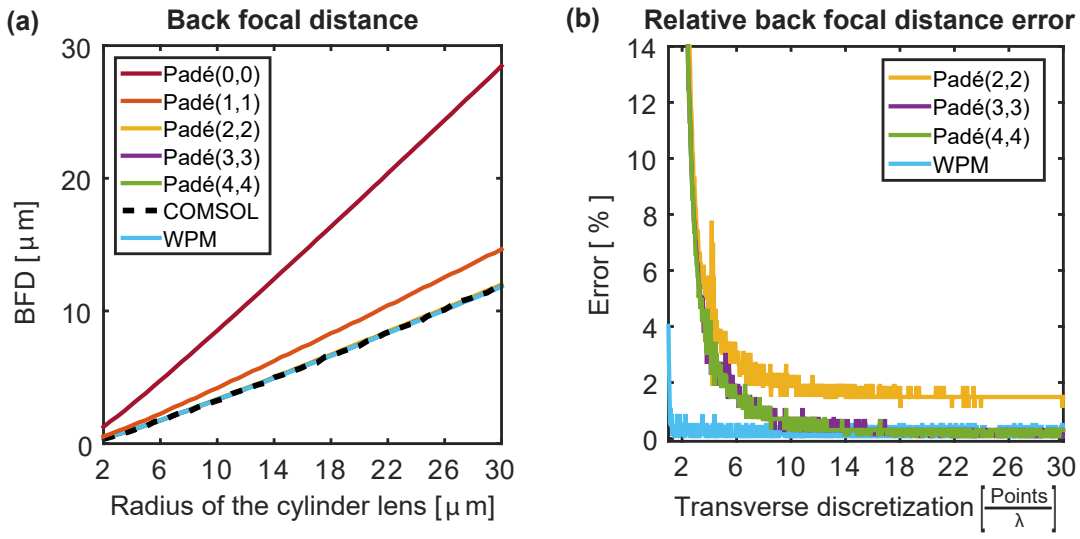

Figure 2.3: (a): Comparison of the calculated back focal distances BFD of the WPM and the different BPMs in comparison to the rigorous simulation for varying micro-optical lens diameters. (b): Relative back focal distance error $\left|\frac{BFD_{\text{Alg.}} - BFD_{\text{Rig.}}}{BFD_{\text{Rig.}}}\right|$ of the individual algorithms related to rigorous simulations. The errors are evaluated for a micro-optical lens with a radius of $r = 15\,\mu\text{m}$ for different transverse discretization densities.

that the WPM as well as higher order Padé BPMs are able to accurately calculate the back focal distance. Within these different simulations a respectively high grid density was chosen ($\Delta x = \Delta z = \frac{\lambda}{50}$). To assess also the convergence of the different methods with the transverse sampling, the relative back focal distance error $\left|\frac{BFD_{\text{Alg.}} - BFD_{\text{Rig.}}}{BFD_{\text{Rig.}}}\right|$ is considered, i.e., the ratio of the error in the back focal distance for the varying algorithms (Alg.) normalized by the back focal distance as extracted from the rigorous simulation (Rig.). This evaluation was performed for a micro-optical lens of radius $r = 15\,\mu\text{m}$ and a longitudinal step size of $\Delta z = \frac{\lambda}{50}$ (see Fig.

2.3 (b)). For the WPM, coarse grid densities of approximately two points per wavelength are sufficient to accurately determine the back focal distance, which closely resembles the Shannon-Nyquist theorem. For the different BPMs a much higher grid density is necessary to achieve converged results. In particular, four times more sampling points are necessary in comparison to the WPM to decrease the error below an error threshold of about 2 percent. This finding is of major importance within the simulation of micro-optical structures, as it has a strong impact on either the computational runtime or equivalently the overall volume that can be simulated. The algorithms of the different formulations of the BPMs in three dimensions are at least scaling according to the square number of field points $N^2 = N_x\, N_y$, as the inevitable sparse matrix inversions have a complexity scaling with the number of nonzero elements. Therefore an increased computational grid density of about four will decrease the computational runtime by a factor of at least 16. A discussion about the influence of a longitudinal sampling density Δz has been omitted here. This issue is connected to the representation of the inhomogeneous medium by a staircase approximation. As a rule of thumb a discretization of $\Delta z = \frac{\lambda}{20}$ results typically in satisfying results. This issue is explained by conventional grating theory [81]. A binary grating achieves a maximum diffraction efficiency of 40.5% in a desired diffraction order. By increasing the number of layers to approximate the blazed profile the overall diffraction efficiency increases. This corresponds to an improved staircase approximation of the blazed grating. In particular, by approximating the ideal blaze profile with 20 layers an overall diffraction efficiency of approximately 99% is achieved.

Regardless of the computational effort of the individual methods, it turned out, that both the WPM and the higher order Padé BPMs are able to accurately describe the focal field characteristics. This might rise the additional question, whether these results only belong to TE-polarization or whether they remain valid also for TM-polarization. This question already was introduced within Sec. 1.1.2 and will be readdressed here. To this end, the individual results within the distinct polarization states will be compared here. In order to derive the results for

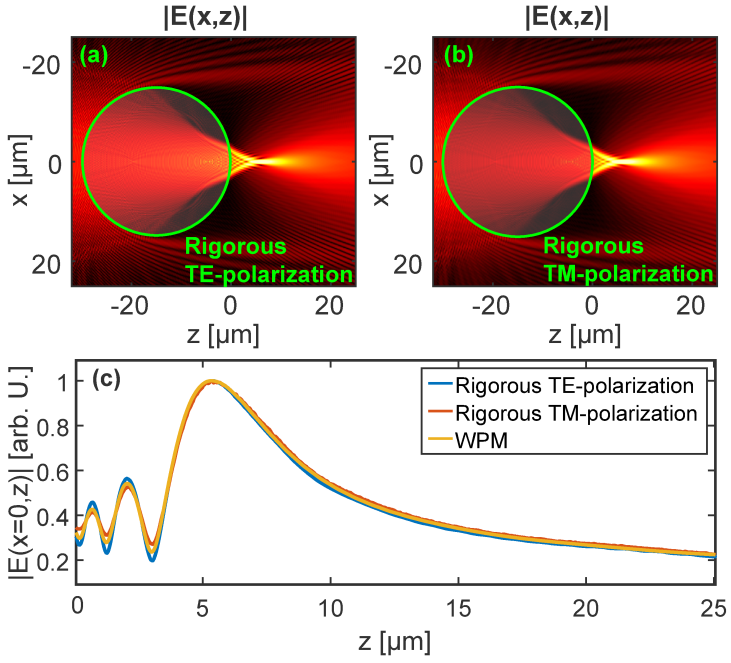

Figure 2.4: (a), (b):Comparison of the focal field profiles in between TE- and TM-polarization for the same scenario as discussed in Fig. 2.2. (c) Comparison of the field profiles on the optical axis in between the rigorous simulations and the WPM.

the TM-polarization state, the aspect is used, that in this case the magnetic field $\mathbf{H} = H_y \mathbf{e}_y$ obeys the Helmholtz-Eqn. (see Sec. 1.1.1). Thus, a formal solution of the Helmholtz-Eqn. can be used for both the electric field in TE-polarization and similar for the magnetic field in TM-polarization [43]. Hence, the electric field distribution in TM-polarization is derived from the magnetic field according to Maxwell's equation 1.2

$$\mathbf{E} \propto \frac{1}{n^2(r,\omega)} \begin{pmatrix} -\partial_z H_y(r,\omega) \\ 0 \\ \partial_x H_y(r,\omega) \end{pmatrix} \quad . \tag{2.5}$$

The respective solutions are compared within Fig. 2.4. For comparability the electric field in TE-polarization is added although being identical to Fig. 2.2 (a). Moreover, in Fig. 2.4 (b) the electric field in TM-polarization, i.e., $|\mathbf{E}| \propto \frac{1}{n^2}\sqrt{|\partial_z H_y|^2 + |\partial_x H_y|^2}$, is shown. It gets evident, that the results in TE- and TM-polarization are visually identical. Minor deviations can be realized for the on-axis field profiles as shown in Fig. 2.4 (c). It is interesting, that the unidirectional result of the WPM lies in between the ones in TE- and TM-polarization. Nevertheless, also within this example it gets evident, that the scalar optical description is well suited to describe the mentioned structure. However, for smaller rod-lens diameters this situation changes and polarization influences rise. These aspects are beyond the scope of this current discussion, as the focus lies on strategies to overcome the limitations of the TEA.

Up to now the accuracies of the individual methods were discussed, but actual computational runtimes were ignored. In a next step, this issue will be evaluated for the three-dimensional case. Therefore, a micro-optical ball lens with a diameter $D = 30\,\mu\text{m}$ is simulated on the grid $L_x \times L_y \times L_z = [60\,\mu\text{m} \times 60\,\mu\text{m} \times 40\,\mu\text{m}]$ with a sampling $N_x \times N_y \times N_z = [1024 \times 1024 \times 1050]$. The computational runtime performed on a machine with an Intel Core i7 3930K processor is shown in the following Table 2.1.

Table 2.1: Computational runtime

	Time [min]		Time [min]
WPM	2.0	Padé(2,2)	99.0
Padé(1,0)	13.6	Padé(3,3)	165.0
Padé(1,1)	62.5	Padé(4,4)	236.1

It turns out that the WPM provides a serious time advantage in comparison to the BPMs for the considered scenario. These respective simulations were carried out on an identical grid density for the individual BPMs and the WPM. In turn, by additionally considering the sampling requirements as outlined previously the time advantage even improves. A more detailed analysis regarding the influence of a total number of points on the computational runtime is omitted as it will not affect the general conclusion.

In particular, the WPM seems superior for the modeling of micro-optical components beyond the TEA as sampling requirements and computational runtime are strongly reduced in comparison to the BPMs. This can open up novel abilities in the characterization and design of micro-optical components. Nevertheless, as outlined in Sec. 1.4 the WPM tends to insta-

bility problems for optical structures with extended longitudinal boundaries, i.e., waveguiding structures. In case these issues are apparent, it is suggested to rely on the BPMs. Then, it is of particular importance to choose the lowest Padé order and sampling density to achieve converged accuracy for a given scenario. Thus, in the following Sec. 2.3.1 an algorithmic approach will be presented to estimate *a-priori* a suitable BPM formulation. Thereby, pitfalls connected to convergence studies of BPM simulations will be discussed.

2.3.1 Accuracy assessment of the beam propagation methods

Beam propagation methods are inevitable numerical tools to study guided wave phenomena. Moreover, as previously shown, these techniques are also well suited to investigate micro-optical components with high numerical aperture and high index contrast. Nevertheless, in three dimensions the computational complexity of the higher-order Padé BPMs is increased substantially, which slows down their computational performance. To this end, a methodology is desirable, which allows to estimate a suitable BPM formulation with a lowest sampling effort, which achieves a required accuracy. The development of such a methodology will be discussed in the following.

According to the discussion of Sec. 1.3, the individual Padé orders provide descriptions of the field evolution operator with increasing accuracy. Moreover, by changing the grid density and the reference index n_{ref}, the accuracy of the BPMs is also affected. Thus, for every simulation scenario a careful convergence analysis should be performed to estimate the trustworthiness of the BPMs. Here, pitfalls are discussed connected to these convergence analyses of BPMs and an easy methodology is proposed to assess a suitable BPM formulation and its grid density *a-priori* to a simulation. The errors of the individual formulations are connected to the phase of a beam. In particular, BPMs do not fulfill the analytic dispersion properties of plane waves $|\mathbf{k}|^2 \neq k_x^2 + k_y^2 + k_z^2$. Thus, errors can be evaluated, by analyzing the propagation constant $k_z(k_x, k_y)$ plane waves evolve in the BPM schemes [48, 54, 65, 82, 83].

To assess the dispersion properties of the BPMs, the propagation of an initial field is considered in a homogeneous medium characterized by a refractive index of n. According to Eqn. 1.8, the field distribution in a subsequent layer is analytically given as

$$\tilde{E}(k_x, k_y, z_0 + \Delta z) = \tilde{E}(k_x, k_y, z_0) e^{ik_z \Delta z} \quad .$$

This allows to estimate the propagation constant $k_z^{\mathrm{BPM}}(k_x, k_y)$ of the BPM as

$$k_z^{\mathrm{BPM}}(k_x, k_y) = \frac{1}{i\Delta z} \ln\left(\frac{\tilde{E}(k_x, k_y, z_0 + \Delta z)}{\tilde{E}(k_x, k_y, z_0)}\right) \quad , \tag{2.6}$$

by relying on an initial beam of small waist propagated by the different BPMs [1]. Moreover, the propagation angle α of a plane wave is derived as $\alpha = \tan^{-1}\left(\frac{k_x}{k_z^{\mathrm{BPM}}}\right)$. This allows to assess the

[1] By numerically evaluating this equation special care has to be taken. The simulation domain should be large enough, that no field components are damped due to the boundary conditions. This, of course, would affect respective results. Moreover, by choosing only a single step Δz for the evaluations, additional numerical problems might arise as individual field changes are small in subsequent planes. It is suggested to evaluate fields over several steps. Overall, errors of these evaluations are directly visible in the retrieved dispersion curves and they do not appear smooth. Then, these mentioned parameters should be changed.

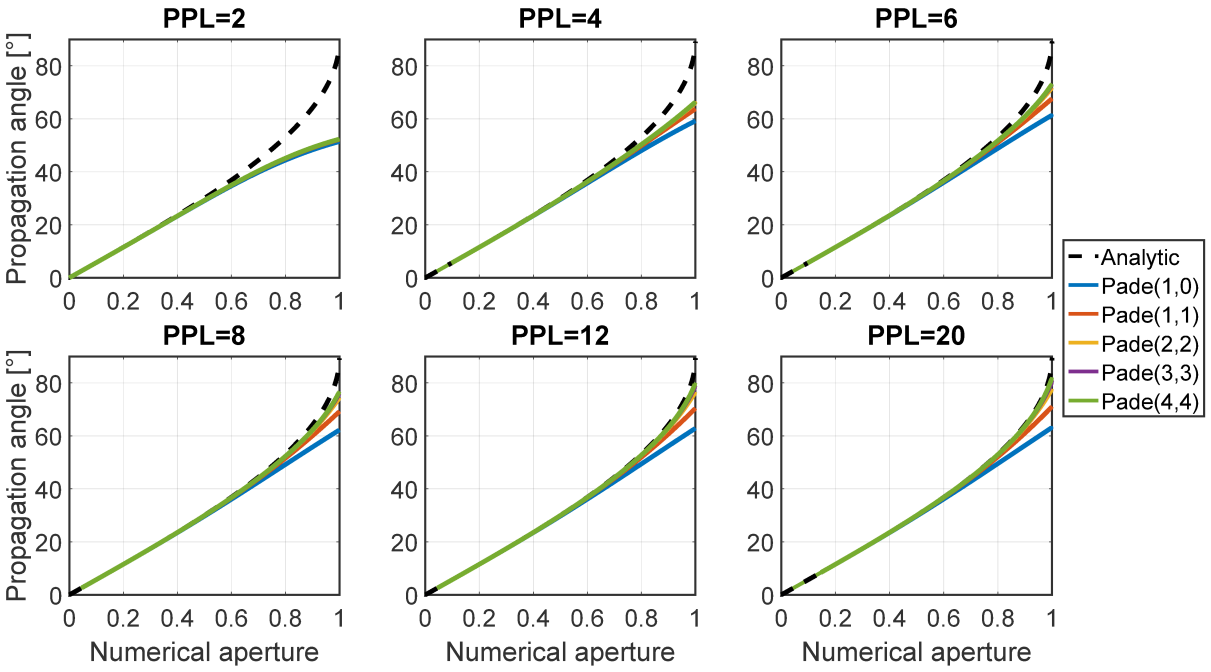

Figure 2.5: Associated propagation angle of plane waves for the different BPM formulations depending upon the analytic numerical aperture $NA = \frac{k_x}{k_0}$. The refractive index of the surrounding medium is chosen equal to the reference index n_{ref} as $n = 1$. Along the longitudinal z-axis a spacing $\Delta z = \frac{\lambda}{20}$ was chosen. Within the respective subfigures the transverse grid density is varied and the lateral spacing Δx is defined in fractions of the initial wavelength λ as $\Delta x = \frac{\lambda}{\mathrm{PPL}}$, where PPL denotes "points per wavelength".

BPMs by comparing their propagation behavior to the analytic one as shown in Fig. 2.5. For small numerical apertures, i.e., paraxial conditions, the BPMs predict the propagation angles correctly, while for non-paraxial conditions the angle is underestimated. Roughly speaking, this allows to interpret errors connected to the BPMs as negative spherical aberration, which leads to a shift of the focal position of a lens. Thus, these aspects can serve as explanation for the findings of Sec. 2.3.

It turns out that the error connected to the grid density is superordinate to the individual higher orders of the Padé approximation. In other words, the different Padé approximations provide more accurate results only for respectively high grid densities. This aspect needs to be interpreted as a severe pitfall for convergence analyses of BPMs. In particular, one might judge on the accuracy of a BPM simulation by considering a respective scenario within the different Padé-approximations. If no accuracy improvement is achieved by changing between the individual Padé BPMs, one might think the simulation results are converged. Hence, the lowest order Padé BPM is chosen for which the accuracy improvement stagnates. This approach fails, if in the beginning of the convergence study the grid spacing is chosen too coarse. Then, no difference is observed in the simulations for different Padé orders and one might trusts a none trustworthy BPM simulation. To overcome this pitfall, a convergence study needs to be founded on a respective high grid density and should only be lowered if possible. Nevertheless, these kind of convergence studies are cumbersome and might require large computational resources. Thus, an alternative *a-priori* assessment of the BPMs is desirable.

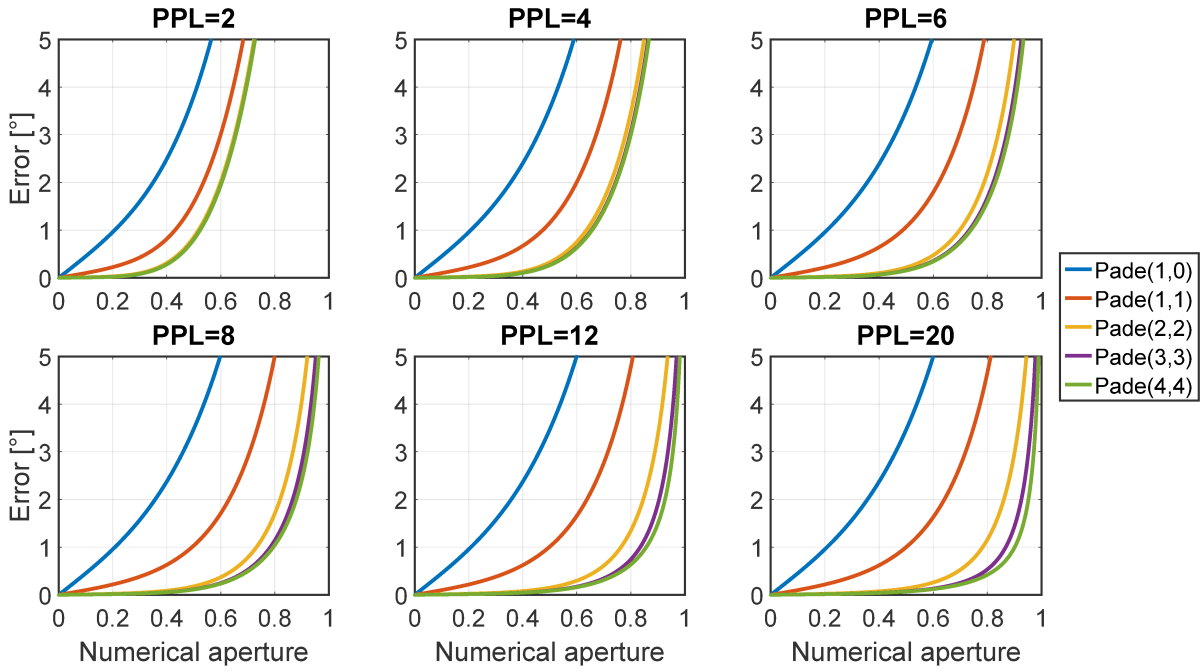

Figure 2.6: Error in the propagation angle of plane waves for the different BPM formulations with respect to the analytical value. The refractive index of the surrounding medium is chosen as $n = 1$ and differs from the reference index within the BPM simulation $n_{\text{ref}} = 1.5$. Along the longitudinal z-axis a spacing $\Delta z = \frac{\lambda}{20}$ was chosen. Within the respective subfigures the transverse grid density is varied.

A valid BPM-formulation and a required grid density can be estimated by evaluating the errors of the BPM in a worst-case scenario. In particular, the errors are assessed for the case of a homogeneous medium, whose refractive index n_e is chosen as the maximum deviation to the reference index, i.e., $n_e = \{n(x, y, z) : \ |n(x, y, z) - n_{\text{ref}}| = \text{max.})\}$. This error is shown in Fig. 2.6 for a reference index of the BPM of $n_{\text{ref}} = 1.5$ and a homogeneous medium characterized by a refractive index of $n = 1$ (This resembles the situation as discussed in Sec. 2.3). From the knowledge of a typical numerical aperture of the scenario and an error threshold, a valid BPM-formulation can be assessed. Then, one chooses the lowest order Padé-approximation and grid-density for which the errors are smaller than the threshold.

The major challenge in this approach is the explicit choice of the numerical aperture and the error threshold. The prior can be determined based on first order principles. Often, the numerical aperture is a characteristic measure in a specific optical system and is known *a-priori* to a certain extent. For instance, it defines the resolution of optical systems or the acceptance angles of optical fibers. The major challenge then belongs to the fixation of an error-threshold. Choosing this value is specific to the problem itself and requires profound knowledge about the accuracies that should be reached. For the example discussed in the previous section the numerical aperture approximately equaled $NA \approx 0.8$ and a relative error threshold of 1 percent should be sufficient, i.e., an error $\Delta\alpha$ in the propagation angle $\Delta\alpha < 3.6°$. According to Fig. 2.6 this error threshold is met for a Padé(2,2)-BPM with a grid density of approximately 6 points per wavelength. Hence, this estimation closely resembles the conclusions that were drawn in Sec. 2.3 along with the discussion of Fig. 2.3.

2.3.2 Summary

For the simulation of micro-optical structures different algorithmic approaches exist to simulate their respective response. On the one hand, the thin-element approximation is often considered. It describes the impact of the micro-optical element as the induced phase retardation an incoming wavefront is altered. This approach is founded on a geometric optical perspective and provides an analytic connection between optical properties of a wave and the topology of the component. This enables fast simulations and the algorithm is widely disseminated for the design of diffractive optical elements. Nevertheless, the underlying physical model is quite restrictive. In particular, any ray bending inside the optical component is neglected. As a consequence, any change in an incoming intensity due to ray deflections are neglected as well. This restricts the application of the TEA to respectively thin-elements, where these influences are only of minor importance. By relying on an improved geometrical model these downsides can be resolved [49–52]. Nevertheless, any influence of diffraction occurring inside the component is still neglected and extended algorithms are required to overcome these limitations. To this end, different beam propagation methods were evaluated against a modified formulation of the wave propagation method. In particular, the WPM algorithm was reformulated for step index structures, which allows a serious time improvement in this case. It turns out, that both the beam propagation methods and the reformulated wave propagation method can accurately simulate micro-optical components beyond the TEA. Nevertheless, there are strong differences in computational runtime and sampling requirements. In particular, the WPM can provide accurate results on a lowered grid density and a simultaneous improvement in computational runtime. As a consequence the WPM is ideally suited to overcome the limitations of the TEA. Nevertheless, in case of gradient index media these time improvements diminish. Moreover, for the simulation of guided wave phenomena the BPMs seem superior in comparison to the WPM. To be precise, the WPM suffers from certain stability issues in these cases. In turn, BPMs are widely disseminated for these simulation scenarios and provide accurate results.

2.4 Hankel-based wave propagation method

Within the previous Sec. 2.3 the ability of the different Padé BPMs and the WPM were discussed to overcome the limitations of the TEA. It turned out that the WPM can simulate micro-optical elements with accuracies close to rigorous ones with a substantially increased computational performance in comparison to the BPMs. This can enable improved virtual prototyping of micro-optical elements and thus enhance their respective designs. Here, the WPM is extended into a rotationally symmetric formulation (Hankel-WPM), which exploits this kind of underlying symmetry. This allows to reduce the efforts of a three-dimensional simulation, characterized by Cartesian coordinates $(x, y, z)^T$, into a two-dimensional one, described by coordinates $(r = \sqrt{x^2 + y^2}, z)^T$. This can further reduce the computational effort by up to two orders of magnitude. In the following the theoretical framework of the Hankel-WPM will be derived. To this end, the angular spectrum of plane wave decomposition algorithm needs to be reformulated for cylindrical coordinates. This formal derivation is shown in Appendix B and its most important aspects are discussed here.

An initial scalar light field $E(x, y, z_0)$ can be decomposed into angular harmonics

$$E(r, \varphi, z_0) = \sum_{m=-\infty}^{\infty} E_m(r, z_0) e^{im\varphi} \ , \tag{2.7}$$

where $x = r\,\cos(\varphi)\,,\ y = r\,\sin(\varphi)$. The individual $E_m(r, z_0)$ are given as

$$E_m(r, z_0) = \frac{1}{2\pi} \int_{-\pi}^{\pi} E(r, \varphi, z_0) e^{-im\varphi}\, d\varphi \ ,$$

where m describes the azimuthal angular dependence. The propagation of the light field along the optical axis by a distance $\Delta\, z$ is then given by (see Appendix B)

$$E(r, \varphi, z_0 + \Delta z) = \sum_{m=-\infty}^{\infty} e^{im\varphi} \mathcal{H}_m{}^{-1}\{\mathcal{H}_m\{E_m(r, z_0)\} e^{ik_z\, \Delta\, z}\}, \tag{2.8}$$

$$k_z(k_r) = \sqrt{k_0{}^2 n^2 - k_r{}^2} \ , \quad k_0 = \frac{2\pi}{\lambda} \ ,$$

where $\mathcal{H}_m\{E_m(r, z)\}$ and $\mathcal{H}_m{}^{-1}\{E_m(k_r, z)\}$ are the Hankel-transform of order m and its inverse respectively

$$\mathcal{H}_m\{E_m(r, z)\} = \tilde{E}_m(k_r, z) = \int_0^{\infty} E_m(r, z)\, J_m(k_r\, r)\, r\, dr \ ,$$
$$\mathcal{H}_m{}^{-1}\{\tilde{E}_m(k_r, z)\} = E_m(r, z) = \int_0^{\infty} \tilde{E}_m(k_r, z)\, J_m(k_r\, r)\, k_r\, dk_r \ .$$

In Eqn. 2.8, a summation over angular harmonics occurs, which has to be truncated for numerical reasons. Hence, the computational performance of the algorithm is intrinsically linked to the number of angular harmonics that need to be considered. In particular, for a general plane wave described by a propagation angle $\alpha \neq 0$ with respect to the optical axis, a high number of angular harmonics needs typically to be considered (see appendix B). Then, the original formulation of the WPM is better suited in most cases. However, often initial light fields only have a low number of angular harmonics. As an example, light emitted by a rotationally symmetric optical fiber generally consists of few modes with low angular momentum m. Moreover, one of the most important cases is a rotationally symmetric incident field on-axis $E(r, \varphi, z_0) = E(r, z_0)$. This is the case, e.g., for a Gaussian beam, where only $m = 0$ needs to be considered

$$\begin{aligned} E(r, \varphi, z_0 + \Delta z) &= \mathcal{H}_0{}^{-1}\{\mathcal{H}_0\{E(r, z_0)\} e^{ik_z \Delta z}\}, \\ k_z(k_r) &= \sqrt{k_0{}^2 n^2 - k_r{}^2} \ . \end{aligned}$$

In the following, the rotationally symmetric formulation of the WPM will be introduced. Again, the inhomogeneous medium is assumed to be decomposed into a finite number L of pairwise disjoint and homogeneous subregions with refractive index n_α. Then, the refractive index distribution $n_{z_0}(r) = n(r, z_0)$ is given in a subsequent layer as $n_{z_0}(r) = \sum_{\alpha=1}^{L} n_\alpha \Theta_\alpha^{z_0}(r)$, where

$$\Theta_\alpha^{z_0}(r) = \begin{cases} 1 & n_{z_0}(r) = n_\alpha \ , \\ 0 & n_{z_0}(r) \neq n_\alpha \ , \end{cases}$$

is the characteristic function of the subregion α.

The propagation equation for a single angular component $E_m(r, z_0)$ through a medium with a rotational symmetric index distribution $n(r, z_0)$ can be written as

$$E_m(r, z_0 + \Delta z) = \sum_{\alpha=1}^{L} \Theta_\alpha^{z_0}(r) \mathcal{H}_m^{-1} \left\{ e^{ik_z^\alpha \Delta z} \mathcal{H}_m \left\{ E_m(r, z_0) \right\} \right\} , \tag{2.9}$$
$$k_z{}^\alpha(k_r) = \sqrt{k_0{}^2 n_\alpha{}^2 - k_r{}^2} .$$

Therefore, the propagation of the initial field through the inhomogeneous medium characterized by $n(r, z)$, is described as the iterative propagation through individual layers. In every layer, described by K differing refractive indices n_k, K individual propagation steps along the distance Δz in the equivalent homogeneous medium described by n_k are performed. Afterwards the individual fields are merged according to the characteristic function of the subregion k. Moreover, the different angular components $E_m(r, z)$ are propagated individually through the system, as their angular momentum m remains preserved due to the rotational symmetry of the refractive index distribution. The total field distribution is given by the sum over all angular harmonics as

$$E(r, \varphi, z) = \sum_{m=-\infty}^{\infty} E_m(r, z) e^{im\varphi} . \tag{2.10}$$

To achieve optimal computational performance of the algorithm, an efficient implementation of Eqn. 2.8 is of special importance. Here, the algorithm as proposed by Fisk-Johnson [84–86] is considered for the efficient and robust computation of numerical Hankel transforms. This method preserves important properties of the analytic Hankel-transform in a similar way as the numerical Fast-Fourier-Transform does with the analytic Fourier-transform. It should be noted that the transverse sampling points r_{dht} for the evaluation of the discrete Hankel-transform are connected to the roots of the corresponding Bessel-functions. In particular, the radial coordinate $r = 0$ is not included for the important Hankel-transform of order $m = 0$. While these aspects have no influences for the Hankel-WPM it could be a drawback for the post-processing of the simulations. The evaluation of fields along the optical axis often is of outermost importance. This deficiency of the discrete Hankel transform can be lifted by an additional interpolation step [87, 88], or an explicit evaluation as discussed within Sec. 2.4.1.

2.4.1 False light evaluations of diffractive lenses

In the following the Hankel-WPM will be assessed by investigating diffractive lenses. This particular example is of practical importance and similarly a representative scenario to assess the proposed algorithm. These components are of particular importance within the design of modern optical systems. In particular, their application not only enables to reduce the overall size of optical systems but can also increase their optical functionality. This unique feature originates from the combination of refractive and diffractive properties within these lenses. Especially the chromatic characteristics are not only influenced by a wavelength dependent refractive index but also by diffractive influences, which results in an anomalous dispersion. This can be used for

chromatic correction. In contrast to conventional achromats these so-called hybrid achromats are composed of one material only. Therefore, these hybrid lenses are not only interesting to miniaturize optical systems but are particularly interesting if the glass choice is restricted, i.e., in infrared optics or miniaturized optical systems produced by direct laser writing [89–93]. As a major drawback, these lenses inherently cause diffractive false light, i.e., light scattered into unwanted diffraction orders. Therefore, the realistic estimation of the induced false light during the optical design process is of major importance to predict the performance of the optical system.

To this end, the Hankel-WPM will be assessed in comparison to the TEA to predict diffractive false light. These results are referred to rigorous simulations of the scalar Helmholtz equation performed with Comsol. It turns out, that the Hankel-WPM achieves accuracies close to rigorous ones, while the TEA overestimates the performance of these lenses. In particular, at the rings of segmentation of these lenses diffractive influences emerge, which leads to the excitation of higher diffraction orders and which lowers the overall performance of these devices. These aspects are not predicted by the TEA. This finding is also of particular importance in the broader sense of evaluating diffractive optical elements. These devices have similar steep edges and they lead to the excitation of higher diffraction orders, which are seen as a strong zeroth order straylight peak or ghost images even for the design wavelength. These aspects and especially their implications on the design of DOEs will also be addressed within the following section.

To assess the Hankel-WPM a diffractive lens with a focal length of $f = 0.8$ mm and an entrance pupil diameter of EPD ≈ 0.38 mm was chosen based on the phase profile of a thin lens $\varphi(r) = -\frac{2\pi}{\lambda_0}\frac{r^2}{2f}$ for the design wavelength $\lambda_0 = 500$ nm. The diffractive lens was used in first diffraction order, i.e., the maximum segmentation height equals an induced optical path length difference of one wavelength λ_0 and the corresponding surface sag was calculated with Eqn. 1.19. Such a diffractive lens could be used for the design of endoscopic optical systems [94]. Moreover, these size dimensions still allow for rigorous solutions of the Helmholtz equation with Comsol. In particular, for this situation a Comsol-model was used, which solves the Helmholtz-Eqn. in rotationally symmetric coordinates $(r = \sqrt{x^2 + y^2}, z)^T$ and thus allowed to assess diffractive lenses of these dimensions. As initial field, a collimated beam along the optical axis was used and therefore only the angular order $m = 0$ needs to be considered. The Hankel-WPM needs less than 10 seconds of computational time to simulate the diffractive lens on a computational grid of $[N_r \times N_z] = [4000 \times 400]$. The three dimensional Cartesian formulation of the WPM requires approximately two orders of magnitude more in computational runtime. Referring to the Comsol simulations there is a time improvement of more than 3 orders of magnitude, even excluding the time needed for creating the mesh and the interpolation of the field data onto a regular grid.

In Fig. 2.7 (a) the field distribution in close proximity to the diffractive lens is shown. For better clarity only the inner part $r < 75\,\mu$m is evaluated. Strong amplitude modulations at the discontinuities of the lens profile are found. These effects are not predicted within the TEA-formalism, where diffractive lenses are described as pure phase elements, which do not influence the amplitude of the incident field. Thus, analyzing these influences and their impact for the overall performance of the component allows to assess limitations of the TEA. Based on these

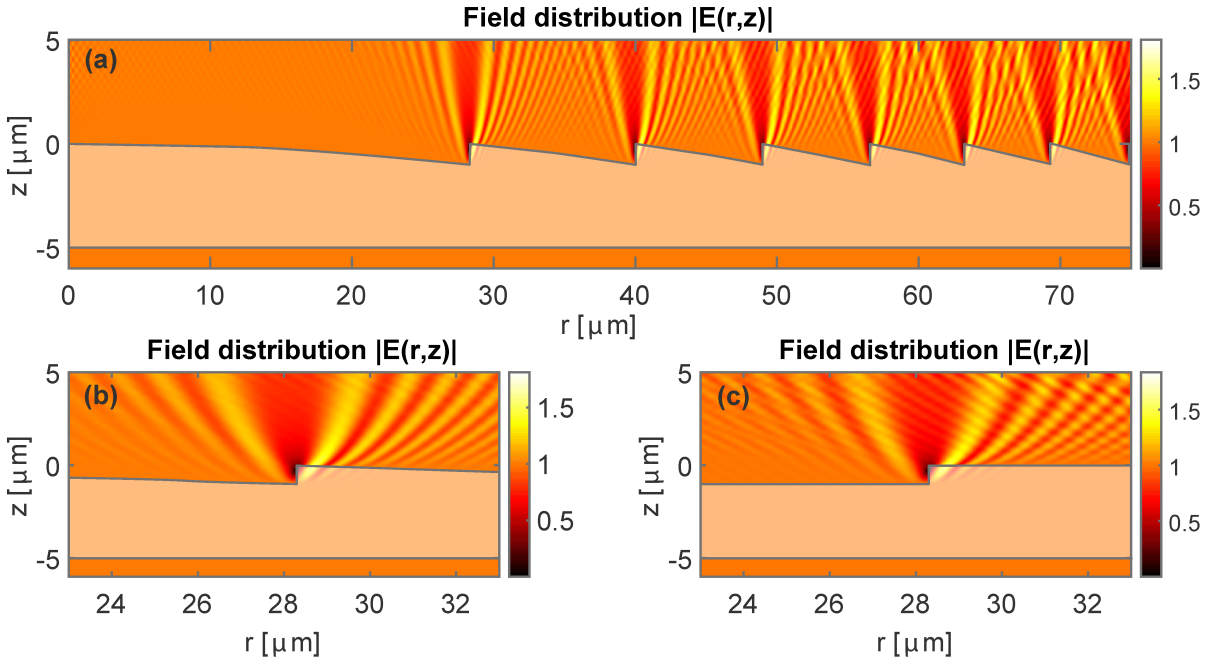

Figure 2.7: (a) Visualization of the field distribution in close proximity to the diffractive lens simulated by the Hankel-WPM (Axis not to scale). The diffractive lens is characterized by a focal length of $f = 0.8$ mm and an entrance pupil diameter EPD of approximately EPD ≈ 0.38 mm. The field distribution is shown for the design wavelength $\lambda_0 = 500$ nm. (b),(c) Respectively, the field distribution at the first ring of segmentation is shown in between the diffractive lens and a binary structure inducing a phase shift of 2π for the design wavelength.

insights strategies can be developed to circumvent these challenges.

The amplitude modulations arise at the rings of segmentation of the diffractive lens and are shown in more detail in Fig. 2.7 (b). One might think, these effects originate from ray bending at the refractive surface parts, which are ignored within the framework of the TEA (see Fig. 1.3). Then, also the amplitude is affected and for the diffractive lens a shadowed region around the rings of segmentation emerges. Nevertheless, this aspect does not provide the fundamental explanation of the phenomenon and is only of minor importance. In particular, the emergence of the modulations is a topological effect of the sample, present also in the absence of ray bending. To this end, the field distribution of a binary step profile is shown in Fig. 2.7 (c). This component induces a geometric phase-delay of 2π for the design wavelength λ_0 and thus corresponds to a neutral element in the framework of the TEA. For this component the radii of the individual rings were chosen equal to the ones of the diffractive lens to enhance comparability. Referring to the amplitude modulations of the diffractive lens an high degree of similarity is found. This suggests that these modulations are of the same fundamental origin. Since within the example of the binary profile no geometric ray deviations emerge, the amplitude modulations are entirely of wave-optical nature. To explain the effect one should consider the evolution of a plane wave traversing the binary profile. With increasing propagation distance the phase difference on either side of the actual binary structure increases. Then, directly at the edges of the profile the phase of the wave gets disrupted and thus becomes an uncertain or singular value. This aspect originates the fundamental amplitude modulations, as an uncertain phase value will cause a vanishing intensity at the corresponding positions. This effect, of course, is not only apparent

for diffractive lenses but moreover also for general diffractive optical elements. In these cases, it provides an explanation for perturbations apparent in a realized intensity distribution. In case of a Fresnel-hologram the rings of segmentation can directly be visible [95, 96] and for Fourier-holograms zeroth order false light is encountered [97]. To overcome these limitations a design algorithm of DOEs should be optimized to circumvent the generation of steep edges in the final surface sag. Nevertheless, this also requires a manufacturing process, which is able to produce these smooth surface sag profiles. These aspects will be discussed in chapter 5 in detail, where the realization of freeforms for beam shaping on optical fiber tips is discussed.

To assess the impact of the modulations in the amplitude on the performance of the diffractive lens, the field distribution along the optical axis is evaluated for the design wavelength $\lambda_0 = 500$ nm in Fig. 2.8. Due to spherical aberration present for the diffractive lens considering the paraxial parabolic profile, the focal position z_{Foc} related to the maximum field strength on the optical axis is shorter than the nominal focal length of $f = 0.8$ mm. Moreover, larger deviations are apparent at the position around $z \approx 0.36$ mm. There, a peak of increased field strength is apparent, which is not predicted by the TEA. This corresponds to a false light peak, which degrades the image quality. The appearance of the peak can be discussed on the base of diffractive lens theory. Then, diffractive lenses are understood as a blazed radial grating within the TEA formalism. The individual diffraction orders p of this radial grating are related to individual focal lengths [98]

$$f_p = \frac{\lambda_0}{\lambda}\frac{f}{p}\,, \tag{2.11}$$

for wavelengths different from the design wavelength λ_0. Within the description of the TEA for the design wavelength $\lambda = \lambda_0$ only the first diffraction order is expected, corresponding to the nominal designed focal length f of the diffractive lens. The mentioned diffractive influences, which are not considered within the TEA, lead to the excitation of higher diffraction orders.

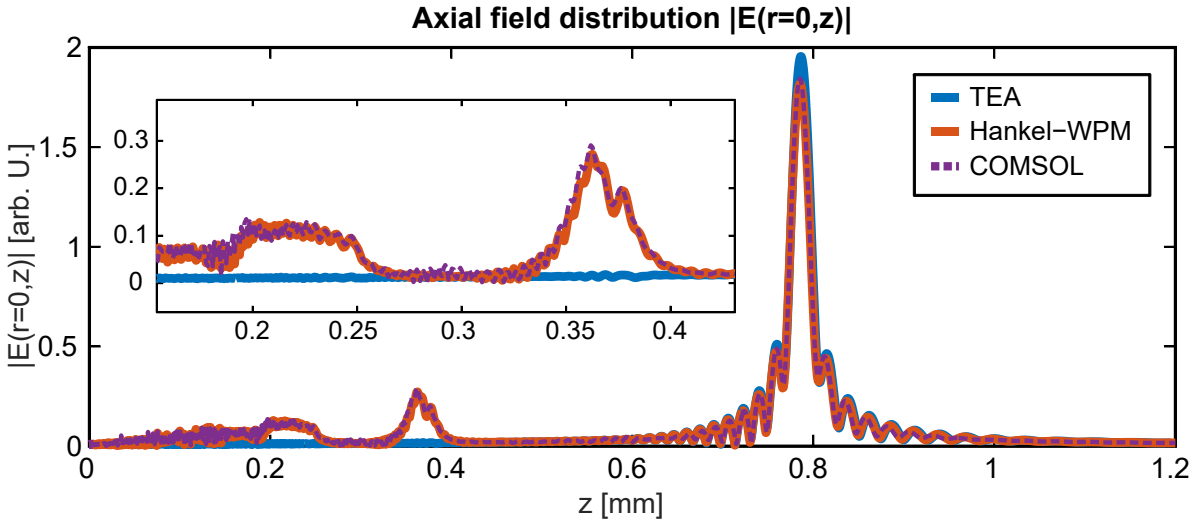

Figure 2.8: The field distribution $|E(r = 0, z)|$ along the optical axis is shown for $\lambda_0 = 500$ nm as comparison between the Hankel-WPM, the COMSOL simulation, and the thin-element approximation.

The apparent peak around $z \approx 0.38$ mm in Fig. 2.8 then corresponds to the second diffraction order of the diffractive lens and induces unwanted false light even for the design wavelength λ_0. While false light usually is considered as a rather statistical effect, which simply reduces the contrast of an image, this situation differs for diffractive lenses. Then, every individual order appears as a defocussed image point, leading to a halo-effect in the actual image plane. This can strongly disturb the visual perception of an image and is known to be a substantial issue for modern virtual reality glasses and camera objectives using diffractive lenses [99, 100]. This

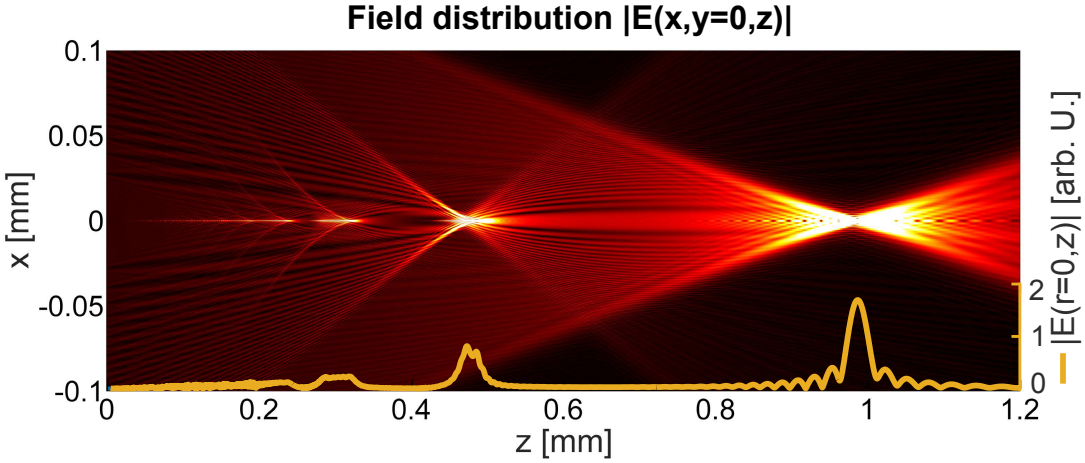

Figure 2.9: The field distribution $|E(x, y = 0, z)|$, simulated by the Hankel-WPM, is shown for the wavelength $\lambda = 400$ nm.

aspect of diffractive lenses is evaluated within Fig. 2.9, where the field distribution $|E(r, z)|$ visualizes the multi focus effect of diffractive lenses. There the field distribution is shown for a wavelength of $\lambda = 400$nm.

In an optical design these false light influences should be taken into account in order to evaluate the performance realistically. While within the TEA formalism closed form expressions exist to predict the false light [101], an extended methodology is required here. To evaluate the light power directed into the unwanted diffraction orders, the ratio of radially integrated light power in the focal point z_{Foc}, i.e., the maximum intensity on the optical axis, enclosed in a radius of $r_{\mathrm{Foc}} \leq 10\,\mu$m is related to the total light power directly behind the diffractive lens

$$\eta = \frac{\int_{r=0}^{r_{\mathrm{Foc}}} |E(r, z_{\mathrm{Foc}})|^2 \, r \, dr}{\int_{r=0}^{\infty} |E(r, z=0)|^2 \, r \, dr} \, . \tag{2.12}$$

Thus, Eqn. 2.12 describes the diffraction efficiency, i.e., the relative amount of light power in the prescribed focal position. Assuming an equivalent ideal lens, described by an Airy intensity distribution, a maximum diffraction efficiency of $\eta = 0.985$ is achieved, since not the entire light power is encircled in the corresponding radius defined by r_{Foc}. Deviations from this ideal value describe the amount of false light scattered into different orders. As the influence of false light is of interest, the encircled energy is referenced against the field behind the diffractive lens. Losses due to reflections, which occur in the rigorous simulations, are thus excluded as they do not affect the diffractive false light, i.e., light in unwanted diffraction orders influencing the field distribution in the focal region. To find and evaluate the focal position z_{Foc} related to the

maximum intensity on the optical axis, the field distribution on the optical axis is calculated directly from the spectrum as obtained behind the diffractive lens at a position $z = 0\,\mu\text{m}$

$$E(r = 0, z) = \int_0^\infty \tilde{E}_0(k_r, z = 0)\, e^{ik_z z}\, k_r\, dk_r \ , \tag{2.13}$$

which is derived by evaluating Eqn. 2.8 on the optical axis analytically. After finding the position z_{Foc}, the field behind the diffractive lens is propagated into the focal position to evaluate Eqn. 2.12. Moreover, to increase the numerical resolution of the focal field inside the radius r_{Foc} the interpolation algorithm as proposed by Norfolk in [87] is applied.

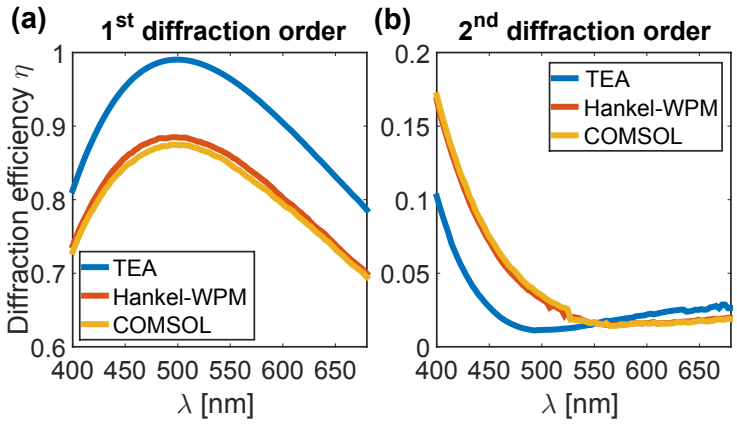

Figure 2.10: (a) Diffraction efficiency in the first diffraction order, i.e., the relative energy ratio in the prescribed focal position f. (b) Relative amount of energy in the undesired focal position f_2.

These diffraction efficiencies are calculated for the first and second diffraction order. While the prior describes the relative amount of energy in the desired focal point f, the latter describes the relative amount of false light in the undesired focal point f_2 according to Eqn. 2.11. In Fig. 2.10 (a) and (b) the corresponding diffraction efficiencies are shown in comparison to the rigorous simulation and the TEA. For the TEA a diffraction efficiency for the design wavelength λ_0 in the desired first diffraction order is found to be smaller than the ideal value of one. This effect is caused by the evaluation of diffraction efficiencies according to Eqn. 2.12. A residual amount of energy will not be encircled within a radius as defined by r_{Foc}. Therefore the ideal value of one in the diffraction efficiency cannot be reached within the model. Moreover, the diffraction efficiency in this case for the second diffraction order is larger than zero, since a finite field energy is encircled within the radius r_{Foc} even for a vanishing second diffraction order.

By comparing to the rigorous simulation it is evident that the Hankel-WPM can precisely calculate the diffraction efficiencies, and thus the diffractive false light, in both the first and second diffraction order. This is not the case, if one relies on the TEA, where deviations of up to 12 percent are present. The TEA overestimates the diffraction efficiency in the desired first diffraction order and underestimates the amount of induced false light. Moreover, for the second diffraction order, the TEA also predicts a qualitatively different spectrally resolved diffraction efficiency. These aspects could lead to misjudgments within an optical design process while relying on the TEA. The Hankel-WPM allows more accurate simulations of diffractive lenses beyond the TEA, which allows the efficient and realistic assessment of false light induced by diffractive lenses.

2.5 Summary

In this chapter different algorithms were discussed to overcome the limitations of the TEA. On the one hand, a reformulation of the original WPM algorithm was introduced and evaluated against the individual formulations of the Padé BPMs. As a result, the modified formulation of the WPM shows superior characteristics in comparison to the different Padé BPMs, as accurate simulations are achieved with an enhanced computational performance, while simultaneously the demands onto the computational grid-density are reduced. Thus, the WPM provides the potential to overcome the limitations of the TEA. This ability of the WPM to simulate micro-optical elements with high accuracy and high computational efficiency enables the improved virtual prototyping of these components. This can improve their optical design and therewith their quality and optical functionality. Moreover this also can open up novel abilities to model and characterize micro-optical elements.
In a further step, the WPM was extended into a rotationally symmetric formulation called the Hankel-WPM and exploits an underlying rotational symmetry of the refractive index distribution. This algorithm was assessed for the characterization of diffractive lenses and showed superior characteristics to predict false light in comparison to the TEA. For the investigated scenario an additional time improvement of approximately two orders of magnitude was found in comparison to the Cartesian formulation of the WPM. Overall, this can enable the realistic estimation of the performance of diffractive lenses within an optical design. Moreover, this example has the potential to provide additional insights for the design of diffractive optical elements. In particular, steep edges in the surface sag of a DOE lead to diffractive influences, which lower their performance and which are not predicted by the TEA. Hence, a design algorithm for DOEs should avoid the generation of steep edges in the surface sag. Thus, to realize DOEs of highest diffraction efficiency, steep edges should be avoided whenever possible. These aspects are discussed in detail in Sec. 5.1.1.

Part III

Characterization and Design of Micro-Optical Structures

The previously developed numerical simulations tools can open up novel avenues to design, model and characterize micro-optical systems. These aspects are discussed in the following for selected application scenarios. On the one hand, in the appending chapter glass matrix distortions are discussed, which might occur after the inscription of fiber Bragg gratings. In this case, a specifically tailored light-sheet side illuminates an optical fiber. Due to a photosensitivity of the fiber core, the incident field causes structural modifications of the refractive index distribution. Beside these intended structural changes, additional distortions in the glass matrix of the fiber might arise. Their appearance is reproducible and shows a distinct symmetry. The origin of these modifications were not revealed in depth and therewith a solution strategy was not available. Based on numerical simulations of the situation a deeper understanding of these parasitic structural changes is gained. These insights are used to develop a solution strategy and these results are discussed in chapter 3.
In the subsequent chapter 4 a non-invasive metrology method to characterize optical fibers is discussed. Optical fibers are one of the most important building blocks in modern telecommunication- and laser systems. Thereby, demands on the accuracy of realized fibers are steadily increasing. To this end, characterization techniques that enable the monitoring of fiber parameters during the manufacturing process are of growing importance. To this end, a metrologic characterization technique, similar to an in-line holographic measurement principle, is introduced. In particular, the investigated fiber is side-illuminated by a coherent beam and the diffraction response is evaluated on a distant screen. In the considered scenario strong index contrast, e.g., glass to air, are involved. This prohibits the application of typical approximations considered within in-line holography. Alternatively, the wave propagation method is used to describe the scenario. By a direct comparison between simulations and measurements, a parameter retrieval is performed and structural properties, e.g., the core and cladding diameter, are assessed.
Finally in chapter 5 an integrated beam shaping concept is introduced to realize complex illumination patterns in a focal region. To this end, a freeform is realized on the tip of an optical fiber, which redistributes the fundamental eigenmode into a complex illumination pattern. Within the design process, limitations of the thin-element approximation are considered. As discussed in the preceding section, steep edges provoke diffractive influences, which are not predicted by the TEA. As a consequence, special care should be taken in order to restrict surface gradients and to omit steep edges in a surface profile. Considering these aspects, high diffraction efficiencies could be realized with unprecedented accuracy in the realized target field distributions.

3 Glass-Matrix Distortions during Fiber Bragg Grating Inscription

In this chapter structural modifications of the glass matrix after fiber Bragg gratings inscriptions are discussed. These results were developed in a collaboration with Tino Elsmann from the *Leibniz Institute of Photonic Technology (IPHT)*. In particular, all the investigated samples and measurements were provided by Tino Elsmann. The development of the numerical model and the individual simulations were performed without the aid of this colleague. The interpretation of results were performed together, which provided the basis to plan additional experiments. The solution strategy to overcome the apparent glass matrix distortions was developed without the aid of Tino Elsmann. Possibilities to realize this conceptual idea were discussed and developed together. Individual parts of the presented results are summarized in a manuscript intended for publication.

Fiber Bragg gratings (FBGs) are structural modifications of an optical fiber along its optical axis. In particular, FBGs correspond to periodic modulations of the refractive index distribution along the propagation direction of the supported eigenmode. Then, each modulation inside the waveguide causes a partial reflection of an incoming wave. On the one hand, if the entire number of reflections are interfering constructive, the FBG serves as a high-quality reflector at wavelength λ_{FBG}. This is achieved for optical path length differences, which equal multiples of 2π for a roundtrip of the wave. Hence, the period Λ of the FBGs is given as $\Lambda = \frac{\lambda_{\mathrm{FBG}}}{2n_{\mathrm{eff}}}$, where n_{eff} is the effective mode index. On the other hand, more complex modulations of the cores refractive index distribution even allows to tailor the spectral transmission and reflection properties on demand. For further insights into the theoretical description of FBGs the work of Kersey *et al.* in [102] and Hill *et al.* in [103] is referred, which provides a great overview on the topic. Mostly, FBGs are realized due to the interference of two intense UV-laser beams in the core region of an optical fiber (See Fig. 3.1). The photosensitivity of this core, i.e., due to a germanium dotation, leads to a change of its refractive index caused by the incident UV-laser light. Then, the interference pattern of the initial beam directly inscribes the FBG, where its width Λ is controlled via the incidence angles of the two beams.

FBGs are widely applied within integrated fiber-optical networks, as they offer the potential to realize highly efficient distributed Bragg reflectors in an integrated approach, i.e., a high degree

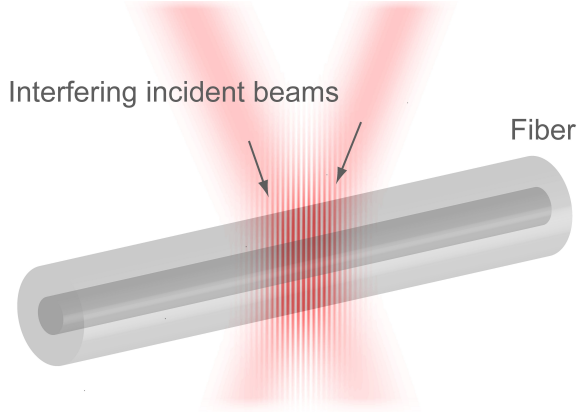

Figure 3.1: Schematic sketch for the realization of fiber Bragg gratings in an optical fiber. Two intense UV-laser beams are interfering in the core region. A photosensitivity of this core leads to a modification of its refractive index depending upon the local intensity of the beam.

of miniaturization without critical adjustments. These devices are widely disseminated in their application and are used, e.g., in temperature and stress sensing [24–26], narrowband filters for data processing [104–106] or most importantly as resonator mirrors for fiber lasers [107, 108]. In the latter case of fiber laser systems the amount of guided light is the most essential parameter. In order to increase this value without exceeding damage thresholds, the mode-field diameter of the guided eigenmode is increased respectively. Thus, the local energy density is lowered, while the overall power is maintained. This is achieved by relying on low-NA fibers, which have a respectively large core area and a low index contrast in between core and cladding. These fibers are realized by a low germanium concentration of the core, which is the responsible parameter for the index contrast. Nevertheless, this parameter also determines the cores photosensitivity. As a consequence, these mentioned low-NA fibers only have a weak photosensitivity. Hence, to realize FBGs in these fibers, the initial laser power for the inscription process needs to be increased. As a consequence, the damage threshold of the cladding material of the fiber can be reached due to the high intensity [109]. Then the fiber material gets modified due to non-linear interaction processes, which negatively affects the properties of these fibers. In particular, after a FBG inscription process a threefold glass matrix distortion at the rear side of the side-illuminated fiber can occur (see Fig. 3.2).

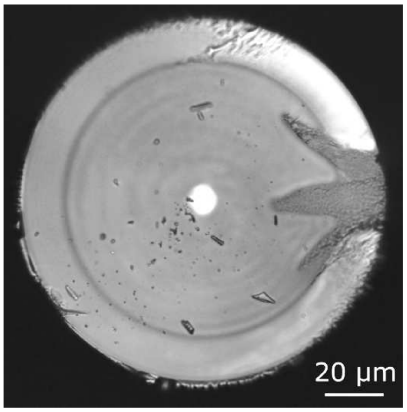

Figure 3.2: Microscopic image of a fiber after the FBG inscription process. Respectively, the incident beam illuminates the fiber from the left side. At the rear side of the fiber a threefold glass matrix distortion is observed. To improve their visibility the contrast of the image was increased.

This distortion, of course, will affect the mechanical stability or even the light propagation inside the fiber. In order to ensure the quality of the realized FBGs and therewith the quality of the respective application, e.g., the fiber laser system, it is of special importance to understand the origin of these mentioned artifacts. The apparent threefold symmetry of the distortion is quite astonishing. Especially the occurrence of the two outer branches is outstanding, as within the symmetry of the experimental setup no indications are found, which could explain their appearance. To discuss this point in more detail, the inscription setup of the FBGs will be elucidated in the following in detail (see Fig. 3.3). To realize the periodically modulated intensity distribution in the core region of the fiber, a two-beam phase-mask interferometer is used. There, an incoming beam is split by a diffraction grating into individual diffraction orders. The 0^{th} order is blocked and the individual 1^{st} and -1^{st} orders are redirected to interfere in the core region. This is realized by two properly oriented mirrors (see Fig. 3.3 (a)). Furthermore, by controlling the angle α of the mirrors, the period of the interference fringes and consequently the ones from the FBG are controlled. Finally, to increase the intensity along the optical axis of the fiber, the initial beam is focused by a cylindrical lens oriented perpendicular to the grating

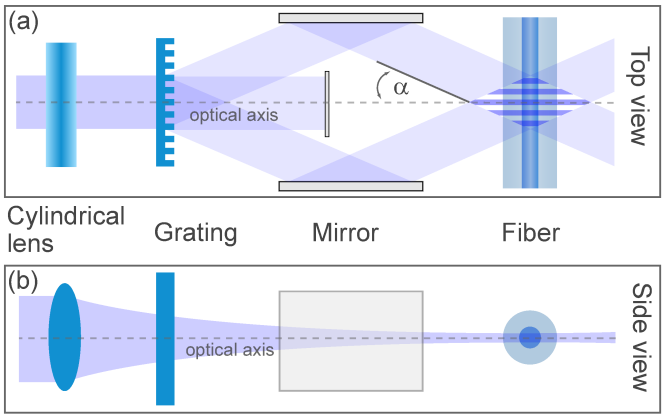

Figure 3.3: Schematic sketch of the experimental setup to realize FBGs. (a) An initial beam is split by a diffraction grating into two beams of equal intensity. These individual beams are brought to interference in the core region of the fiber. (b) To increase the intensity in the core region the initial beam is focused by a cylindrical lens.

(see Fig. 3.3 (b)). This generates an intensity modulated light sheet illuminating the fiber core. At the position of the fiber, this line focus has a waist w_0 of approximately $w_0 = 8\mu m$. As a consequence a FBG is only inscribed at the respective positions within the narrow area of the illuminating beam. To also inscribe FBGs throughout an enlarged area, the beam is scanned throughout the fiber.

By analyzing the proposed setup, only one preferred direction gets evident. This is the optical axis of the setup (see Fig. 3.3). The experimental setup is mirror-symmetric regarding this direction. As a possible explanation for the central lobe one might consider reflected fields from the rear surface of the side-illuminated fiber. Then, the incident and reflected field will interfere and result in a field enhancement. As a consequence, these increased field magnitudes could be viewed as the origin of the central glass distortions. However, these aspects can only serve as a explanation for the central lobe of the distortions. There are no further indications that could explain the appearance of the outer lobes.

3.1 Origin of the glass matrix distortions

To analyze the distortions in more detail, the inscription setup is modeled numerically by relying on the WPM. Due to the symmetry of the setup two dimensional simulations are used, and the respective situation equals Fig. 3.3 (b). Thus, the incidence angle α is neglected within the simulations. Furthermore, as initial field a Gaussian beam with a waist of $w_0 = 8\mu m$ is considered, which is scanned along the cross section of the fiber. Then, individual simulations are considered for different scanning positions of the beam. These respective simulations are considered to be entirely independent from each other. This might be viewed as the simulation of a partially coherent source, where the individual initial beamlets are considered coherently but their superposition is performed incoherently. Finally, to also simulate the reflected field components, the thin-element approximation is evaluated. First, the forward only simulation performed with the WPM is used. Based on these results, the intersection point of the beam with the rear surface of the fiber is calculated as the maximum intensity at these positions. Then, this surface is treated as ideal mirror and the thin-element approximation is evaluated in close vicinity to the intersection point. Due to the small footprint of the incoming beam at the position of the rear surface, only a small part of it is illuminated. Thus, the effective surface sag is very thin at this position, which justifies the local application of the TEA. Finally, the reflected

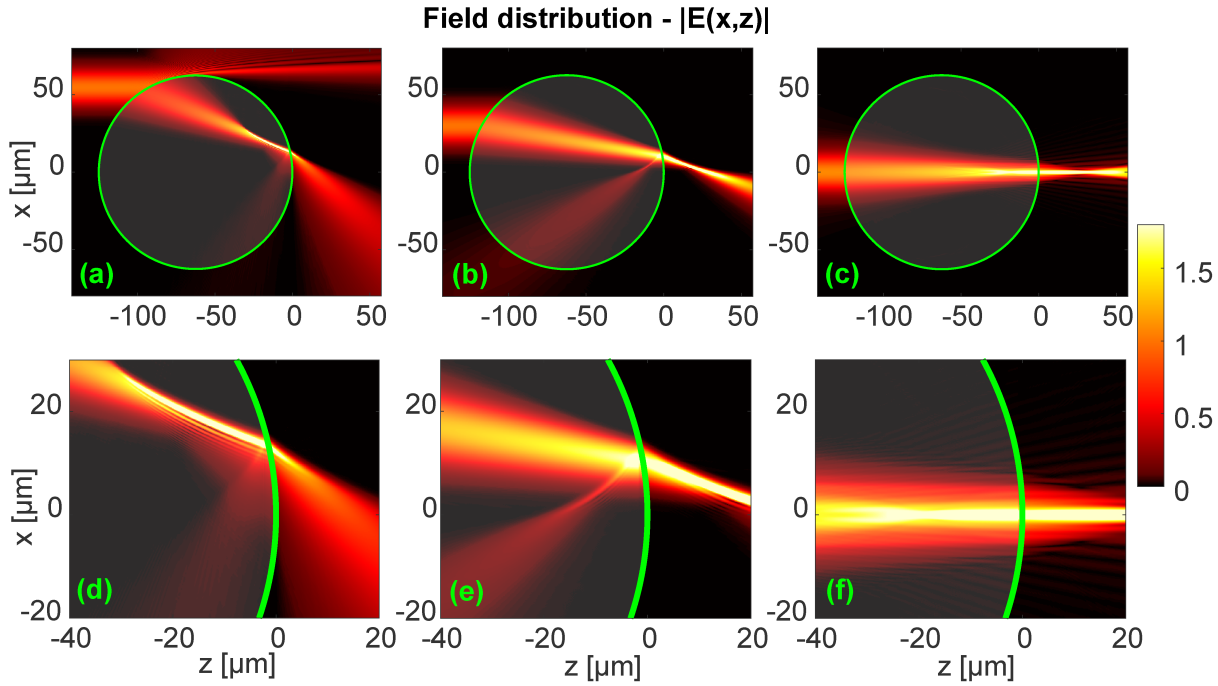

Figure 3.4: Top-row: Field distribution $|E^{x_0}(x,z)| = |E_T^{x_0}(x,z)| + |E_R^{x_0}(x,z)|$ in close vicinity to the optical fiber for a wavelength of $\lambda = 400\text{nm}$. The fiber is made out of fused silica glass with a diameter of $D_{\text{Clad}} = 125\mu\text{m}$ and is side-illuminated by a Gaussian beam with a waist of $w_0 = 8\mu\text{m}$. Moreover, the fiber core has a diameter of $D_{\text{Core}} = 8\mu\text{m}$ and its refractive index is given via the numerical aperture $\text{NA} = .13$ of the fiber $n_{\text{Core}} = \sqrt{\text{NA}^2 + n_{\text{Clad}}^2}$. Within the individual subplots, the initial height of the incoming beam is varied. Bottom-row: Closed up views of the respective simulations of the top-row at the positions of the glass-matrix distortions. All the simulations share the same colormap.

field is propagated backwards and added incoherently to the forward directed one. Thereby, only five percent of the reflected field intensity were taken into account, which approximately fulfills the Fresnel reflection coefficient. Although the chosen model seems like a strong simplification of the problem, it, nevertheless, has the potential to provide a qualitative explanation for the distortions that were found.

In Fig. 3.4 the incoherent superposition of the transmitted $E_T^{x_0}(x,z)$ and reflected field $E_R^{x_0}(x,z)$ is shown for varying initial field heights x_0, i.e., $|E^{x_0}(x,z)| = |E_T^{x_0}(x,z)| + |E_R^{x_0}(x,z)|$. The fiber itself acts like a cylindrical lens and focuses the incoming beams. Nevertheless, the positions where the individual beams reach its smallest waist varies among the configurations. In particular, with increasing height of the initial field this focal position shifts towards the fiber center and even reaches the inner cladding structure. This causes a field enhancement inside the fiber, which might is large enough to exceed the damage threshold of the cladding material. This behavior contrasts the one of a hypothetical ideal lens. In this case, every individual beamlet focuses onto the same position on the optical axis, i.e., the focal point. Thus, the shift of the focal position along the z-direction for the real fiber needs to be interpreted as a form of aberration. To analyze the glass matrix distortions more qualitatively, Fig. 3.5 shows the overall field distribution, i.e., $|E(x,z)| = \sum_{x_0} |E^{x_0}(x,z)|$, overlaid with the microscopic image. The increased field magnitudes fit well to the glass matrix distortions. Thus, these aspects might

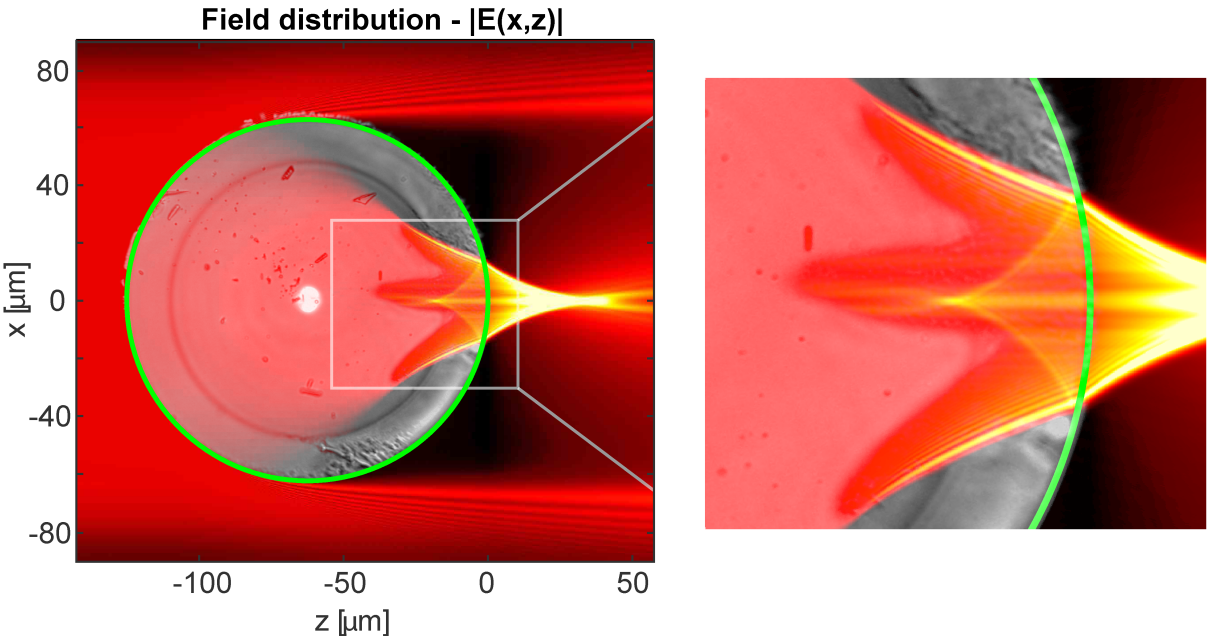

Figure 3.5: Cumulated field distributions $|E(x,z)| = \sum_{x_0} |E^{x_0}(x,z)|$ in close vicinity to the optical fiber for a wavelength of $\lambda = 400$nm. To compare this field distribution qualitatively with the induced glass matrix distortions the corresponding microscopic image is overlaid. At the positions of the compromised glass matrix field enhancements are evident in the simulated field distribution.

serve as explanation for the defects in the fiber. Nevertheless, there are qualitative differences between the field enhancements caused by the reflections in comparison to the ones caused by the off-axis illumination. On the one hand, the focal point in the reflected field appears pronounced as the fields of the individual beams are summing up in this position. Within a single inscription process the field magnitude in the reflected field is lowered (see also Fig. 3.4). This situation differs for the field enhancement connected to the off-axis positions of the initial beam. They are not cumulatively growing and are appearing suddenly for every off-axis beam. This suggests, that the growth of the individual lobes appear different depending upon the conditions to inscribe the gratings. In Sec. 3.2 an example is discussed, where the central lobe is missing. This aspect might be explained due to a lowered initial laser power to inscribe the gratings. Then, the damage threshold might not be exceeded for the central lobe.

In order to develop a solution strategy, not only the origin of the field enhancement of the central lobe needs to be revealed but also the one for the outer lobe. To this end, Fig. 3.6 shows the field distribution of an off-axis beam overlaid with a geometrical raytrace. The individual rays form an aberrated focus inside the cladding, which causes a field enhancement. This non-ideal behavior is explained by the nonlinear properties of the law of refraction. In particular, the off-axis rays hit the cladding surface under grazing incidence and are strongly deflected. This effect is very similar to spherical aberration in classical optical systems. In the considered case these aberrations are strong enough, that neighboring rays even cross each other in the cladding material. Thus, these crossing rays lead to an interference effect, i.e., two-beam interference. As a consequence, an additional field enhancement takes place at the positions of constructive interference, which can be realized in Fig. 3.4 (d). Thus, the outer lobes of the glass matrix

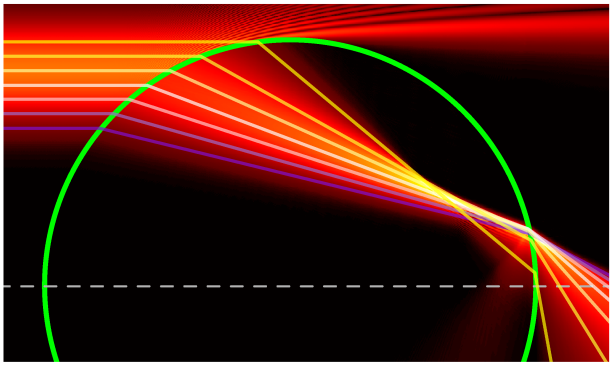

Figure 3.6: Field distribution of an off-axis beam with a distance of $x_0 = 55\mu m$ from the optical axis overlaid with the equivalent geometric optical ray distribution. The wavelength of the beam was chosen as $\lambda = 400nm$. The field enhancement inside the fiber material is caused by an aberrated focal spot for the individual rays.

distortions are explained as spherical aberrations induced by the cylindrical cladding of the fiber. This, of course, suggests that the geometrical footprint of the fiber and therewith the incidence angles on that surface have a strong impact on the appearance of these glass matrix distortions. This aspect is investigated in the following.

3.2 Influential parameters

In the previous section the origin of the threefold glass matrix distortions was investigated. Simulations revealed that spherical aberrations caused by the cladding surface and the reflected field components result in field enhancements. They might serve as explanation of the distortions. Nevertheless, the physical foundation of these effects is caused by non-linear optical processes. Their consideration was omitted in the respective simulations. In turn, including these effects is computationally intense and only possible for respectively small simulation volumes [110]. To verify the original hypothesis, additional experiments are performed to verify the indications on the origin of the glass matrix distortions. To this end, the influence of the cladding geometry will be investigated and the glass matrix distortions after a FBG inscription process in a d-shaped fiber are investigated. These fibers have a polished and flattened part of the cladding in contrast to conventional circular fibers (see Fig. 3.7). These fiber designs are of importance within several fiber laser concepts [111] and are therefore considered here. Within the inscription process the flat side was aligned, as good as possible, parallel to the optical axis of the incident beam. Then, grazing incidence angles are omitted at large initial field heights x_0 at the flat side.

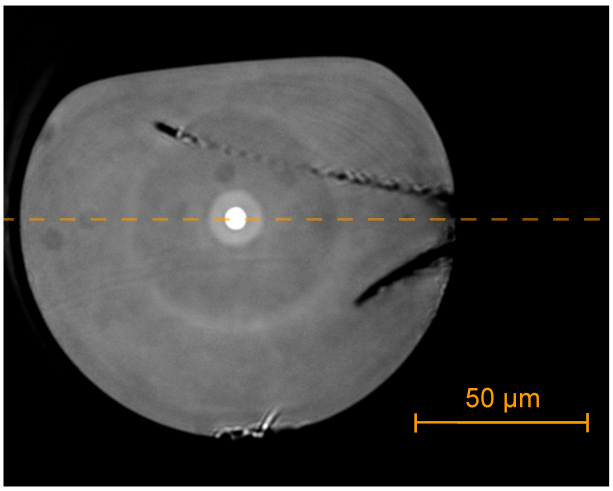

Figure 3.7: Microscopic image of the d-shaped fiber after the FBG inscription process. The incident beam illuminates the fiber from the left side. The angle of the fiber was adjusted qualitatively to account a slight misalignment of the inscribing beam with respect to the fiber. For an angle of 5° the optical axis of the inscribing beam is symmetrical to the distortions. To improve the visibility of the glass matrix distortions the contrast of the image was increased.

As a consequence, the connected outer lobe of the glass matrix distortions was expected not to appear (see also Fig. 3.4). However, this assumption was proven wrong as realized in Fig. 3.7. Moreover, the central lobe of the glass matrix distortion is missing, although the reflections should similarly appear. Nevertheless, as discussed in Sec. 3.1 this might be caused due to a lowered initial laser power.

The pertinent question belongs to the origin of the strong distortion appearing from the polished side of the fiber. This behavior contrasts the intuitive understanding of the situation. To analyze these defects in more detail, Fig. 3.8 (a) shows the simulated field distribution overlayed with the microscopic image. In these simulations, a slight misalignment of the orientation of the flat side of the fiber with respect to the optical axis of the incident beam was considered. This aspect was observed by analyzing the microscopic images. The orientation of the induced glass matrix distortions appeared slightly rotated with respect to the optical axis of the initial beam (see Fig. 3.7).

Within the simulations the outer lobe, which belongs to the flat side of the fiber, is not predicted. Neither the associated field enhancement is found, nor the respective position of the glass distortions matches the simulated field distribution.

Within the simulations an ideal profile of the d-shaped fiber was considered. In particular, a sharp edge in between the circular and the flat part of the fiber was assumed. In turn, within the actual fiber a slight rounding of this edge is evident. Thus, to reveal the origin of the distortions, a slightly changed cladding geometry was considered in a next step. The results are shown in Fig. 3.8 (b). In this modified scenario field enhancements are apparent at the position of the distortions. Thus, the appearance of the strong glass matrix defects are a direct consequence of the adapted geometry. In particular, the rounded edge at the transition between the spherical

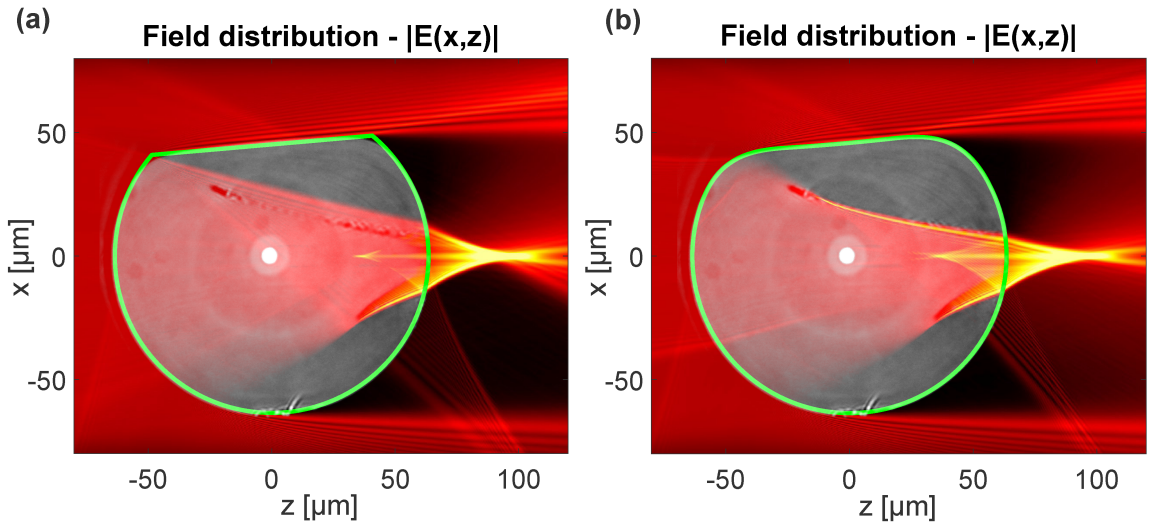

Figure 3.8: Cumulated field distributions $|E(x,z)| = \sum_{x_0} |E^{x_0}(x,z)|$ in close vicinity to the d-shaped fiber for a wavelength of $\lambda = 400$nm. The fiber is made out of fused silica glass with a diameter of $D_{\mathrm{Clad}} = 125$µm and polished from one side. Moreover, the fiber core has a diameter of $D_{\mathrm{Core}} = 8$µm and features a numerical aperture of NA $= 0.13$. (a) Simulation of an ideal d-shaped fiber with a sharp edge at the transition in between the circular and the flat part. (b) Simulation of an d-shaped fiber with a rounded edge. The curvature of this rounding was qualitatively adapted to the microscopic image prior to the simulation.

and the flat part of the fiber acts like an additional lens. This focusing part redistributes the subsequent fraction of the incoming energy. This results in an additional field enhancement at the position of the upper lobe of the glass matrix distortions. It seems astonishing, that this moderate change of the fiber geometry has a major influence on the appearance of the distortions. Nevertheless, this additional experiment confirmed the indications on the origin of these modifications. In a next step a solution strategy will be developed, which avoids the appearance of the distortions.

3.3 Possible solution strategies

In this section a possible solution strategy will be discussed to avoid the appearance of the glass matrix defects. On the one hand, as discussed in the previous section, the cladding geometry has a strong influence on the appearance of these distortions. Consequently, by modifying the cladding footprint, the parasitic field enhancements can be suppressed. As a consequence, the fiber will be non-circular. Then, within the inscription setup, the fiber needs to be oriented properly with respect to the incoming beam. Thus, increased alignment sensitivities appear, which complicate the realization of FBGs. Hence, the concept is not preferable. Alternatively, the actual fiber could be embedded in a material of higher refractive index, i.e., an additional outer cladding structure. Then, the incident beam is refracted at the two distinct materials. By properly designing the additional outer diameter, the field enhancements can be avoided. Moreover, the circular symmetry is preserved and thus the alignment sensitivities remain unchanged. To avoid confusion, the cladding of the actual fiber is referred to inner cladding in the following, to distinguish it from the additional outer one. As an additional benefit, this approach has the potential to overcome a second limitation in the realization of fiber Bragg gratings. By relying on the conventional inscription scheme, FBGs cannot be realized throughout the entire inner cladding area (see Fig. 3.4). There, so-called shadowed regions emerge, which are not illuminated by the incident beams. Hence, in these areas FBGs cannot be realized. The origin of these regions arises from the refraction at the outer cladding surface. The caustic of the refracted rays shadows certain off-axis regions of the fiber (see Fig. 3.5). Nevertheless, to realize FBGs in certain multicore fibers, the illumination of these off-axis regions is mandatory. Thus, an entirely homogeneous illumination throughout the whole fiber is desirable. The novel approach, which in the following is discussed in detail, can overcome these mentioned problems. The design of the outer cladding is carried out in two steps. First, a geometric optical model is established and the outer cladding diameter is optimized. Second, this layout is assessed by wave-optical simulations with the WPM. The final design could be realized in two ways: On the one hand, the composed fiber could be realized within a standard drawing process. Then, a stacked preform composed of the actual fiber and the additional cladding is required. On the other hand, a capillary fiber according to the outer cladding could be realized. Then, it might be possible to insert the actual fiber into this capillary prior to the FBG inscription process. Afterwards this fiber is removed again. This second option has the charm, that the mechanical properties of the overall fiber are not affected at all.

In a first step, a geometric optical model is set up to assess the influence of the outer cladding diameter. In particular, Zemax is used for that purpose. This ray optical approach allows for

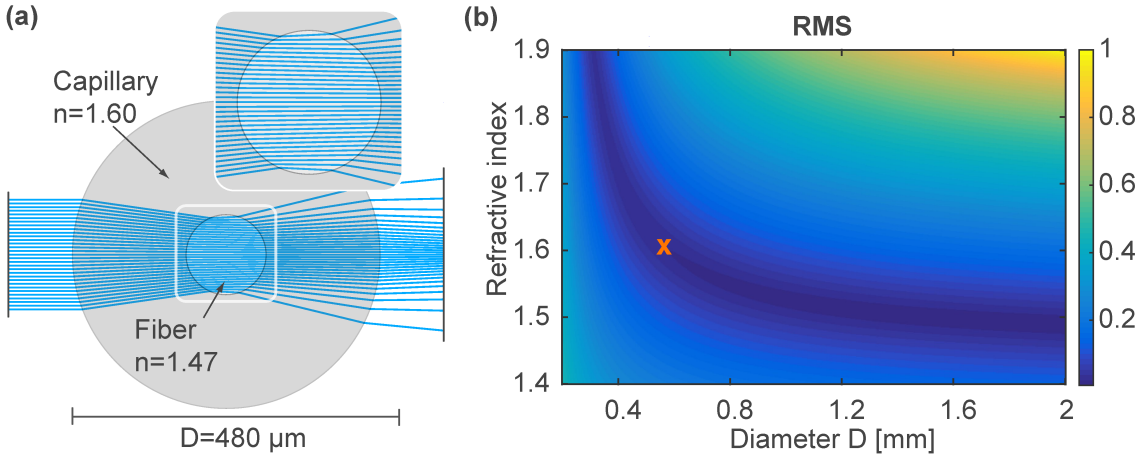

Figure 3.9: (a) Ray distribution inside the stacked fiber for an incoming beam with wavelength $\lambda = 400$nm. The outer cladding diameter was optimized to achieve collimated conditions inside the actual fiber. This ensures a nearly homogeneous illumination throughout the inner cladding. (b) Calculated RMS-value of the angular ray distribution inside the inner cladding for varying diameters and refractive indices of the capillary. The asterix denotes the position of the design according to subfigure (a).

a fast modeling of the scenario and therewith an easy optimization is possible. In a second step, a final design is evaluated by the wave propagation method to assess an as build quality realistically. Within the geometric model, photometric informations are of importance, i.e., the intensity distribution inside the outer cladding and the fiber. These informations are not directly accessible in Zemax. In particular, photometric calculations can only be evaluated in distinct planes, which are not parallel to the incoming rays. However, it is this explicit situation, which is important here. Thus, an alternative evaluation is required, to describe the homogeneity of the illumination. In a geometrical model, the local density of rays describes the intensity of a beam. Thus, to ensure a homogeneous illumination, a constant density is required within the entire inner cladding area. This is achieved, for a collimated beam whose diameter remains constant upon propagation. Hence, within the design the outer cladding diameter is adjusted to achieve collimated conditions within the actual fiber. A respective design is shown in Fig. 3.9 (a). Thereby, reflections were neglected. This is achieved for an anti-reflection coating, which is added onto the outer cladding surface. This avoids the appearance of the central lobe in the glass matrix distortions. In the considered design a refractive index of the capillary of $n = 1.60$ was chosen. As a consequence, the diameter of the capillary yields approximately $D = 480$µm. Moreover, using other glasses or diameters might is required due to constraints of a manufacturing process or an applicability in experiments. To this end, Fig. 3.9 (b) shows the RMS-value of the angular distribution of the rays inside the fiber. This RMS-value is a quantitative measure for the degree of collimation of the rays. Thus, low RMS-values describe a homogeneous illumination. As a consequence, to realize capillaries with a small diameter, a glass with a respectively high refractive index needs to be used.

To further assess the performance of the design, additional simulations with the WPM are considered. There, an anti-reflection coating on the outer cladding diameter is assumed. Hence, no reflected field components are evaluated within the simulations. In Fig. 3.10 the respective

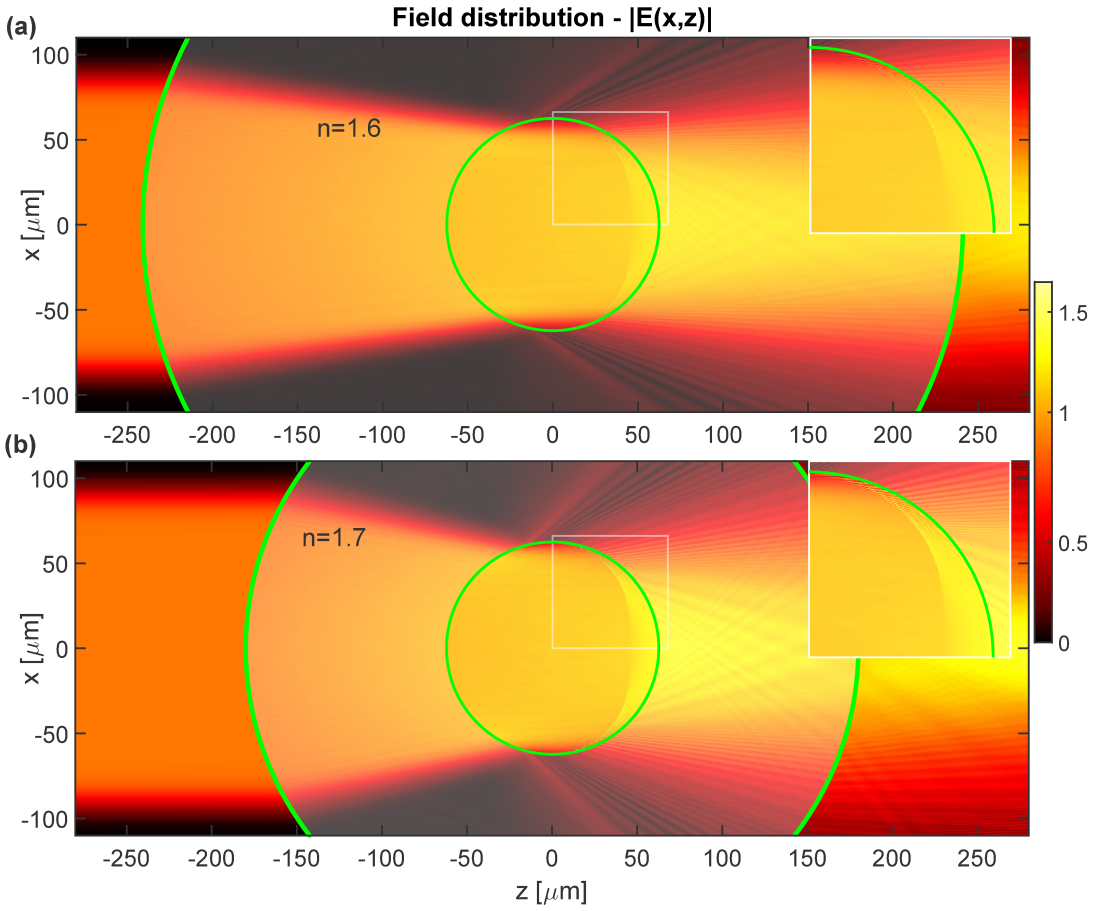

Figure 3.10: Cumulated field distributions in close vicinity to the optical fiber for a wavelength of $\lambda = 400$nm. The individual beams are added incoherently resulting in the final field distribution. Respectively, the simulations for refractive indices $n = 1.6$ and $n = 1.7$ of the outer cladding are compared in subfigures (a), (b). The diameters of the capillary were optimized to achieve nearly collimated conditions inside the fiber.

results are shown for refractive indices of the outer cladding of $n = 1.6$ and $n = 1.7$. In both cases lowered intensities are realized at the top and bottom margin of the actual fiber. Clearly, this issue could be resolved by increasing the initial beam heights x_0. Nevertheless, then also a part of the beam passes the inner cladding. Consequently, these fractions are not refracted and thus are not redirected. As a consequence, this part of the beam interferes with the one that traversed the inner cladding. Hence, this interference leads to parasitic field enhancements inside the outer cladding structure, which should be avoided. However, nearly the entire footprint of the inner cladding is illuminated by the incoming beams and only an outermost part is not illuminated. Referring to the conventional inscription scheme, the proposed setup substantially increases the area in which FBGs can be realized.

Moreover, at the rear side of the actual fiber slight field enhancements can be recognized. They originate from reflections of the incident beam at the rear surface of the inner cladding. These parts interfere with the incoming beam and lead to the slight field enhancement[1]. It gets

[1]The field enhancements originate from the reflected field at the inner cladding surface. Although being a reflected field component the propagation direction of these light components is still in forward direction. In particular, the propagation constant $k_z(k_x, k_y) > 0$ is still positive. Thus, within the WPM these field components are calculated naturally without any extension.

evident that these reflected field components have a stronger influence for the higher refractive index of the outer cladding (see insets of Fig. 3.10). This behavior is caused by the Fresnel reflection coefficients, which increase with a higher index contrast. Thus, to reduce these field enhancements, a lower index of the outer cladding is preferable.

3.4 Summary

In conclusion, this chapter discussed the appearance of glass matrix distortions within the realization of fiber Bragg gratings. In particular, after the inscription of FBGs a reproducible glass matrix distortion is observed at the rear side of the fiber. These modifications show a distinct symmetry characterized by three individual lobes. This aspect is astonishing as no direct evidence is found within the experimental setup, which can directly explain this symmetry. To this end, the inscription setup was modeled numerically by relying on the WPM and these simulations enabled deeper insights about the situation. In particular, spherical aberrations induced by the cladding surface and reflections from the rear surface lead to field enhancements at the positions of the glass matrix distortions. These findings were able to explain the occurrence of these glass defects. To verify these findings, additional experiments were performed. To this end, the glass matrix modifications in a d-shaped fiber were investigated. There, gracing incidence angles for the incoming light were omitted on the flat side of the fiber. Hence, reduced perturbations were expected in this direction. This assumption based on an intuitive understanding of the situation was proven wrong and strong glass modifications were found. In turn, a rounding in between the circular and flat part of the d-shaped fiber originates additional field enhancements, which could explain the strong defects. These increased field magnitudes are absent, assuming the ideal situation without a rounding. These aspects prove, that an intuitive understanding of the situation can fail and only by relying on respective simulations a deeper understanding is gained. Finally, these experiments confirmed the findings on the origin of the glass matrix modifications. Based on these insights a solution strategy was developed. In particular, it is suggested to embed the fiber in an additional cladding structure with an increased refractive index in comparison to the actual fiber. Then, the incoming light is refracted at the two distinct surfaces. By a proper design of the outer cladding diameter the field enhancements are suppressed. As an additional benefit, this approach allows a nearly uniform illumination of the entire inner cladding area. This enables the realization of FBGs within the entire fiber, which is of particular importance for the realization of FBGs in several multi-core fibers. By inspecting this subsequent design with the WPM additional insights were gathered. As a result, a weaker index contrast in between inner and outer cladding is preferable. At the rear side of the inner fiber reflections occur, which lead to a moderate field enhancement. By lowering the index contrast between inner and outer cladding these reflections diminish. Hence, these designs are preferable. However, the respective design has not been realized yet. Thus, a final assessment of its performance is missing and should be viewed as a potential outlook to this work.

4 In-Line Characterization of Optical Fibers

Optical fibers are one of the most important building blocks in modern photonic industries. They provide the unique ability to guide light in a compact design with very small losses. Hence, data can efficiently be transmitted over huge distances and optical fibers evolved to the backbone of telecommunication systems. Moreover, they play a key role in modern integrated laser concepts. To ensure the functionality of these fibers high demands are placed on their fabrication. In telecommunication systems a high purity of the used glass materials is required. Any irregularities will cause parasitic losses of the guided light, which lowers the signal to noise ratio for data transmission. In addition, the actual geometry of these fibers needs to be realized with a highest as-build quality. Similarly, any disturbances will affect the data transmission process. Moreover, for modern integrated laser concepts the mode field diameter is one of the most critical parameters. It influences the overall amount of light, which is guided by the fiber without exceeding the damage threshold of the used glass material. To increase this diameter without affecting the laser beam quality complex, micro-structured fibers are often used [112, 113]. The demands to realize these fibers are steadily increasing and require profound metrological techniques for their characterization. On the one hand, optical- or electron microscopy is used to inspect fibers. However, these techniques require a cleaved and flat fiber tip to assess the inner structural composition. While this enables an accurate assessment of the fiber, it, nevertheless, is a destructive metrological technique. Alternatively, tomographic approaches are used, which enable the reconstruction of the refractive index distribution $n(x, y)$ of the optical fiber by a series of measurements under different illumination conditions [114–119]. The investigated fiber is immersed in an index-matching liquid, which lowers the overall index contrast. This immersion process is required for the evaluation and post-processing of measured data. In this so-called weak scattering regime the application of the Born- and Rytov approximations are justified [120, 121], which form the basis of the tomographic reconstruction algorithm. However, a major down side of these approaches belongs to the immersion of the fiber into an index matching liquid. This cannot be applied within the drawing process and this metrological technique can therefore not be used for an in-line monitoring of fiber parameters.
However, the characterization of optical fibers already during the drawing process is of special significance to ensure their quality and therewith their optical functionality [122]. On the one hand, this allows for the detection of irregularities in realized fibers such as inclusions and impurities in the glasses. On the other hand, it provides the ability to adjust process parameters in a feedback loop to realize fibers with highest as-build qualities. For instance, hollow cores in modern photonic crystal fibers can be adjusted by an applied over pressure during manufacturing. Hence, their constant monitoring can improve the as-build quality of these fibers. However, most of the current techniques for in-line fiber characterization can only monitor the outer cladding diameter [123–127]. Just recently, the evaluation of the inner structural composition emerged into the focus of scientific research [128].

In this chapter, a noninvasive measurement principle is discussed to characterize optical fibers. In particular, an investigated fiber is side illuminated by a monochromatic and coherent beam and the created diffraction pattern is evaluated on a distant screen. A numerical parameter

retrieval enables the assessment of characteristic properties of the investigated fiber. In the following Sec. 4.1 the conceptual idea is introduced and evaluated. To this end, abilities of the approach are systematically assessed and limitations are investigated. In a subsequent Sec. 4.2 these insights are used to improve the methodology. To this end, the experimental setup is refined, which enables an improved assessment of the internal structure of the investigated fiber.

These results were developed in collaboration with Tobias Tiess and Siegmund Schröter from the *Leibniz Institute of Photonic Technology (IPHT)* in Jena. The experiments were planned and designed together. The optical setup was build up by these colleagues and the individual measurements were jointly performed. The entire post-processing and numerical evaluation of measured data was performed without the aid of these colleagues. Individual results were interpreted together, which formed the basis for the planning of additional experimental investigations. In Sec. 4.2 an improved experimental setup is introduced, which allows to characterize optical fibers with an increased accuracy. This refinement is a result of careful analyses of individual simulations to reveal the bottlenecks of the original setup. Additional discussions with these colleagues enabled the development of an experimental setup to overcome limitations of the original one. Several results of this work were published in Optics Express in [75] and Optics Letters in [129].

4.1 In-line holographic measurement setup

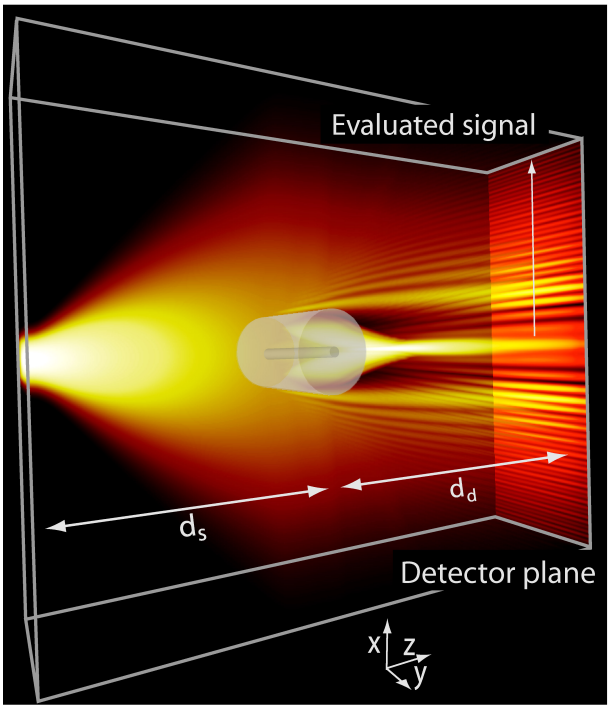

Figure 4.1: Illustrative sketch of the measurement configuration. A coherent and monochromatic incoming beam side illuminates the investigated fiber. This initial beam gets diffracted by the component and causes a characteristic fringe pattern at the position of the detector. Analyzing this interference pattern allows to characterize structural properties of the investigated fiber. The distance between the source and fiber is specified by d_s and the further distance to the detector by d_d.

An in-line holographic measurement principle is considered to characterize structural properties of optical fibers. This methodology is noninvasive and potentially suitable to be integrated into the drawing process of fibers. To this end, a monochromatic and coherent incoming beam side-illuminates the fiber under investigation (see Fig. 4.1). The waist of the initial beam is much larger than the actual diameter of the fiber. Part of the incoming beam is diffracted,

while a remaining part is undisturbed. At the position of a distant screen the individual fractions of the beam are superposed and produce an interference pattern, which establishes the in-line holographic measurement principle. In particular, not only an amplitude information of the diffraction process is encrypted in a measurement but also a phase information due to the interference process. Hence, a characteristic signal for the investigated component is recorded and these in-line holographic approaches are known to allow for measurements with an extraordinary accuracy [130, 131]. However, in the considered case strong index contrasts between air and glass are involved and the conventionally used Born- and Rytov approximations remain no longer valid [120, 121]. In turn, to overcome these limitations extended numerical algorithms are required. Here, a parametric optimization approach is chosen to evaluate measured signals. To this end, the entire setup is simulated numerically using the wave propagation method. Within individual simulations characteristic parameters of the fiber such as the cladding and core diameter are varied. Then, an optimal match between simulated and measured data is examined, which allows to characterize the fiber. Thus, the proposed methodology has the potential to provide a more general framework to evaluate in-line holographic measurements in presence of strong scattering. These abilities are of special significance within modern holographic technologies [20, 27, 28].

4.1.1 Experimental setup

The parameter retrieval of the fiber is founded on a direct comparison between simulations and measurements. This requires an accurate specification and characterization of the used optical components within the experimental setup. Otherwise, systematic deviations might occur within the simulations due to wrong assumptions about the properties of the optical components. Here, an accurate characterization of the illumination source is of critical importance as the initial field distribution $E(x, y, z = z_0)$ is required within the simulations. Any alignment sensitive components should be avoided to warrant a high accuracy and stability of this initial field. To this end, a single mode optical fiber is considered as initial source as its fundamental eigenmode is highly deterministic and stable against environmental disturbances. To this end, the light of a Helium-Neon laser is focused into a single-mode optical fiber at the corresponding wavelength of $\lambda = 0.632\mu$m (Thorlabs SM 630-HP). The fiber filters the incident laser beam and the well specified eigenmode is finally used as initial field within the experiments. To specify the initial field for the simulations an eigenmode solver is used to calculate the supported fundamental mode of the fiber. This mode has an approximate mode field diameter of MFD $\approx 4\mu$m. To establish the in-line holographic measurement principle this initial field needs to be expanded prior to the investigated fiber. To avoid additional optical components to expand the beam, free space propagation diffraction is considered. The optical fiber used for the illumination within the experiments (Thorlabs SM-630HP) features a numerical aperture of approximately NA= 0.13 and similarly defines the divergence angle of the initial field. Hence, by placing the optical fiber at a sufficiently large distance no additional optical components are required. Within the experiments a distance of approximately $d_s \approx 50$ mm was chosen. This ensures a diameter of the beam at the position of the fiber of several millimeters.

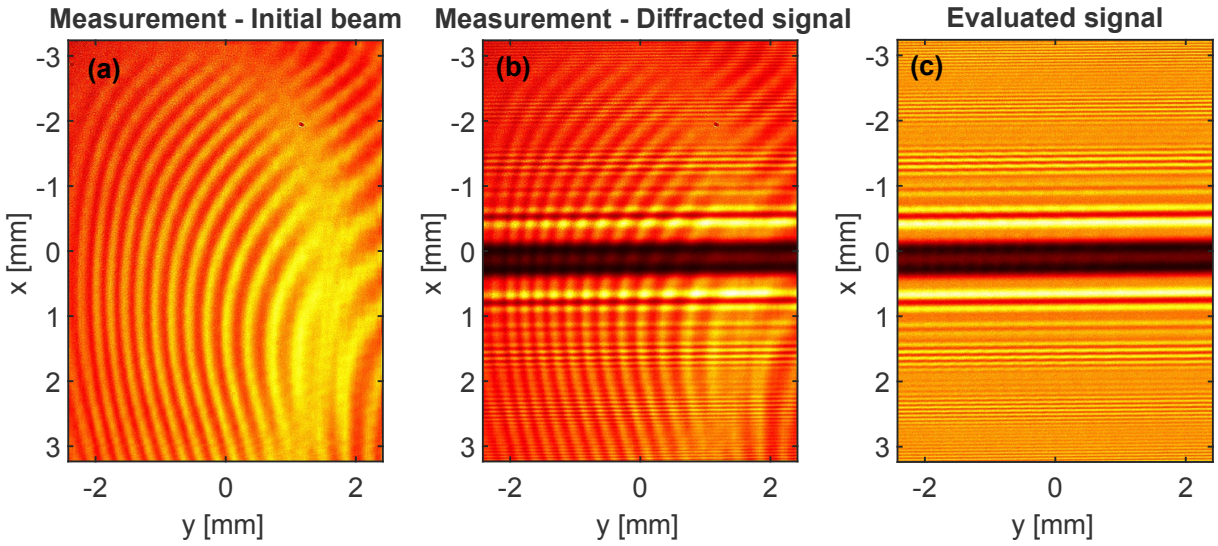

Figure 4.2: (a) Detected intensity $I(x, y)$ of a reference measurement, where the investigated fiber is removed. (b) In-line holographic measurement of the investigated fiber. (c) Apparent interference influences within the measured signals are suppressed by evaluating the ratio between measured diffracted signal and the initial beam, i.e., $\frac{I_{\text{Diffracted}}(x,y)}{I_{\text{Reference}}(x,y)}$.

An additional impact that might disturb a direct comparison between a simulation and a measurement belongs to the influence of the camera. On the one hand, the reliability of measurements is, of course, directly influenced by the imaging properties of the used sensor. On the other hand, the cover glass attached to the sensor for protection purposes can have a critical impact. In particular, this cover glass can induce thin-film interferences and affect the image quality in coherent measurements. This issue is visualized in Fig. 4.2 (a), (b). In Fig, 4.2 (a) a reference measurement is shown, where the investigated fiber was removed in the setup. In this case, one actually expects the image of the expanded initial field emitted by the illuminating fiber, i.e, a nearly gaussian beam. Nevertheless, strong interference artifacts are apparent in the detected signal. These influences are similarly encountered for the actual in-line holographic measurements as shown in Fig. 4.2 (b). These parasitic interference artifacts need to be suppressed in order to evaluate measurements for the parameter retrieval. The appearance of the disturbances could be resolved by removing the cover glass on the sensor of the camera. Alternatively, the artifacts are strongly reduced by evaluating the quotient of the diffracted signal and the unperturbed initial field $\frac{I_{\text{Diffracted}}(x,y)}{I_{\text{Reference}}(x,y)}$ (see Fig. 4.2 (c)). This filtered signal is considered for the further evaluation of measurements and will be shortly interpreted in the following.

Typically, a lowered intensity is measured in the central region of the detected signal. This might be viewed as a shadowing effect of the investigated fiber. In particular, by assuming the fiber being replaced by an equivalent central obscuration a similar image is detected. Then, occurring interference fringes in a measurement are explained by edge diffraction effects originating from the rims of the obscuration. Nevertheless, in the considered case the fiber is transparent and part of the incident beam gets transmitted. In particular, this fraction of the field gets focused

due to the cylindrical lens effect of the side illuminated fiber[1]. This results in a focal spot closely behind the rear surface, which is strongly defocused referring to the distant detector. As a consequence, the connected energy spreads over a larger area. This causes lower intensities in the central region of the recorded detector signal, which is slightly similar to the effect of a central obscuration. Nevertheless, the transmitted field E_{Trans} will interfere with the remained field E_{Remained}, which establishes the in-line holographic measurement principle. Hence, any information about the structural composition of the fiber is encrypted within the entire detector area. A decryption of this signal is very challenging and becomes only possible by relying on numerical simulations.

To improve the comparability between measurements and numerical calculations, the influence of noise in detected signals should be reduced. To this end, the strong symmetry along the $y-$axis in a detected image is considered and a recorded signal is averaged over approximately 100 detector lines. As a downside, this approach slightly reduces contrast in the analyzed interference fringes. To this end, a linear contrast enhancement is performed.
Moreover, the high symmetry about the $y-$dimension justifies to model the entire scenario in a two-dimensional geometry within the simulations, i.e., one transverse $x-$ and one longitudinal $z-$dimension. In a strict sense, this assumption is valid in case the optical setup and the initial field is invariant along the $y-$dimension. However, the Gaussian shape of the incident field perturbs this situation. Nevertheless, this influence is negligible. Otherwise, the diffraction pattern of the fiber would show a curvature in the measured interference fringes, which is not the case in practice. The consideration of a two dimensional geometry can significantly improve the computational runtime to simulate the entire scenario. Nevertheless, the demands for the numerical evaluation are still high as vastly different aspect ratios in the geometry of the setup are involved. While the length of the setup and the beam diameters are macroscopic, smallest feature detail such as the fiber core are microscopic. To cope with these demands the simulation of the entire setup is divided into individual parts. On the one hand, the algorithm as proposed by Shen *et al.* in [132] is used to propagate the optical fields in homogeneous surroundings. In this algorithm parasitic disturbances, caused by the computational boundary, are avoided and an accurate and efficient field propagation is achieved in homogeneous media. Moreover, a stitching approach is considered to reduce the computational effort to calculate the diffraction response of the investigated optical fiber. To this end, the entire incident field E_{Incident} at the position of the fiber is split into two individual subfields $E_{\text{Diffraction}}$ and $E_{\text{Unperturbed}}$, where the sum of these two fields equals the incident field. These fields have a smooth boundary and are therefore partially overlapping. This reduces disturbing numerical artifacts due to the splitting procedure [133]. The subfield $E_{\text{Diffraction}}$ has a transverse elongation of approximately $w = 500\mu\text{m}$, which equals four times the fiber diameter. Then, the diffraction response of the fiber is calculated for this interchanged initial field and the simulations are performed on a smaller computational domain.

[1]This scenario is similar to the one discussed in chapter 3, where the origin of glass matrix distortions during the inscription of fiber Bragg gratings were revealed. However, the initial field conditions differ in the individual scenarios. In particular, for the simulations of the glass matrix distortions the field distribution of a beam with a small waist was considered. This field is scanned along the cross-section of the entire fiber. Then, the cumulated field distributions were evaluated, i.e., individual coherent simulations at different beam positions were added incoherently. This might be viewed as the simulation of a partially coherent source. In contrast to this situation a fully coherent approach is considered here with an overall expanded beam.

For these simulations the wave propagation method is considered. Then, a computational grid density was chosen, which yielded converged results, i.e., a further refinement leads only to marginal changes of a simulated pattern on the detector. These required grid densities were slightly changing for different investigated fibers, e.g., they were depending upon the index contrast between core and cladding. Typically, a grid spacing of $\Delta x \approx \frac{\lambda}{3.5}$ and $\Delta z \approx \frac{\lambda}{15} - \frac{\lambda}{30}$ was sufficient to achieve converged results.

The remaining field $E_{\text{Unperturbed}}$ is not influenced by the investigated fiber and free space propagation codes are chosen. After the calculation of the diffraction response the individual subfields are merged together. Moreover, the setup is simulated monochromatic and a residual bandwidth of the HeNe-Laser is neglected. It is hard to judge the validity of this assumption based on first order principles. However, the overall model performs very well for the simulation of measured signals, which justifies this assumption heuristically. Overall, the calculation of the diffraction response is achieved in a computational runtime of approximately 3-10 seconds, depending upon the diameter of the cladding.

4.1.2 Assessment of a SMF-28 fiber

To assess this conceptual idea to characterize optical fibers, a standard telecom fiber (SMF28) is investigated in a first step. This fiber is characterized by a highest as-build quality and thus ideally suited to evaluate and verify the methodology. According to the vendor, the cladding and core diameter are specified by $D_{\text{Clad}} = 125\,\mu\text{m}$ and $D_{\text{Core}} = 8.2\,\mu\text{m}$ with a nominal uncertainty of $\Delta D_{\text{Clad, Core}} \approx \pm 0.56\%$. The refractive index of the cladding material is characterized

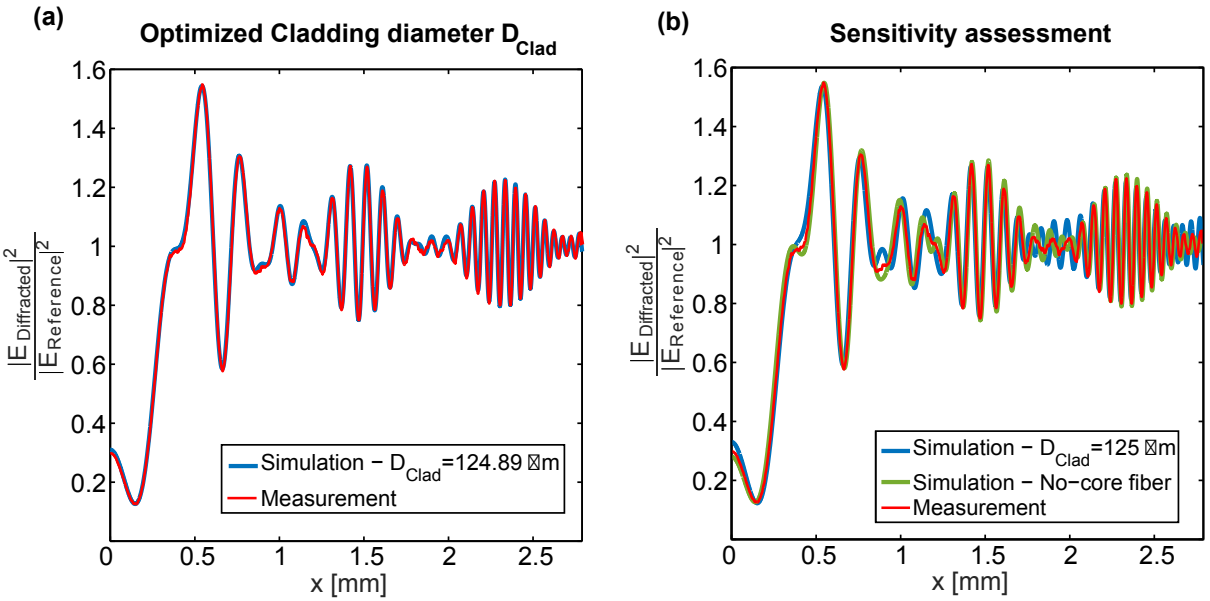

Figure 4.3: Comparison of measured and simulated signals. The origin of the diagram corresponds to the center of symmetry, i.e., the optical axis: (a) Comparison to the optimized cladding diameter $D_{\text{Clad}} = 124.89\,\mu\text{m}$. This belongs to a nominal deviation of $\Delta D_{\text{Clad}} = 0.11\,\mu\text{m}$ in comparison to the nominally specified diameter as proposed by the vendor. (b) Comparison between slightly mismatching parameters and the measurement. The simulation of the nominally specified fiber $D_{\text{Clad}} = 125\,\mu\text{m}$ and an equivalent bare no core fiber with $D_{\text{Clad}} = 124.89\,\mu\text{m}$ are evaluated.

by the one of fused silica $n_{\mathrm{Clad}} = 1.4570$ at the corresponding wavelength $\lambda = 632\mathrm{nm}$. The refractive index of the core is specified via the numerical aperture of the fiber NA= 0.14 as $n_{\mathrm{Core}} = \sqrt{\mathrm{NA}^2 + n_{\mathrm{Clad}}^2} = 1.4637$. Hence, within the optimization process the core and cladding diameter were considered. Additionally the distances $d_s \approx 50 \pm 5\mathrm{mm}$ and $d_d \approx 85 \pm 5\mathrm{mm}$ between fiber and source/detector are not perfectly characterized and are considered within the parameter retrieval. Initial simulations revealed that the uncertainty within the core diameter and the one of the source distance do not significantly influence the outcome of a simulation. The optimization revealed an optimal match between simulation and measurement for a detector distance of $d_s = 84\mathrm{mm}$ and a cladding diameter of $D_{\mathrm{Clad}} = 124.89\mu\mathrm{m}$, which lies well within the specifications of the vendor. This corresponds to a nominal mismatch of $\Delta D_{\mathrm{Clad}} = 0.11\mu\mathrm{m}$, which equals an induced path length difference of approximately $\frac{\lambda}{13}$. The comparison between the measured and simulated signal is shown in Fig. 4.3 (a). To assess the sensitivity of the parameter retrieval, perturbations of the ideally matching parameters are shown in Fig. 4.3 (b). In particular, the nominally specified fiber with a cladding diameter of $D_{\mathrm{Clad}} = 125\mu\mathrm{m}$ is compared with an equivalent no-core fiber with $n_{\mathrm{Core}} = n_{\mathrm{Clad}}$ characterized by the retrieved cladding diameter $D_{\mathrm{Clad}} = 124.89\mu\mathrm{m}$. Clearly, deviations are observed, which indicates the high sensitivity of the measurement principle against varying parameters.

To assess the sensitivity in more detail, the parameter range is extended and also the influence of the refractive index of the core is assessed. To this end, the RMS-error

$$\mathrm{RMS} = \frac{\sqrt{\int \left(\frac{I^{\mathrm{Meas}}_{\mathrm{Diffracted}}}{I^{\mathrm{Meas}}_{\mathrm{Reference}}} - \frac{I^{\mathrm{Sim}}_{\mathrm{Diffracted}}}{I^{\mathrm{Sim}}_{\mathrm{Reference}}} \right)^2 dx}}{\sqrt{\int \left(\frac{I^{\mathrm{Meas}}_{\mathrm{Diffracted}}}{I^{\mathrm{Meas}}_{\mathrm{Reference}}} \right)^2 dx}} \tag{4.1}$$

is analyzed. There $I^{\mathrm{Meas/Sim}}_{\mathrm{Diffracted/Reference}}$ corresponds to the measured/simulated intensity for the diffracted or the unperturbed field. Eqn. 4.1 describes the mismatch between measurements and simulations and is shown in Fig. 4.4. On the one hand, the core and cladding diameter are varied for a fixed refractive index of the core $n_{\mathrm{Core}} = 1.4637$. On the other hand, the core diameter is fixed to $D_{\mathrm{Core}} = 8.2\,\mu\mathrm{m}$ and the cladding diameter and the refractive index of the core are varied. In this scenario, the core refractive index is varied between $n_{\mathrm{Core}} = 1.457$ and $n_{\mathrm{Core}} = 1.5$, which equals the case of a no-core fiber and one with a numerical aperture of NA= 0.36. In every of these cases a minimum is observed at the positions of the nominally specified parameters as proposed by the vendor. Nevertheless, the valley of the merit function is extended and therewith the accuracy to retrieve the core diameter and core refractive index diminishes. To be precise, within the manufacturing accuracy of the cladding diameter $\Delta D_{\mathrm{Clad}} = 0.7\mu\mathrm{m}$ an uncertainty in the core refractive index and diameter of $\Delta n_{\mathrm{Core}} \approx 0.01$, $\Delta D_{\mathrm{Core}} \approx 15\mu\mathrm{m}$ is found. Moreover, it is realized that for the cladding diameter characterization several local minima emerge, which are spaced approximately by $\Delta D_{\mathrm{Clad}} \approx 1.5\mu\mathrm{m}$. Nevertheless, the central minima located around $D_{\mathrm{Clad}} = 125\mu\mathrm{m}$ is slightly deeper. Therewith, the cladding diameter is uniquely retrieved. The occurrence of these local minima is explained by the holographic measurement procedure, which is sensitive to local phase values. This phase information is only unique within the interval of zero to 2π due to phase wrapping for larger phase values. Therefore, phase changes of multiples of 2π

in this diffracted signal can lead to ambiguous results, i.e., the local minima. According to the thin-element approximation this equals a length difference $\Delta z = \frac{\Delta\varphi}{\Delta n k_0} \approx 1.4\mu\text{m}$, evaluated for the refractive indices of air and fused silica glass at the corresponding wavelength $\lambda = 0.632\mu\text{m}$. This value is in close agreement to the experimental separation between individual minima of $\Delta D_{\text{Clad}} \approx 1.5\mu\text{m}$. Nevertheless, by changing the cladding diameter also the amplitude of the diffracted signal changes. These variations are rather unique, which leads to distinguishable RMS-deviations in these local minima.

In summary, it turns out that the wave propagation method is well suited to describe these in-line holographic measurements in presence of strong scattering and enables a parameter retrieval in principle. Nevertheless, at this current stage the accuracies are not sufficient to characterize fibers. The major problem belongs to the fact that individual parameters can be balanced against each other and the parameter retrieval is not unique. This ambiguity might be resolved by adding additional measurements. In particular, measurements could be performed at different rotation angles of the fiber, for different wavelengths and for different image planes, i.e., different distances d_s between fiber and detector. This increases the informational content within the measurements and might lead to unique results. Alternatively, in Sec. 4.2 a modified illumination is proposed, which reduces the influence of the cladding diameter and allows for an improved assessment of the internal structure of fibers.

4.1.3 Assessment of a no-core fiber

To further assess the possibilities of the methodology a slightly elliptical no-core fiber is investigated. A microscopic reference measurement revealed the major and minor axis of the fiber to $a = 201 \pm 1\mu\text{m}$ and $b = 199 \pm 1\mu\text{m}$. In a next step, the fiber was investigated by the in-line holographic measurement principle. In this scenario, particular attention is given to the possibility

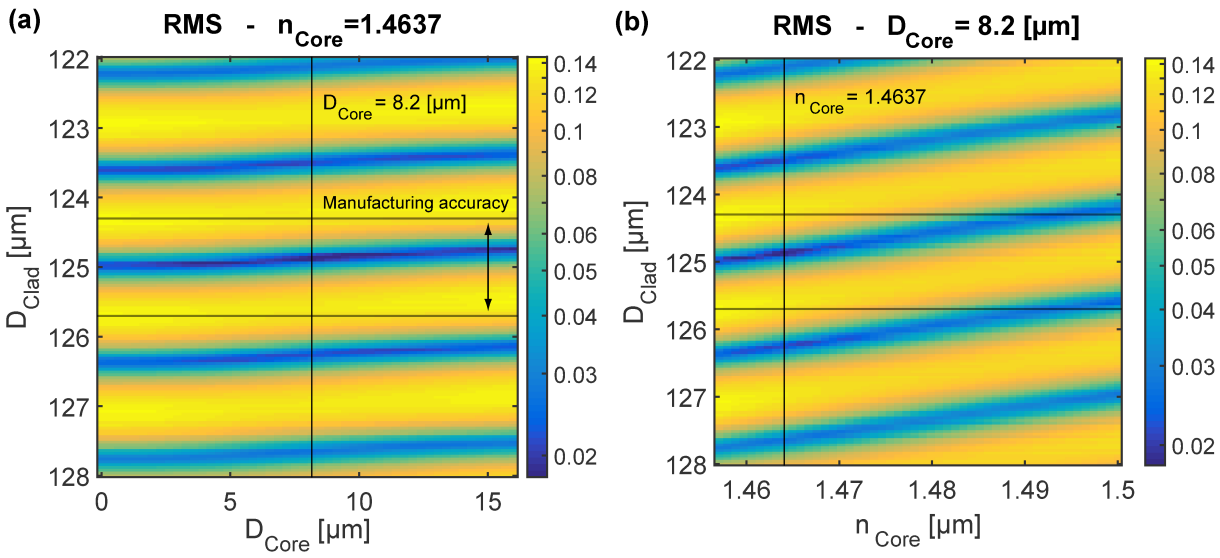

Figure 4.4: Calculation of the relative RMS-error according to Eqn. (4.1) between the measured and simulated signal, where in (a) the refractive index of the core is fixed to $n_{\text{Core}} = 1.4637$ and in (b) the core diameter is fixed to $D_{\text{Core}} = 8.2\mu\text{m}$. These fixed values correspond to the nominally specified parameters as proposed by the vendor.

to not only reveal the individual elliptical diameters but also to retrieve the relative orientation angle of the elliptical fiber. This enables to orient the elliptical fiber parallel along one of the individual axis with respect to the incident beam. This possibility could be of particular interest within the inscription process of fiber Bragg gratings. In this scenario the explicit geometry of a fiber and its orientation can have a strong impact on the appearance of glass matrix distortions (see Sec. 3.2 for reference).

Referring to the previous measurements, the experimental setup was slightly changed. In particular, the investigated fiber was mounted on a rotation unit, which allows to change the angle of the elliptical fiber with respect to the incoming beam. Then, a series of measurements under varying angular rotation angles in steps of $\Delta\vartheta = 10°$ were performed and the measured results were evaluated. The ellipticity of the fiber breaks the symmetry of the experimental situation with respect to the $x-$axis. In particular, only by orienting either of the elliptical axis of the fiber parallel to the incoming beam, the overall symmetry is maintained. In these cases a

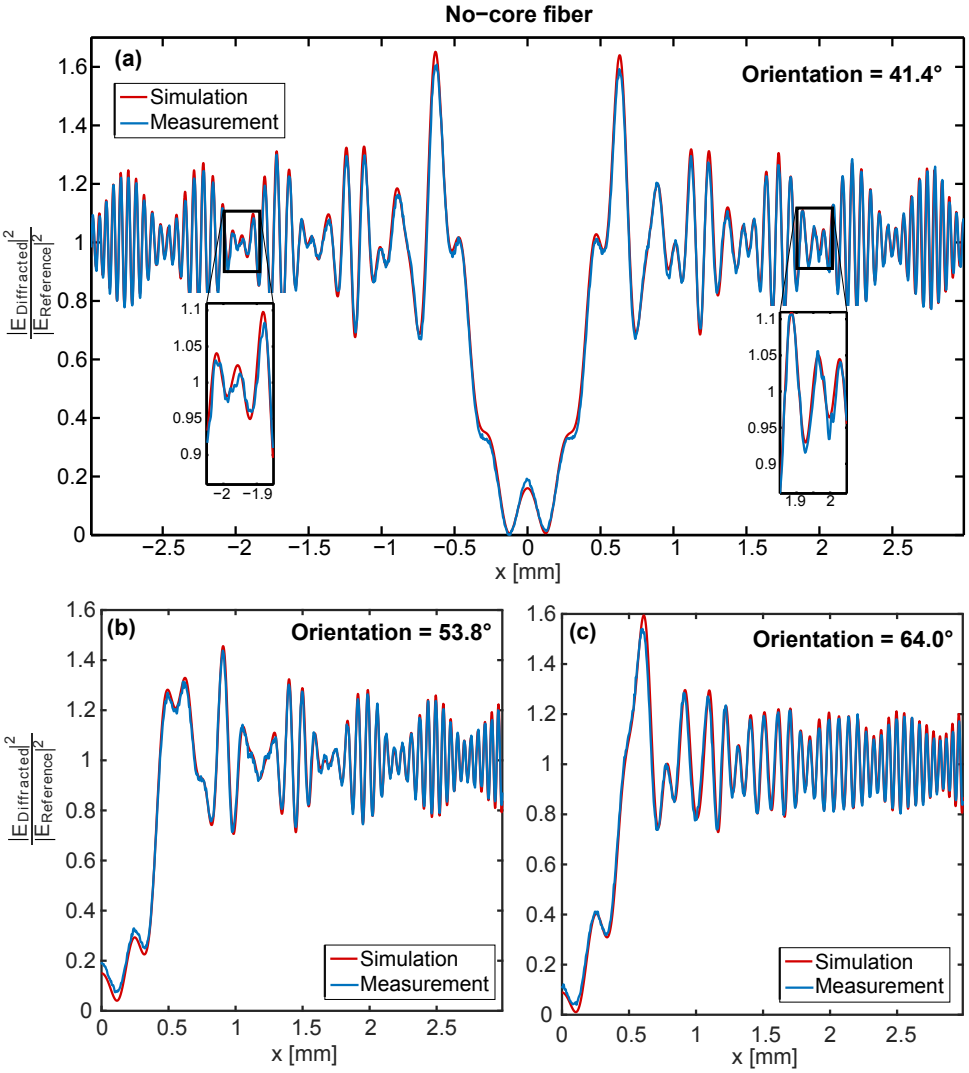

Figure 4.5: Comparison of measured and simulated signals for the assessment of a elliptical no core fiber under different relative orientation angles. The retrieved orientation angle of the elliptical fiber equals $\vartheta = 41.4°, 53.8°, 64.0°$ in subfigures (a)-(c) respectively. The optimization revealed the major- and minor axis as $a = 201.76\mu m$ and $b = 199.13\mu m$.

detected signal should be axis-symmetric, i.e., $f(x) \stackrel{!}{=} f(-x)$. Any changes of these exceptional orientations perturb the symmetry and should be directly seen within a measured signal as an asymmetry. This aspect could be used to align the individual fiber axis parallel to the incoming beam. In particular, a positioning of the fiber might become possible by readjusting the orientation angle and by maximizing the symmetry about the $x-$axis within a detected signal.
However, in practice this alignment procedure turned out to be difficult. By rotating the fiber distinguishable changes in the detected signals are realized, as shown in Figs. 4.5 (a)-(c). However, the asymmetry in a detected signal is quite weak as realized in Fig. 4.5 (a). To highlight the broken symmetry two insets are added into this graph. This issue might be explained by the limited numerical aperture NA within the detection process, which is given by the sensor width $L_x \approx 6\text{mm}$ and the detector distance $d_d \approx 84\text{mm}$ as $\text{NA} = \frac{\frac{L_x}{2}}{d_d} \approx 0.04$. Thus, the measurement process might only be sensitive to an effective diameter of the ellipse along the optical axis. Hence, additional information about the orientation of the ellipse within a single measurement might be resolved by an increased numerical aperture in the detection process.
Alternatively, the elliptical parameters of the ellipse are retrieved by evaluating the whole set of measurements simultaneously. The aspect of an effective elliptical diameter is used for the optimization in a first step. To this end, the ellipticity of the investigated fiber is neglected and within the optimization an effective diameter is retrieved for every individual measurement. The largest and the smallest retrieved values were considered as initial major- and minor axis. In a next step, the orientation angle is considered additionally and all parameters were optimized simultaneously. This analysis allowed the retrieval of the current orientation angle and the assessment of the major- and minor-axis to $a = 201.76\mu\text{m}$ and $b = 199.13\mu\text{m}$. These results are shown in Fig. 4.5 (a)-(c). As a sanity check, the retrieved orientation angles within the optimization are in agreement with the adjusted angles within the experiments. There are only slight mismatches, e.g., the angular separations are slightly different $\Delta\vartheta \neq 10°$. This issue is explained by the experimental adjustability of the fiber rotator and an error is estimated of at least $\pm 2°$.

4.1.4 Assessment of a capillary fiber

In the following, the assessment of capillary fibers will be discussed, which, in contrast to conventional fibers, are characterized by a hollow core. Capillaries with small hole diameters between several hundred nanometers and a few micrometers are important for several modern technologies. The scope of applications includes medical diagnostics [134], plasmonic sensing [135–137], and novel dye laser concepts [138, 139]. In every of these applications, the diameter of the capillary hole has a crucial impact on the overall functionality. Hence, the diameter has to be controlled very accurately during manufacturing. The diameter of this capillary hole can be adjusted during the drawing process by controlling an overpressure in the hollow core [140]. The ability to monitor this core diameter on-line is of special importance. It can enable a feedback mechanism to accurately control the resulting diameter of the hollow air core. This can significantly enhance the quality of realized capillary fibers and therewith improve their functionality in a respective application.

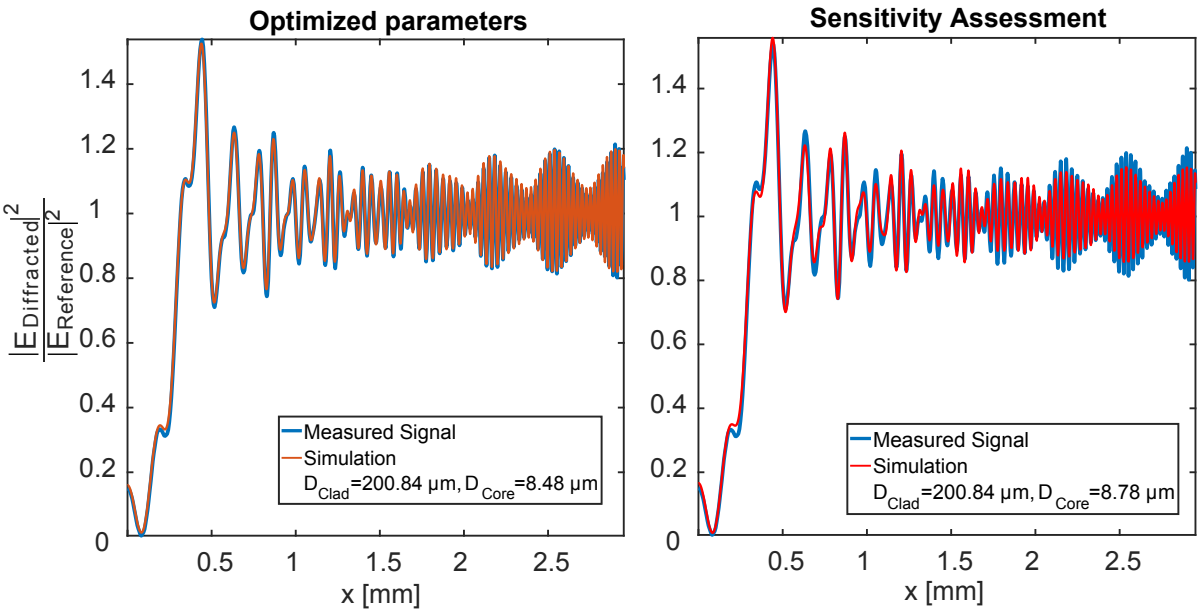

Figure 4.6: Comparison of measured and simulated signals. The origin of the diagram corresponds to the center of symmetry, i.e., the optical axis: (a) Comparison of the measured signal in comparison to the optimized cladding and capillary hole diameter $D_{\text{Clad}} = 200.84\mu\text{m}$, $D_{\text{Cap}} = 8.48\mu\text{m}$. (b) Comparison of the measured signal to a slight deviation of the ideally matching parameters. In particular a mismatch of the capillary hole diameter of $\Delta D_{\text{Cap}} = 0.3\mu\text{m}$ is introduced.

Within the experimental assessment, a capillary fiber with an approximate cladding diameter of $D_{\text{Clad}} \approx 200\mu\text{m}$ and a capillary hole diameter of $D_{\text{Cap}} \approx 8\mu\text{m}$ was chosen. For these measurements the source and detector distance equaled $d_s \approx 70\text{mm}$ and $d_d \approx 60\text{mm}$. Thus, the detector was moved closer to the diffracting fiber, which increases the numerical aperture within the detection process. While a further reduction would be beneficial, experimental constraints such as the housing of the camera prohibited to choose a shorter detector distance. For these measurements the parameter retrieval revealed a cladding and capillary hole diameter of $D_{\text{Clad}} = 200.84\mu\text{m}$, $D_{\text{Cap}} = 8.48\mu\text{m}$. These respective results are shown in Fig. 4.6 (a) and a comparison between the measured signal and a slightly mismatching capillary hole diameter of $\Delta D_{\text{Cap}} = 0.3\mu\text{m}$ is shown in Fig. 4.6 (b). Clearly, the small change in the capillary hole diameter is distinguished, which suggests the high sensitivity to assess the capillary hole. Additional simulations revealed that the mutual influence between the capillary hole diameter and the cladding diameter within the parameter retrieval is weak. Therewith, the retrieved capillary diameter can be revealed with an accuracy $\Delta D_{\text{Cap}} < 0.3\mu\text{m}$. This finding is in contrast to the investigation of the SMF28 fiber, where a strong correlation between core and cladding diameters reduced the accuracy to retrieve the core diameter. The improved sensitivity to characterize the capillary fiber is explained by the strong scattering response of the capillary hole. While a conventional fiber core is characterized by an index difference of $\Delta n < 10^{-2}$ the index difference between the cladding and the hollow core is as large as $\Delta n \approx 0.457$. As a consequence, the capillary hole induces a strong scattering response, which allows to retrieve this parameter with an improved accuracy.

Nevertheless, a detected interference pattern is characterized by high frequent modulations. This sets high demands for the measurement process. Any environmental disturbances such as vibrations can influence the detected interference patterns. Hence, reducing the spatial frequencies within the detection process is desirable. As it will be shown in the following Sec. 4.2, these modulations are connected solely to the assessment of the outer cladding diameter and any additional analysis and interpretation of these high frequent modulations is omitted here[2]. Moreover, to retrieve the capillary diameter, weak amplitude modulations have to be evaluated. Hence, to further increase the accuracy and applicability of the methodology an improved distinguishability of detected signals depending upon structural changes of the fibers is desirable. These aspects are discussed detailed in the following section.

4.2 Improved assessment of the internal structure of optical fibers

In the following, the proposed in-line holographic measurement setup is refined to improve the assessment of optical fibers. This setup will especially be optimized to retrieve the inner structural composition of the fiber. Thereby, the sensitivity to assess the outer cladding diameter will be strongly reduced. While this aspect seems to be adverse at first glance it actually constitutes a strong advantage of the setup. On the one hand, the outer fiber diameter is typically monitored already during fabrication, e.g., by the method as introduced by Watkins [123]. On the other hand, within the parameter retrieval there is a mutual influence between the cladding diameter and other structural fiber parameters. In particular, for fibers with weak index contrasts this results in an ambiguity between the retrieved core- and cladding diameter and these parameters could be balanced against each other within the optimization process (See Sec. 4.1.2 for reference). Hence, a reduced impact of the outer fiber diameter within the evaluation of measurements seems preferable for the overall characterization of the internal structural composition of the fiber. To reduce the influence of this outer cladding diameter within the evaluation of measurements, the diameter of the incoming beam is strongly reduced. A schematic sketch of the measurement setup is depicted in Fig. 4.7. In particular, the waist of the incident beam is chosen smaller than the outer cladding diameter of the investigated fiber. Hence, there is only a transmitted field E_{Trans} that traverses the investigated fiber and there is no remained field E_{Remained} any longer. As a consequence, the in-line holographic measurement principle breaks apart for the assessment of the outer cladding diameter. This originates the decreased sensitivity within the optimization process towards this parameter. Additionally, high frequent modulations in a detected signal are avoided. These oscillations were caused in the original setup by the interference in between the transmitted and the remained field. Hence, the

[2] Alternatively, a Fourier-based assessment of detected patterns might reveal deeper insights about the diffraction process and allows to resolve the high frequent modulations in Fourier-space. In addition, phase-resolved measurements will improve the assessment of investigated fibers. These phase-informations might be gathered by evaluating diffraction patterns in several measurement planes. Then, phase retrieval algorithms might be used to achieve the required informations [53]. Nevertheless, the experimental requirements are high as any environmental disturbances will have a critical impact. As a consequence, any additional effort to analyze measured interference patterns is omitted.

refined setup reduces strong oscillations within measured diffraction patterns and the numerical post-processing simplifies.

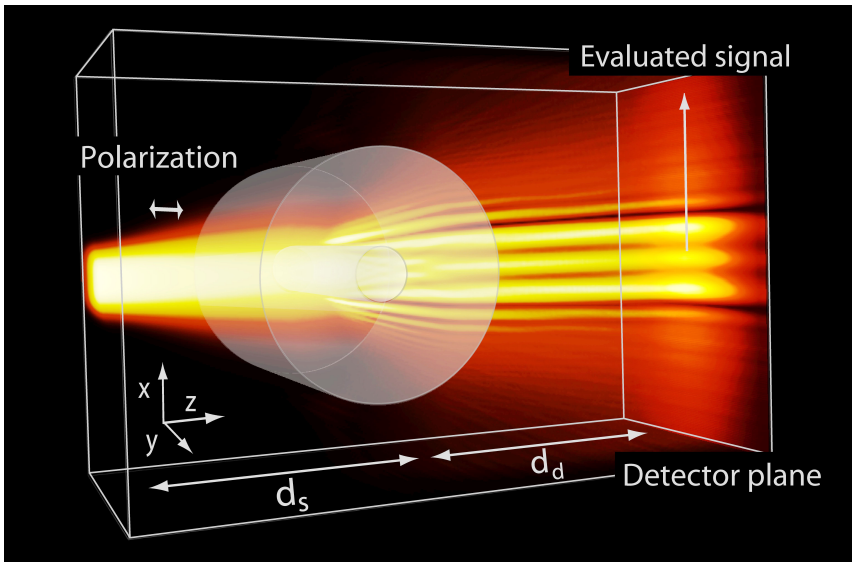

Figure 4.7: Illustrative sketch of the measurement configuration. An incoming beam with a waist size smaller than the cladding diameter but larger than the core diameter gets diffracted. This establishes an in-line holographic measurement principle between the diffracted and the remained field inside the optical fiber. This leads to a characteristic fringe pattern at the position of a distant detector specific to the internal structure of the investigated fiber. The distance between the source and fiber is specified by $d_s \approx 300\mu$m and the further distance to the detector by $d_d \approx 50$ mm (Note, the sketch is not to scale). Detected signals are evaluated along the x-axis, i.e., perpendicular to the principal axis of symmetry (y-axis).

As an advantage, the in-line holographic measurement principle remains valid for the assessment of the internal structural composition of the investigated fiber. In particular, the initial beam waist is chosen smaller than the assessed fiber diameter but still larger than the internal structures such as the fiber core. Thus, the in-line holographic measurement principle is founded entirely on the transmitted field that traverses the fiber, i.e., in between the diffracted signal by a fiber core and the respective remained field.
Moreover, in this modified setup the signature of the internal structural composition should strongly improve in a measured signal. In particular, the smaller waist of the initial beam increases the amount of diffracted power, e.g., by the fiber core. To be more precise, in this case the ratio between the incident beam diameter and the internal feature sizes is improved, which increases the signal to background ratio.

To establish the conceptual idea of the improved in-line holographic measurement setup, the initial beam diameter should be lowered. This is realized experimentally by placing the illumination fiber at a distance of approximately $d_s \approx 200 - 300\mu$m in front of the center of the investigated fiber. This distance ensures that the diverging initial field is much smaller than the cladding diameter at the position of the investigated fiber, but still larger than internal structural feature sizes. This chosen approach is not suitable for an integration into the drawing line of optical fibers. In particular, this setup is too fragile to be integrated into the drawing process of optical fibers. By designing a proper illumination unit, these challenges could be resolved.

However, the current realization allows to assess the methodology in a proof-of-principle study without demanding additional efforts.
Within the measurements the distance between the source and the fiber could not be controlled with a required accuracy and is considered additionally within the numerical parameter retrieval. Moreover, a polarization remaining fiber was chosen for illumination. The polarization of the initial field is chosen parallel to the optical axis of the investigated fiber by properly aligning the polarization axis (see Fig. 4.7). Then, the overall situation equals TE-polarization, where the electric field vector is parallel along the symmetry direction of the entire scenario. As a consequence, a Helmholtz equation for the electric field component E_y describes the experimental configuration rigorously (see Eqn. 1.5 in Sec. 1.1.1 for reference). This aspect improves the applicability of the wave propagation method for the simulations, since the algorithm intends to solve the Helmholtz equation instead of the full set of Maxwell's equations.

To assess the modified experimental scenario in more detail, Fig. 4.8 (a) shows the near

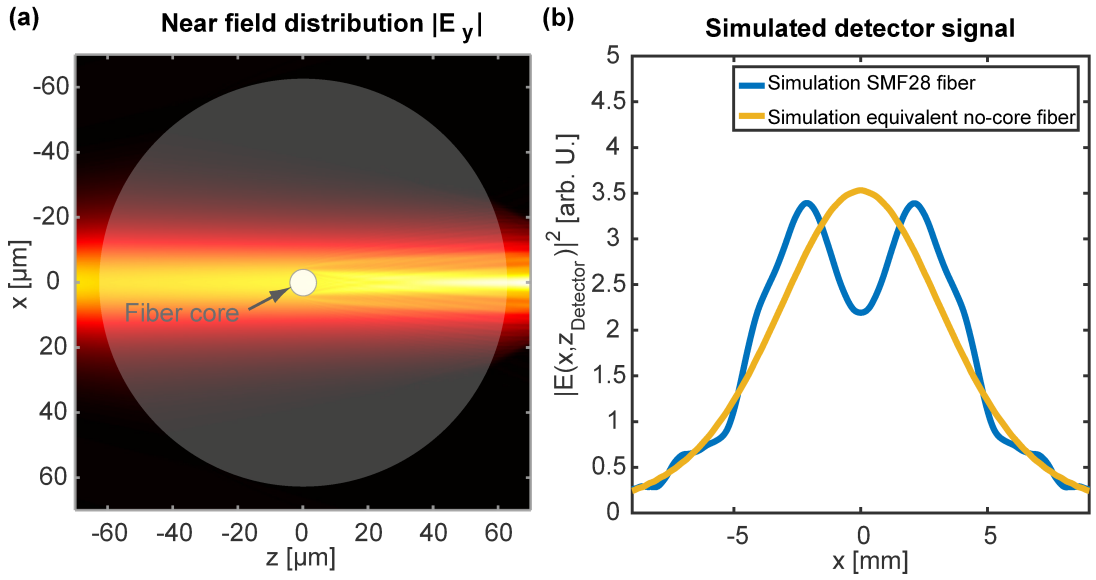

Figure 4.8: (a) Simulation of the field distribution in close vicinity to the optical fiber for the improved in-line holographic measurement setup. As incident field the eigenmode of a single mode optical fiber at a wavelength of $\lambda = 0.633$ µm is considered, which is placed at a distance of $d_s = 200$µm in front of the investigated fiber. The cladding and core diameter are specified as $D_{\mathrm{Clad}} = 125\,\mu\mathrm{m}$ and $D_{\mathrm{Core}} = 8.2\,\mu\mathrm{m}$. The refractive index of the cladding material is specified by the one of fused silica at the corresponding wavelength $n_{\mathrm{Clad}} = 1.4570$. The refractive index of the core is specified by the numerical aperture of the fiber NA $= 0.14$ as $n_{\mathrm{Core}} = \sqrt{\mathrm{NA}^2 + n_{\mathrm{Clad}}^2} = 1.4637$. (b) Simulated signal at the position of a detector at a distance of $d_d \approx 45$mm behind the diffracting optical fiber.

field around a hypothetical SMF28 fiber. This standard telecom fiber is characterized by a weak index contrast of $\Delta n \approx 7 \cdot 10^{-3}$ between core and cladding and its characterization was difficult relying on the original in-line holographic setup (see Sec. 4.1.2). The diameter of the incident beam is chosen slightly larger than the optical fiber core. This increases the amount of diffracted energy without affecting the in-line holographic measurement principle and, therewith, this improves the signature of the core in a detected signal. This aspect is shown in Fig. 4.8 (b).

There, a simulated detector signal of the SMF28 fiber is shown in comparison to the equivalent no-core fiber. Clearly, these signals show an improved distinguishability in comparison to the original setup and high frequency oscillations are suppressed significantly (see Sec. 4.1.2 for reference). The simulated signal of the SMF28 fiber is characterized by a dip in the center of the measured signal. For the equivalent no core fiber the dip is absent and the overall signal has a nearly Gaussian shape. This shape is not significantly affected upon a change of the cladding diameter. In particular, the fiber might be viewed as a cylindrical lens and the cladding diameter determines its effective focal length. A slight change of the radius influences the focal power. As a consequence, this leads to a slight change of the beam diameter on the detector. Nevertheless, the overall Gaussian shape remains preserved. Any significant change of this measured field profile is caused by an internal structural change, e.g., a fiber core or impurities in the glass material. Hence, the ambiguity in the parameter retrieval between a cladding and core diameter is removed (see Sec. 4.1.2 for reference). Hence, this modified setup can uniquely resolve optical path length differences of at least $\frac{\lambda}{12}$, which are approximately induced by the optical fiber core ($D_{\mathrm{Core}} = 8.2\,\mu\mathrm{m}$, $\Delta n \approx 7 \cdot 10^{-3}$).

4.2.1 Assessment of capillary fibers

As a representative scenario to discuss the improved fiber characterization methodology, the assessment of capillary fibers is considered in the following. For these measurements a new camera (Allied Vision - GT3300) with a removed cover glass was used. Then, parasitic interference artifacts that originate from thin-film interferences on the cover glass are removed. As an advantage, no reference measurements are required any longer. To evaluate the measurements, an averaging of about 500 detector lines (2.5mm) along the axis of translational symmetry ($y-$axis), and a linear contrast adjustment were performed to reduce spurious influences of noise and stray light.

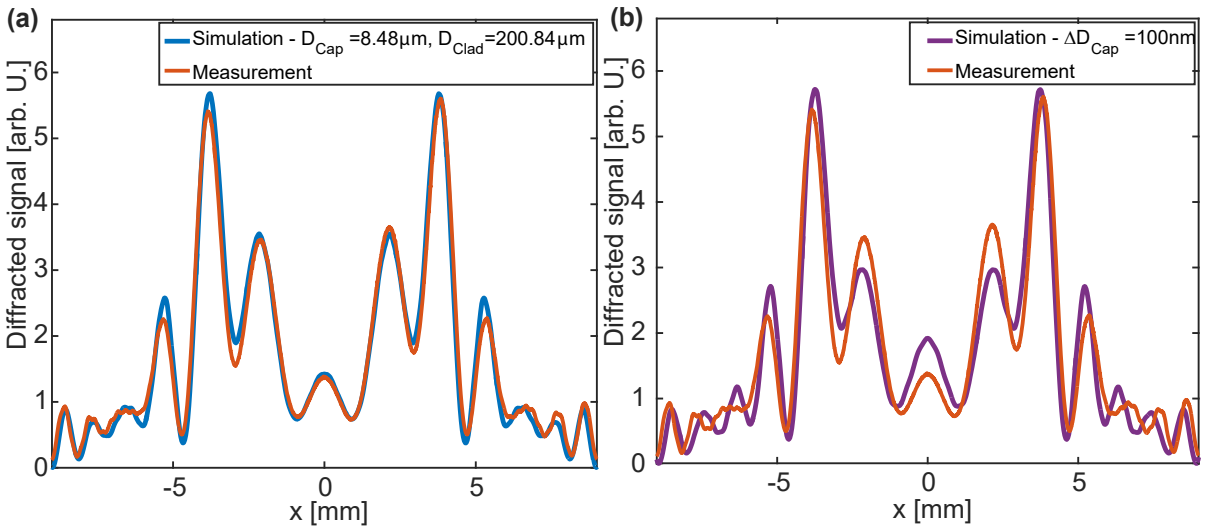

Figure 4.9: Comparison of measured and simulated signals. The investigated fiber is characterized by the vendor with an approximate capillary hole diameter of $D_{\mathrm{Cap}} \approx 8\mu\mathrm{m}$. The origin of the diagram corresponds to the center of symmetry ($y = 0$), i.e., the optical axis: a) Comparison to the capillary hole diameter of $D_{\mathrm{Cap}} = 8.48\,\mu\mathrm{m}$ and a cladding diameter of $D_{\mathrm{Clad}} = 200.84\,\mu\mathrm{m}$. (b) Comparison to a slightly mismatching capillary hole diameter of $D_{\mathrm{Cap}} = 8.58\mu\mathrm{m}$

In a first step, the capillary fiber used for the evaluations in Sec. 4.1.4 is reconsidered. This allows to perform a sanity check for the previously retrieved parameters. Hence, current measurement results are evaluated without considering the cladding and capillary hole diameter. Within the parameter retrieval only the distances d_s and d_d are optimized. The respective comparison between simulation and measurement is shown in Fig. 4.9 (a) for a retrieved source and detector distance of $d_s \approx 265\mu m$ and $d_d \approx 55mm$. A good agreement between simulation and measurement is found for the previously retrieved parameters. This underlines the internal consistency of the in-line holographic measurements to characterize optical fibers. Moreover, Fig. 4.9 (b) shows the simulated signal for an increased hole diameter of $D_{\mathrm{Cap}} = 8.58\ \mu m$. This slightly deviating diameter of only $\Delta D_{\mathrm{Cap}} = 100$ nm leads to distinguishable results within the parameter retrieval. This verifies the improved accuracy of the modified in-line holographic measurement setup.

In the following, the accuracy in the parameter retrieval is discussed in more detail and special emphasis is placed on the occurrence of local minima in the optimization. To this end, an alternate capillary fiber is investigated, which is characterized by the vendor with an approximate cladding and hole diameter of $D_{\mathrm{Clad}} \approx 200\mu m$ and $D_{\mathrm{Cap}} = 4 - 5\mu m$. Fig. 4.10 shows the comparison between the measured signal and the simulation based on the retrieved parameters. In particular, for a capillary hole diameter of $D_{\mathrm{Cap}} = 4.55\,\mu m$ an optimal match is found. The topology of the merit function is analyzed to assess the uniqueness of this retrieved parameter. To this end the RMS-deviation between simulation and measurement is evaluated

$$\mathrm{RMS} = \frac{\sqrt{\int \left(|E_{\mathrm{Meas}}(x)|^2 - |E_{\mathrm{Sim}}(x)|^2\right)^2 \, dx}}{\sqrt{\int \left(|E_{\mathrm{Meas}}(x)|^2\right)^2 \, dx}} \,, \tag{4.2}$$

for varying parameter configurations. In Fig. 4.11 (a) the RMS-deviation for varying cladding and capillary hole diameters is shown, while the initial source distance of $d_s = 340\mu m$ is fixed. In Fig. 4.11 (b) the initial source distances and the capillary hole diameters are varied, while the cladding diameter $D_{\mathrm{Clad}} = 200\mu m$ is fixed. A relatively weak sensitivity is found towards the cladding diameter D_{Clad} and the source distance d_s. In particular, the uncertainty in

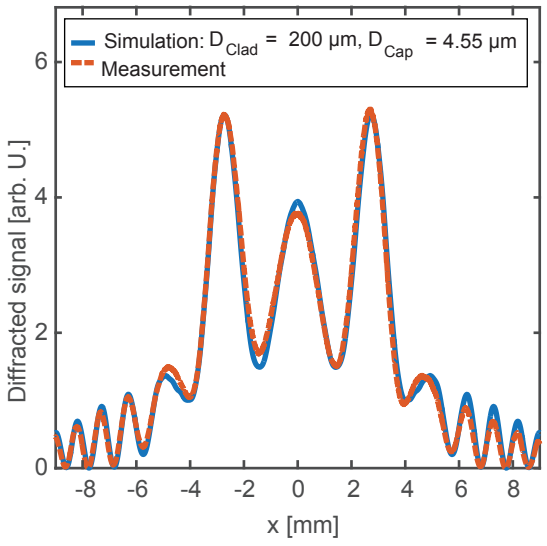

Figure 4.10: Comparison of measured and simulated signals. The investigated fiber was characterized by the vendor with an approximate capillary hole diameter of $D_{\mathrm{Cap}} = 4 - 5\mu m$. For the simulation a capillary hole diameter $D_{\mathrm{Cap}} = 4.55\,\mu m$ was used, where the closest agreement between measurement and simulation was achieved.

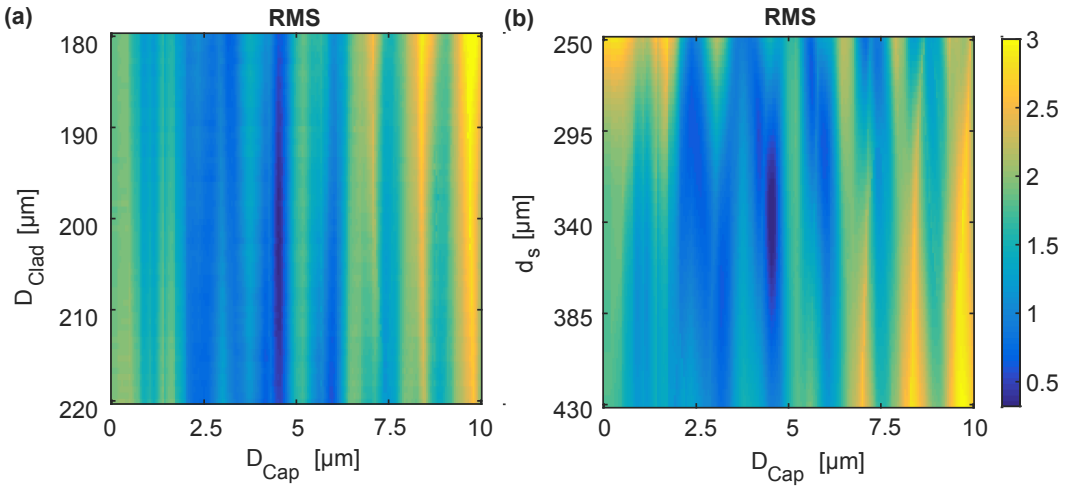

Figure 4.11: Calculation of the relative RMS-error according to Eqn. (4.2) between the measured and simulated signal, where (a) the source distance is fixed to $d_s = 340$µm and (b) the cladding diameter is fixed to $D_{\text{Clad}} = 200$µm. The investigated fiber was characterized by the vendor with an approximate capillary hole diameter of $D_{\text{Cap}} = 4 - 5$µm.

the retrieved fiber diameter is approximately $\Delta D_{\text{Clad}} \approx \pm 10$µm and for the source distance $\Delta d_s \approx \pm 20$µm. As an advantage, the cladding diameter needs not to be considered explicitly within the optimization. In particular, it will be sufficient to rely on the diameter, which is monitored during the fabrication process. Moreover, a strong sensitivity in the RMS-deviation is realized towards the capillary hole diameter D_{Cap}. A narrow, deep and distinctive minimum is found, which allows to retrieve the capillary hole diameter with high accuracy $\Delta D_{\text{Cap}} \approx \pm 100$ nm. This manifests the reliable ability of the methodology to characterize the inner structural composition of these fibers and to enable a parameter monitoring during fabrication. In particular, for this purpose it is suggested to build up a look-up table, where the individual simulation results are stored. During fabrication these results are used to compare the measurements with the simulations.

Overall, this can improve the as-build quality of fibers and therewith guarantee their optical functionality. Nevertheless, local minima are apparent in the RMS-deviation of the parameter scan, which are separated by approximately $\Lambda_{\text{Cap}} \approx 1.5$µm. Again, their appearance is explained by the holographic detection process being sensitive to both amplitude and phase information of the diffracted signal by the capillary. Relying on the thin-element approximation an associated phase change of 2π equals a length difference of $\Delta z \approx 1.4$µm. This value is in good agreement to the experimental finding. Nevertheless, by changing the diameter of the capillary hole, of course, the amplitude of the diffracted signal changes, which leads to distinguishable RMS-deviations in these local minima. Hence, a unique capillary hole diameter can be retrieved. To circumvent the appearance of the local minima one might change the coherence of the initial source. Currently a nearly monochromatic Helium-Neon laser at a wavelength of $\lambda = 632$nm with a small spectral bandwidth is used. Alternatively, one might use a LED with an increased bandwidth. This will diminishes coherent influences and the the local minima might disappear in the merit function. Nevertheless, these refinements are beyond the scope of this current assessment.

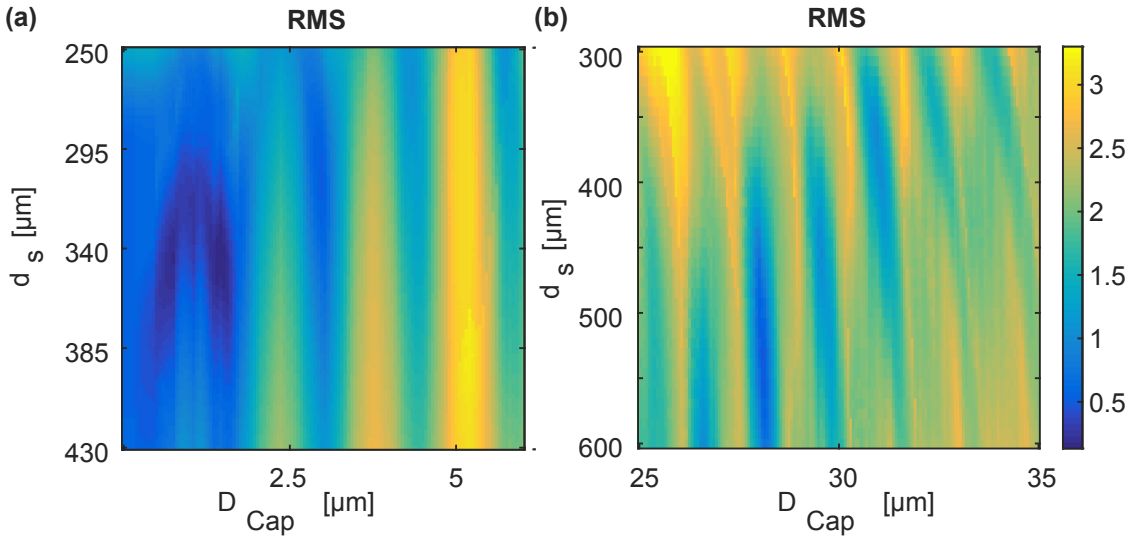

Figure 4.12: Calculation of the relative RMS-deviation by varying the initial source distance and the capillary hole diameter for a fixed cladding diameter. Respectively in subfigure (a) and (b) the results are shown for capillaries with approximate hole diameters of $D_{\mathrm{Cap}} = 1.5$ µm and $D_{\mathrm{Cap}} = 29$ µm

However, one particular problem arises in case the changes in the amplitude modulations are weak upon varied capillary hole diameters. In these cases individual local minima become indistinguishable and the retrieved parameters become ambiguous. This situation is realized for the investigation of capillary fibers with small hole diameters comparable to the used wavelength. To discuss this issue in more detail, Fig. 4.12 (a) shows the RMS-deviation for a capillary with a hole diameter of approximately $D_{\mathrm{Cap}} \approx 1.5$µm. Two local minima are apparent for hole diameters of $D_{\mathrm{Cap}} = 0.7$µm and $D_{\mathrm{Cap}} = 1.46$µm respectively. The RMS-value for the larger diameter is approximately 30% lower than the RMS-value for the smaller diameter and a conclusive parameter retrieval is still possible. Nevertheless, by further decreasing the hole diameter below one micrometer the local minima become indistinguishable. Then, the diffracted signal approaches the so-called quasi static limit, i.e., the Rayleigh scattering regime, and the diffraction response is less distinctive. This issue might be overcome by relying on a smaller illumination wavelength, which shifts the quasi static limit to smaller diameters. Moreover, the impact of an initial polarization becomes a stronger impact on the outcome of a measurement in these cases. Hence, this issue could be used to also assess capillaries with small diameters by relying on distinct TE- and TM-polarized measurements. Nevertheless, this also requires to adapt the simulations towards polarization resolved approaches. In this two dimensional situation the problem is rigorously described by a Helmholtz equation for the electric or magnetic field components for TE- or TM-polarization respectively (see Eqn. 2.5 for reference). Hence, the wave propagation method might still be used in this case. Nevertheless, the WPM neglects backward propagating field components, which might be problematic for the assessment of small capillary hole diameters. In particular, resonant whispering-gallery modes might be excited inside the capillary, which affect the outcome of a measurement. Then, fully rigorous solution techniques need to be used to predict the outcome of a measurement.

Finally, the improved in-line holographic measurement setup was used to assess large capillary

hole diameters of up to $D_{\mathrm{Cap}} = 30\mu\mathrm{m}$. The respective RMS-deviation is shown in Fig. 4.12 (b). In this case a capillary hole diameter of $D_{\mathrm{Cap}} = 28.03\mu\mathrm{m}$ was retrieved. The investigation of capillary hole diameters that are even larger was omitted as in these cases no accuracies of up to 100nm are needed. In this size regime, according to Mie-theory, the response approaches the so-called geometric limit. Thus, simple geometrical ray trace might be sufficient to determine the diameter of the capillary hole. In this case, it might be possible to retrieve the diameters by evaluating deflection angles of an initial beam with a small waist scanned across the fiber diameter in a similar manner as described by Watkins [141]. This idea is reconsidered also in the following section as a further refinement to improve the experimental methodology.

4.3 Summary

This chapter focused on the development of a noninvasive characterization technique of optical fibers, which potentially is suitable for the integration into their fabrication process. To this end, an in-line holographic measurement principle was introduced and evaluated. In this scenario, the investigated fiber was side illuminated by a monochromatic and coherent beam and the created diffraction pattern was monitored on a distant detector. In contrast to conventional in-line holographic measurement approaches, strong index-contrasts between glass and air were involved in the considered scenario. As a consequence, algorithms based on the Born- and Rytov approximation, which are conventionally used for the evaluation of in-line holographic measurements, remain no longer valid. Hence, alternative evaluation strategies are required. Here, these measurements were directly compared to simulations of the entire scenario based on the wave propagation method. A parametric optimization enabled the characterization of the investigated structure. Nevertheless, the originally proposed setup to characterize fibers was limited by several aspects. In particular, measured signals were characterized by highly oscillating fringe patterns. Moreover, to retrieve structural informations about the inner composition of fibers, weak amplitude modulations had to be evaluated in the otherwise strongly modulated signal. This, of course, sets high demands for the measurements and similarly also for their numerical evaluation. To overcome these challenging aspects the originally proposed setup was modified, especially to improve the signature of a fiber core in a measurement. To this end, the incoming beam diameter was reduced, which, in turn, increases the relative amount of diffracted energy by the fiber core. This enhances its detectability within a measurement. Moreover, the incoming beam diameter was even reduced below the diameter of the fiber. As a consequence, the in-line holographic measurement principle breaks apart for the assessment of the outer cladding diameter. This strongly reduces the high frequent modulations, which were inherent to the measurements relying on the original setup. This modified setup was used to characterize capillary fibers and shows a high sensitivity to changes of the capillary hole diameter. In particular, this value was retrieved with an accuracy of up to 100 nm. However, at this current stage the setup was only evaluated as a proof-of-principle study. The ability to characterize micro structured fibers with an increased complexity has not been investigated. In particular, the potential of the setup to assess photonic crystal fibers should be investigated. However, in this case the computational effort of the simulations increase. In particular, the photonic crystal structure needs to be parametrized properly, which will increase the computational complexity in the

optimization. One particular challenge in these optimizations will be the treatment of the local minima. However, as discussed previously, lowering the temporal coherence of the source might help.

Currently, the refined setup does not enable the accurate assessment of the outer cladding diameter of the fiber. To also overcome this limiting aspect a further improvement of the setup is shortly discussed in the following. This refinement was not implemented and should be viewed as a potential future outlook. In a first step the underlying conceptual idea is discussed and in a second step a potential implementation is introduced. Additional insights about the investigated fiber might be gathered if the illuminating beam is scanned over the entire cross section of the fiber. In particular, an easy characterization of the outer cladding diameter becomes possible in this case. If the illuminating beam is placed outside the fiber, the unperturbed beam profile is measured. However, an immediate perturbation of the beam profile should be measurable as soon as the beam is affected by the outer cladding diameter. In particular, this observation could be used to measure the outer diameter. Moreover, by scanning the beam throughout the fiber one might measure the deflection angles caused by the fiber. In the framework of a ray-based model additional insights could then be gathered at low computational cost, which is similar to the idea as introduced by Watkins [141]. Additionally, impurities in the fiber material should be easily observable. In particular, without a perturbation inside the fiber the overall profile should maintain a nearly Gaussian profile. Any disturbances should directly be visible as a perturbed beam shape. Finally, the in-line holographic measurement principle for the assessment of the fiber core remains entirely unaffected and the evaluations should be similarly possible.

To realize this conceptual idea in practice, a proper illumination unit should be designed. In particular, one might use an initial laser beam whose angular direction is controlled by a galvanometer scanner. This beam is focused by a cylindrical lens oriented parallel to the investigated fiber. Then, a light sheet is generated in the focus, which is used as initial field. Using an elongated light sheet instead of a Gaussian spot improves the signal to noise ratio within the measurements. In this case, the entire CCD-matrix of the sensor is illuminated more homogeneously along the symmetry direction. Finally, by changing the incidence angle of the initial laser beam via the galvanometer scanner the lateral spot position changes. Hence, the position of the illuminating light sheet with respect to the illuminating fiber could be controlled. This could enable the improved assessment of optical fibers.

5 Integrated Beam Shaping

Specifically tailoring the illumination distribution in an optical system is of special significance for various applications. In laser-based material processing tailored focal field distributions are required to improve uniformity and accuracy in the material modifications. Therefore, top-hat profiles are often required, e.g., to enable a high slope steepness in laser cutting. Moreover, optical tweezers and atom traps also strongly benefit from tailored focal field distributions. There, a realized intensity distribution determines the trapping potential, which is a critical influence in these applications [142].
Finally, several modern measurement principles rely on a structured illumination, i.e., the projection of a predefined pattern on a sample. Analyzing this influence of a tailored lightning on the outcome of a measurement can reveal deeper insights about the sample. By a series of measurements under different illumination conditions an increased information content is gathered. Then, individual measurements are digitally processed and merged to give a final result, which is often referred to as computational sensing. This coarse idea is realized in different experimental methodologies, which allows the assessment of vastly different application scenarios. On the one hand, structured illumination enables to retrieve three dimensional structural information of macroscopic samples [143, 144], which is of particular importance in quality assurance. Moreover, a tailored lightning is also applied within modern surface metrology techniques, named tilted wave interferometry [22]. This enables to assess strongly curved aspheres, which otherwise are hard to evaluate. Finally, structured illumination is used to increase the resolution in conventional imaging systems and in microscopy, known as ptychography [145] and structured illumination microscopy (SIM) [16, 17].
In particular, in SIM different complex illumination patterns [146] are projected into the focal region of the microscope. Referring to the Abbe limit, the post processing of these measurements allows to increase the resolution by a factor of two. These tailored illumination patterns are conventionally achieved by specifically altering the phase of an initial beam in the far field and focusing this modified beam into the focal region. This is realized by a specifically tailored

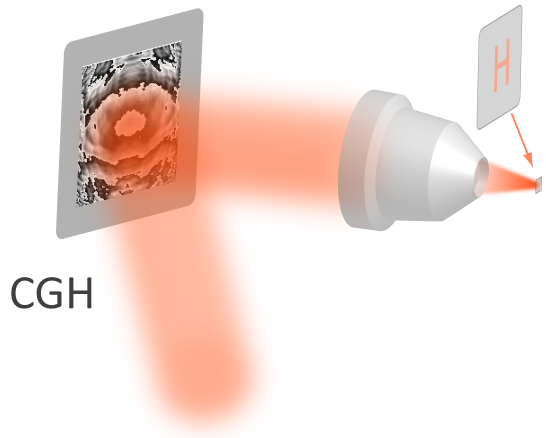

Figure 5.1: Schematic sketch of the beam shaping setup to realize tailored focal field distributions. The phase of an initial beam is altered by a specifically designed computer generated hologram (CGH) in the far field. This modified beam is focused in a Fourier-arrangement, which permits to realize a tailored focal field distribution.

phase mask, i.e., a computer generated hologram (CGH), placed in the focal plane of a Fourier-setup (see Fig. 5.1). To be more precise, conventionally either spatial light modulators (SLMs), digital micromirror devices (DMDs) or diffractive optical elements (DOEs) are used. Then, the

pixelation of the SLM/DMD or the layered height profile of the DOE due to the constraints of mask based lithography leads to the excitation of higher diffraction orders. This induces parasitic false light, which is seen as a strong zeroth order peak or ghost images. Moreover, inherent to these approaches are alignment sensitivities to adjust the individual components with respect to each other. This demands particular care and lowers the flexibility of these setups to be easily adapted to varying experimental conditions. In addition, the size of these systems is macroscopic. This restricts the applicability of these systems in different technological applications such as endoscopy. Overcoming these limitations is desirable to pave the way for novel applications [147–149].

In this chapter a novel concept is introduced to realize tailored focal field distributions in a highly miniaturized approach. To this end, a diffractive optical element is realized monolithically on the tip of an optical fiber, which allows to redistribute the initial fundamental Gaussian eigenmode of the fiber into the target field distribution. A design methodology is introduced, which results in continuous surface profiles with reduced slope steepness. These smooth diffractive optical elements are referred to as freeform holograms in the following (see Fig. 5.2). They allow to

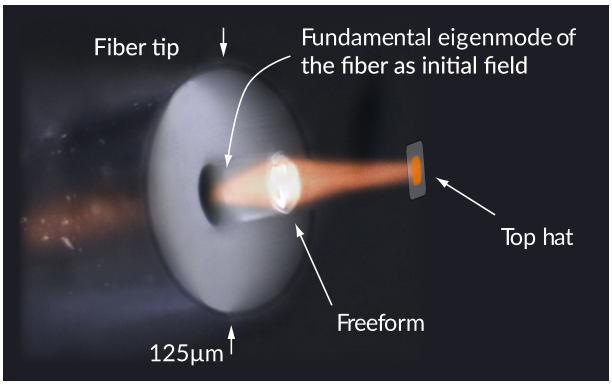

Figure 5.2: Illustrative sketch of the setup to realize integrated point spread function engineering. A freeform optical surface is realized on the tip of an optical fiber by direct laser writing, which enables the redistribution of the fundamental eigenmode of the fiber into a desired field distribution, e.g., a top hat.

overcome apparent restrictions in conventional diffractive beam shaping approaches. In particular, these freeform holograms allow to suppress perturbing false light, ghost images, and speckle effects [150], which are main challenges in conventional diffractive beam shaping [81, 151, 152]. However, these designed freeforms require a manufacturing process, which is able to realize these continuous surface profiles with a required accuracy. Conventional mask based lithographic processes only enable the realization of diffractive optical elements by a coarse layering as defined by the number of used masks. In turn, gray-scale lithography and femtosecond two-photon direct laser writing can overcome these limitations. Especially the latter one enables the creation of highly accurate, complex three-dimensional micro-optical components [3, 153] even on the tip of optical fibers [90, 93, 154–158]. Hence, two-photon direct laser writing is used and assessed to realize the designed freeform holograms.

The following chapter is structured as follows: First, the overall design methodology is introduced in the following Sec. 5.1. Second, the appending Sec. 5.2 discusses the fabrication of the designed freeform holograms and the overall experimental realization of the integrated beam shaping concept.

Results presented in this upcoming chapter were developed in a strong collaboration with Simon Thiele from the *Institut für technische Optik* in Stuttgart. The individual experiments were planned and designed together. The entire fabrication of designed structures and their

experimental characterization was performed by Simon Thiele. The optical design of freeform holograms and the numerical analysis of measured data was performed without the aid of this colleague. All the individual results were interpreted together, which formed the basis for the planning of additional experimental investigations. Finally, these insights were used to overcome experimental restrictions and challenges, which resulted in the proposed beam shaping approach as discussed in Sec. 5.2.3.
There is a planning of a patent application regarding this integrated beam shaping concept and individual parts of the presented results are summarized in a manuscript intended for publication.

5.1 Optical design of freeform holograms

5.1.1 General design methodology

For the design of a surface profile that enables the redistribution of an initial incoming beam into a desired target field distribution two different approaches are distinguished in general: Refractive and diffractive beam shaping. The prior considers a mapping to convert an initial intensity distribution into a desired one. Then, every initial ray described by $(x_{\mathrm{Initial}}, y_{\mathrm{Initial}})$ is mapped to a new location $(x_{\mathrm{Target}}, y_{\mathrm{Target}})$ in the target plane. This redistribution permits the realization of the target field distribution [151, 159]. In a subsequent step the actual freeform is calculated, which refracts individual incoming rays according to this mapping. The explicit choice of a mapping is not unique. However, there is only one optimal mapping, for which the cumulated distances $\sqrt{(x_{\mathrm{Initial}} - x_{\mathrm{Target}})^2 + (y_{\mathrm{Initial}} - y_{\mathrm{Target}})^2}$ for the individual rays are minimal. Hence, this mapping corresponds to minimal deflection angles of the initial ray distribution and therewith to a minimization of surface gradients. This, of course, is beneficial for a manufacturing process. Moreover, these refractive approaches result in smooth freeform surfaces without discontinuities, which prevents perturbing straylight and speckle effects [96, 160]. Nevertheless, strong contrasts in the final intensity distribution still result in curvature peaks at the freeform surface. This can set high demands for the manufacturing process. In addition, the optical design relies entirely on a geometric optical approach, which neglects any influence of diffraction.
Alternatively, diffractive beam shaping is based on a wave-optical approach and considers the tailored interference of individual plane waves. Their superposition yields the desired field distribution in the target plane. To this end, the phase of an initial monochromatic beam is altered by a specifically designed computer generated hologram (CGH). Conventionally, the initial CGH-plane is Fourier-conjugated to the final target plane. This is achieved by placing the CGH in the focal plane of a Fourier setup or by placing the target plane at a sufficiently large distance, i.e., the farfield. High contrasts in a final target intensity are realized more easily due to destructive interference effects. To design these computer generated holograms modified formulations [142, 161–166] of the original Gerchberg-Saxton algorithm, often referred to as iterative Fourier transform algorithm (IFTA) [167, 168], are usually considered. These algorithms compute the required phase change $\Delta\varphi(x, y)$ by which an initial field must be changed to realize a desired target field distribution. To convert the designed phase profile $\Delta\varphi(x, y)$ into an

actual surface profile $z(x, y)$ of the diffractive optical element, the thin-element approximation (TEA) is usually considered. In these coherent approaches, perturbing zeroth order straylight, ghost images due to the excitation of higher diffraction orders, and speckle effects are a main challenge [96, 142, 152, 160, 161, 165, 166, 169].

To be more precise, phase vortices can emerge during the optical design. Then, phase spirals that wind from zero to 2π appear in a designed phase $\Delta\varphi(x, y)$. These vortices are a primary source of straylight [152]. Moreover, steep edges occur in a designed surface profile due to phase wrapping (see Fig. 5.3). As discussed in Sec. 2.4.1, these edges cause additional false light, which lowers the overall performance and which are not predicted by simulations relying on the TEA. Finally, inaccuracies of a manufacturing process lead to deviations in between a realized

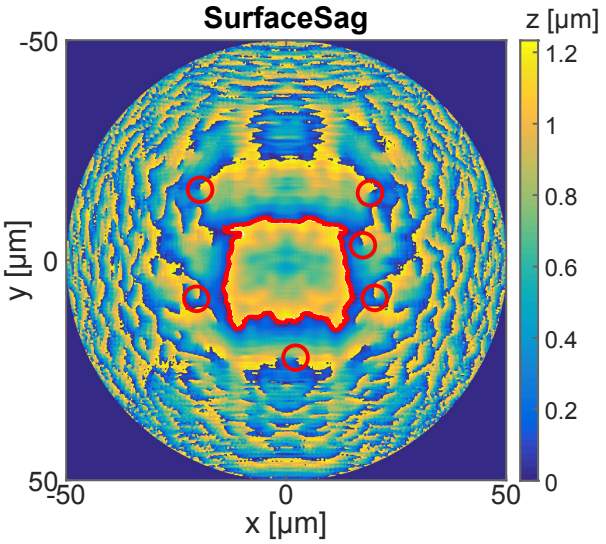

Figure 5.3: Visualization of phase vortices (Red circles) and steep edges due to phase wrapping (Red solid line) in a designed diffractive optical element. A conventional IFTA-algorithm [167] was used to design the surface profile for the considered design scenario, which is discussed in this chapter.

and a designed diffractive optical element. This, of course, leads to additional parasitic straylight, which degrades a realized target field distribution. As a consequence, the design algorithm should be adapted to converge to surface profiles, which are beneficial for a manufacturing process. For the considered fabrication technique of two-photon direct laser writing, small feature sizes and rapid changes in a designed surface profile should be avoided. In particular, the smaller these feature sizes are, the higher are the requirements for their manufacturing. As a consequence, the aforementioned refractive beam shaping seems superior in this case as a surface is achieved with smallest possible gradients.

However, in the considered case refractive beam shaping cannot be applied directly. Due to the microscopic size dimensions of the beam shaping unit on the tip of an optical fiber, diffractive influences cannot be neglected. Alternatively, the advantages of both approaches might be combined by suppressing perturbing zeroth order straylight and speckle effects without neglecting diffractive influences. To this end, an optical design should result in a surface profile without discontinuities and reduced gradients. In general, there are several approaches, which seem promising to design continuous diffractive optical elements. On the one hand, refractive beam shaping could be used to generate an initial phase guess, which is further modified by an IFTA routine. This idea was introduced by Kämpfe *et al.* in Ref. [160]. On the other hand, it was suggested by Cumme *et al.* in Ref. [170] to gradually change the unperturbed beam profile in the target plane to the desired field distribution within the IFTA design. This should result

in a smooth convergence of the IFTA algorithm and reduce the emergence of phase vortices. These design strategies still result in a wrapped phase profile, which is removed in a final step by an unwrapping algorithm, e.g., the Goldstein algorithm [171]. Nevertheless, these seminal approaches do not directly restrict gradients in the phase profiles. Moreover, it is difficult in this framework to directly include additional manufacturing constraints, e.g., a maximum curvature in a surface, within the design. Hence, there is a high potential to advance these design algorithms, which could further improve realized target field distributions in comparison to the early pioneering approaches [160, 170].

Alternatively, in the following a design methodology is introduced, which optimizes directly onto an unwrapped phase profile. Hence, the algorithm optimizes directly onto the surface profile in the framework of the TEA. This is beneficial for various reason. On the one hand, surface gradients can directly be restricted. On the other hand, additional manufacturing constraints, e.g., surface curvatures, can easily be considered within the design. Finally, there is no need to use phase unwrapping algorithms, which reduces the computational effort. In the following, the conceptual design idea will be introduced first, while afterwards the individual steps are discussed in detail. To design the freeform hologram, a modified formulation of the algorithm proposed by Brenner in Ref. [150] is used. In particular, the design methodology corresponds to an adapted IFTA concept. It calculates the phase change $\Delta\varphi(x, y)$ an initial field needs to be altered to realize a target intensity in a distant plane. Thereby, the phase of the field in the target plane is not specified. This degree of freedom is utilized to minimize the deviation between desired target intensity and an actual realization. In contrast to the traditional IFTA-algorithm the 2π-periodicity of the phase is directly removed and an unwrapped phase profile is achieved without additional computational efforts. Moreover, maximum gradients in the phase values $\Delta\varphi(x, y)$ are restricted in the algorithm [150]. Nevertheless, there are many degrees of freedom within the design, since local phase values $\Delta\varphi(x, y)$ are still allowed to vary nearly arbitrary. Hence, the algorithm might converge to a local minimum and phase gradients could be reduced further. To overcome this issue, an idea of classical freeform design is adapted into diffractive beam shaping.

In classical design, a surface profile is conventionally described by a polynomial representation. In early optimization cycles only few coefficients of the freeform description are allowed to change. These polynomials typically represent low spatial frequencies in a surface profile. This results in a coarse optimization, which is refined and improved subsequently by allowing additional higher order freeform terms to vary. This procedure typically results in an improved convergence and therewith a better performance of the design. To adapt this idea into the optimization of the freeform hologram, the phase $\Delta\varphi(x, y)$ is filtered in every optimization cycle by a Gaussian function $\Delta\varphi(x, y) \longrightarrow \Delta\varphi(x, y) \circledast e^{-\left(\frac{x^2+y^2}{2\sigma^2}\right)}$. The same procedure is applied to the target intensity. During the optimization, the width σ of this blurring filter is gradually lowered. Hence, in early optimization cycles only the low frequency information of the image is realized by the imprinted phase. During the subsequent refinement, narrower details are adapted (see Fig. 5.5). This results in an improved convergence with overall lowered gradients in the final phase profile. This will improve the manufacturability of the designed surface profiles. In par-

ticular, narrow features in a final surface profile are reduced as much as possible, which reduces the overall accuracy requirements of the manufacturing process.

5.1.2 Detailed design procedure

To introduce the design methodology in more detail, in a first step the traditional IFTA algorithm will be discussed. In a subsequent step the modifications are introduced. A schematic flowchart of the original IFTA algorithm is depicted in Fig. 5.4. In an initial step (**0.**) the modulus of the incident field $|E_0(x,y)|$ and an arbitrary chosen phase $\Delta\varphi(x,y)$ are considered. In a subsequent step (**I.**), this initial field $E_{\mathrm{CGH}}(x,y) = |E_0(x,y)|e^{i\Delta\varphi(x,y)}$ is propagated to the target plane $E_{\mathrm{Target}} = \mathcal{P}_{z_{\mathrm{Target}}}\{E_{\mathrm{CGH}}\}$, where $\mathcal{P}_{z_{\mathrm{Target}}}$ denotes the propagation between freeform hologram and target plane specified by the distance z_{Target}. In case the target plane is Fourier conjugated to the initial one, i.e., the farfield or the focus of a Fourier setup, the propagation operator reduces to a Fourier transform. Otherwise, the operator is implemented via a freespace propagation. The latter corresponds to the considered case, where a finite distance was chosen and the propagation operator was implemented via the angular spectrum of plane wave decomposition [172]. In a next step (**II.**), the modulus of the calculated field $E_{\mathrm{Target}} = |E_{\mathrm{Target}}|e^{i\varphi_{\mathrm{Target}}}$ is modified. In the original IFTA $|E_{\mathrm{Target}}|$ is replaced via the target intensity $I_{\mathrm{Ideal}}(x,y)$ as $|\tilde{E}_{\mathrm{Target}}| = \sqrt{I_{\mathrm{Ideal}}(x,y)}e^{i\varphi_{\mathrm{Target}}}$. This modified field is propagated back to the plane of the freeform hologram $E_{\mathrm{Initial}} = \mathcal{P}^{-1}_{z_{\mathrm{Target}}}\left\{\tilde{E}_{\mathrm{Target}}\right\} = |E_{\mathrm{Initial}}|e^{i\varphi_{\mathrm{Initial}}}$ in a subsequent step (**III.**). Finally, in the initial plane the modulus $|E_{\mathrm{Initial}}|$ is replaced via the incident field as $|E_{\mathrm{Initial}}| = |E_0|$ in step (**IV.**). In addition, the phase $\Delta\varphi(x,y)$ is identified via $\varphi_{\mathrm{Initial}}$ in the original IFTA and a new iteration starts. These iterations **I.-IV.** are repeated until the deviation between current intensity and the ideal one are sufficiently low. The convergence of this algorithm is slow and depends strongly on an initial phase guess $\Delta\varphi(x,y)$ used in the first iteration [161]. In addition, speckle effects are a main challenge and degrade the overall performance [96, 142, 152, 160, 165, 166].
To improve the convergence and the quality of realized target field distributions the mixed-region amplitude freedom (MRAF) concept was proposed [142, 165, 166]. In particular, it modifies the substitution of the field modulus in between steps **II.** and **III.**. A mixing parameter $0 < m < 1$ is introduced and the field is substituted as $|\tilde{E}_{\mathrm{Target}}| = m\sqrt{I_{\mathrm{Ideal}}} + (1-m)|E_{\mathrm{Target}}|$. In addition, in the target plane an area $\mathcal{A}$ is defined, called the signal region (SR). Then, the field in the target plane E_{Target} is only replaced within the predefined area. Hence, outside the signal window the field may vary arbitrary.

$$
\begin{aligned}
|\tilde{E}_{\mathrm{Target}}(x,y)| &= \begin{cases} m\sqrt{I_{\mathrm{Ideal}}(x,y)} + (1-m)|E_{\mathrm{Target}}(x,y)| & (x,y) \in \mathcal{A} \\ |E_{\mathrm{Target}}(x,y)| & \text{else} \end{cases} \\
\mathcal{A} &= \text{Signal region}
\end{aligned}
$$

The suggested MRAF procedure improves the convergence and signal quality of the original IFTA algorithm [142, 165, 166]. Nevertheless, in a final phase profile strong gradients are still immanent and the phase is wrapped, i.e., 2π periodic. To overcome these issues the final iteration steps **IV.** $\longrightarrow$ **I.** are modified. To achieve an unwrapped phase profile only differences between subsequent iterations are added onto an otherwise continuous final phase $\Delta\varphi \longrightarrow$

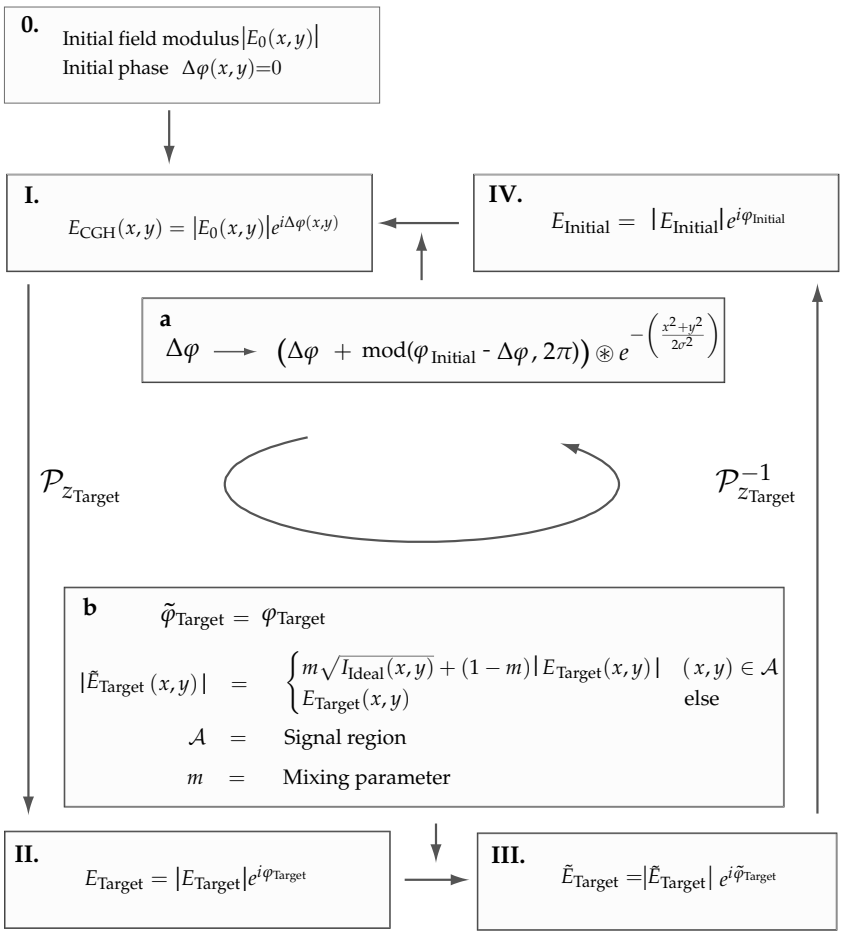

Figure 5.4: Flowchart of the modified IFTA algorithm to calculate the freeform hologram. Step **a.** corresponds to the filtered formulation of the algorithm as introduced by Brenner *et al.* [150]. Step **b.** corresponds to the MRAF procedure [142, 165, 166].

$\Delta\varphi + \mathrm{mod}(\varphi_{\mathrm{Initial}} - \Delta\varphi, 2\pi)$. This modification was suggested by Brenner in [150] [1]. Additionally, this phase profile is filtered by a Gaussian function in every iteration, where the corresponding width is gradually decreased. This reduces local surface gradients and enhances the convergence of the algorithm. To connect the width σ of the Gaussian filtering function to a physically meaningful quantity, the focusing of a Gaussian beam is considered. The minimal waist w_0 of this beam by focusing with a lens of numerical aperture NA is given as $w_0 = \dfrac{\lambda}{\pi \mathrm{NA}}$. Hence, the width of the Gaussian filtering function is identified via the numerical aperture $\sigma = \frac{\lambda}{\sqrt{2}\pi \mathrm{NA}}$.

5.1.3 Fundamental limitations in an achievable accuracy

The accuracy in a realized target intensity is not only influenced by the design methodology. Additionally, fundamental physical aspects limit a maximum resolution. They are discussed in the following. On the one hand, the initial mode field diameter, which illuminates the freeform hologram has a critical impact. It determines smallest feature sizes that can be realized in an otherwise ideal system. Roughly speaking, in the limit of a vanishing mode field diameter, i.e., a point source, the initial phase cannot be changed and therewith the illumination. In turn, for large mode field diameters the problem can be treated by geometrical optics and closed form expressions exist for the design process [159]. The influence of an initial mode field diameter (MFD) is explained by the Rayleigh criterion, which connects the MFD to an angular resolution

[1] In its original formulation by Brenner a filtering in Fourier-space was suggested to restrict maximum gradients. Here, this step is omitted, since a modified filtering operation is used.

$\Delta\theta \approx 1.22\frac{\lambda}{\mathrm{MFD}}$. In conventional diffractive beam shaping, i.e, CGH- and target plane are Fourier-conjugated, smallest feature details in the target intensity are directly described by this angular resolution $\Delta\theta$. Hence, a large mode field diameter can improve the quality of a realized target field distribution. In the considered beam shaping approach, a finite distance z_{Target} between the freeform hologram and the target field distribution will be considered. Then, the angular resolution might be converted into a spatial one $\Delta x = 1.22\frac{\lambda}{MFD}z_{\mathrm{Target}}$ by identifying $\Delta\theta \approx \frac{\Delta x}{z_{\mathrm{Target}}}$. Hence, an increased MFD can improve the convergence of IFTA algorithms. Moreover, a larger MFD also lowers centering tolerances of the freeform hologram with respect to the center of the initial field [155, 173].
To increase this MFD within the considered integrated beam shaping approach, a rather simple idea is used. Instead of realizing a diverging lens on the fiber tip, free space propagation diffraction is considered. The optical fiber used within the experiments (Thorlabs SM-630HP) features a numerical aperture of approximately NA = 0.12, which similarly defines the divergence angle of the guided eigenmode in air. As a consequence, no diverging lens needs to be realized onto the fiber core. The diameter of the final beam shaping unit was chosen equally to the fiber diameter. Hence, as limiting aperture the value of the cladding diameter was assumed and the MFD was chosen as MFD $\approx$ 50µm. This value takes into account, that the MFD of a Gaussian beam is smaller than its geometric footprint. By choosing the MFD considerably larger, diffraction effects originating from the aperture, i.e., the surrounding edges of the beam shaping unit, might disturb a realized target intensity. This mode field diameter is achieved for the initial eigenmode to diffract over a distance of $\Delta z = 250$ µm in air. In this case the actual hologram is realized on a scaffold structure placed at this desired distance from the fiber tip (see Fig. 5.8 (a)). Alternatively, also a solid cylinder made out of the photoresist material used within the manufacturing process could be considered. This photoresist is characterized by a refractive index of $n \approx 1.51$ and the corresponding cylinder height equals in this case approximately $\Delta z = 400$ µm. The hologram is realized on top.

An additional aspect, that influences the accuracy in a realized target intensity belongs to the conversion of the designed phase $\Delta\varphi(x, y)$ into the surface profile of the freeform hologram. As discussed in Sec. 1.2, the thin-element approximation (TEA) is inevitable in this case. It gives an analytic and direct connection between the surface topography and its induced optical effect. Nevertheless, the TEA overestimates the diffraction efficiency. To evaluate the validity and the accuracy of the TEA prior to a manufacturing step, a possible final design is assessed by simulations with the wave propagation method. A potential final design is only accepted if it provides satisfying results. Otherwise, the design is readjusted, e.g., by decreasing incremental step sizes of the Gaussian filtering width σ.

In the following, results of the proposed design methodology will be discussed. As initial field the fundamental eigenmode of a Thorlabs SM-630HP fiber, specified with a numerical aperture of NA= 0.12 and a core diameter of $D_{\mathrm{Core}} = 3.5$µm, is considered. As illumination source a fiber coupled LED (Thorlabs LED M625F2) at a wavelength of $\lambda = 0.63$µm is used. The expansion region of the mode is chosen as $\Delta z = 250$µm in air and this propagated field is then used during the design. In the early iterations, the large width of the Gaussian filtering function flattens an initial phase. As a consequence, during the design a collimated incoming beam is assumed. This

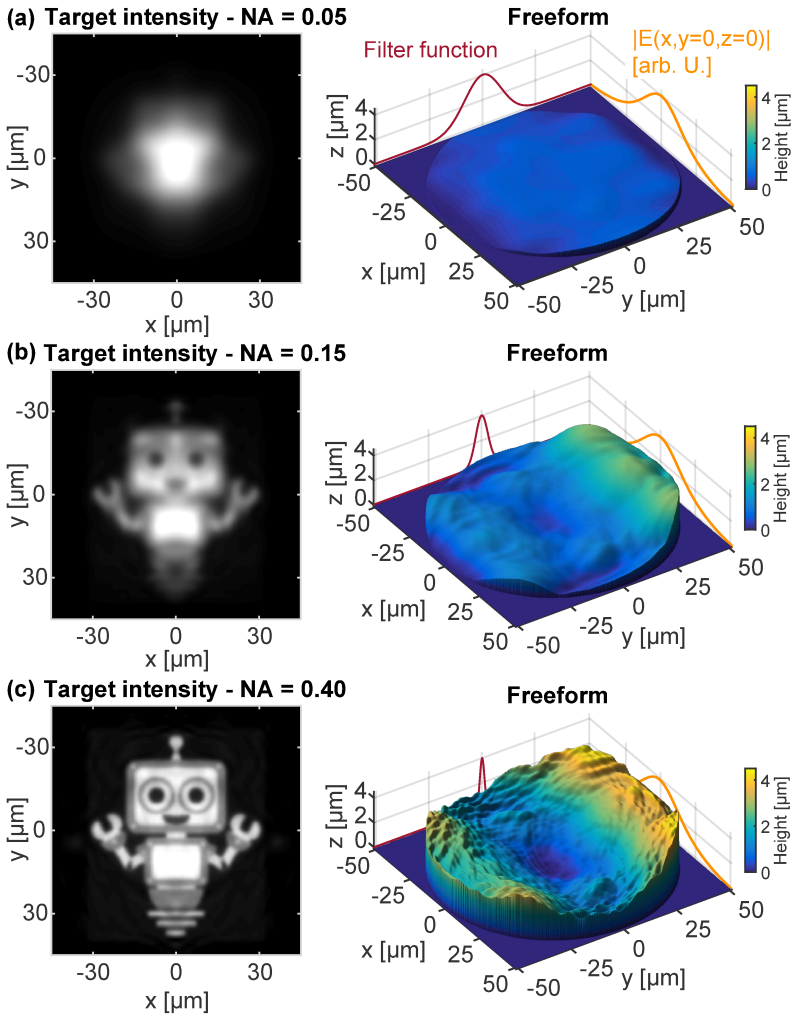

Figure 5.5: Feature sizes in the surface sag are increasing gradually during the design procedure. This is realized by a Gaussian filtering of the surface sag, where the corresponding width is adapted during the iterations. This allows a smooth convergence of the design algorithm and avoids the appearance of large gradients in the surface sag. In subfigures (a)-(c) design results of individual iteration steps are shown. Respectively, the simulated intensity in the target plane, i.e., $|E(x, y, z_{\text{Target}})|^2$, is shown on the left and the corresponding surface sag on the right.

issue could be resolved, in principle, by adding a collimating spherical profile to the freeform hologram. However, an initial spherical phase part will not significantly degrade the performance of the beam shaping unit. Simulations of a designed freeform hologram revealed, that an initial spherical phase part will lead to a magnification and a shift along the optical axis of the realized target intensity. Hence, by considering a magnification factor during the design also a spherical initial phase may be treated. Finally, the distance to the target intensity is set to $z_{\text{Target}} = 150$ µm. Corresponding results at different intermediate optimization steps are shown in Fig. 5.5.

5.1.4 Improved design methodology

In the previous section the optical design methodology was introduced, which enables continuous freeform holograms. In the following, a refinement of the procedure will be discussed, which can improve both the convergence in the optimization and final results. To this end, a preliminary optimization is established to calculate an initial phase guess φ_{Guess} for the realization of a final target intensity. Based on the outcome of this routine a slightly modified formulation of the original algorithm is further considered. It should be stressed at this point, that the methodology introduced in the following was not used within the experimental assessment of the conceptual idea in Sec. 5.2. In particular, the design modifications presented in the following were developed just after the experimental verifications.

To consider an initial phase guess in the original methodology, the calculation of the phase $\Delta\varphi(x,y)$ in between the steps **IV.** and **I.** (see Fig. 5.4) is modified

$$\begin{aligned} \phi &= \Delta\varphi_{\mathrm{Old}} + \mathrm{mod}(\varphi_{\mathrm{Initial}} - \Delta\varphi_{\mathrm{Old}}, 2\pi) \ , \\ \Delta\varphi_{\mathrm{New}} &= \varphi_{\mathrm{Guess}} + (\phi - \varphi_{\mathrm{Guess}}) \circledast e^{-\left(\frac{x^2+y^2}{2\sigma^2}\right)} \ . \end{aligned}$$

First, the unwrapped phase profile ϕ is calculated in an initial step. Then, the filtering process is only applied to the deviations between initial phase guess and the current phase. The remaining part of the algorithm remains unchanged. As an advantage, coarse features of the target intensity are already realized in the beginning. Within the optimization only finer feature details are adapted. This should further avoid stagnations in local minima and improve convergence. However, the major challenge concerns the estimation of an initial phase guess, which has a critical impact within the optimization. It is challenging for the original algorithm to readapt a wrong phase guess. In these cases the routine might not converge to a satisfying result. Without a proper preoptimization, as discussed in the following, a flat initial phase yielded best results.

To calculate an initial phase $\Delta\varphi(x,y)$ a parametric least square optimization is considered. In particular, the phase of the initial beam is described as a superposition of Zernike polynomials $Z_n(x,y)$ as $\Delta\varphi(x,y) = \sum c_n Z_n(x,y)$. The least-square algorithm varies the phase coefficients c_n to achieve a best accordance between the current realization and the target intensities. The degree of similarity is defined numerically as the objective value of a merit function. A more detailed description of this approach is provided by Böhme *et al.* in [174]. In the following, a maximum number of 144 Zernike polynomials were considered with a normalization radius of $R = 70$ µm. To improve convergence within this optimization not the entire number of Zernike-Polynomials were allowed to vary simultaneously. In an initial step only 9 Zernike polynomials were used, which correspond to primary aberrations. In subsequent optimization steps, the number of polynomials is increased gradually. To this end, polynomials corresponding to higher order aberration groups were allowed to vary additionally. In fringe ordering of the Zernike polynomials, these groups are identified by square natural numbers, i.e, $(3^2, 4^2, 5^2, ...)$ [98].

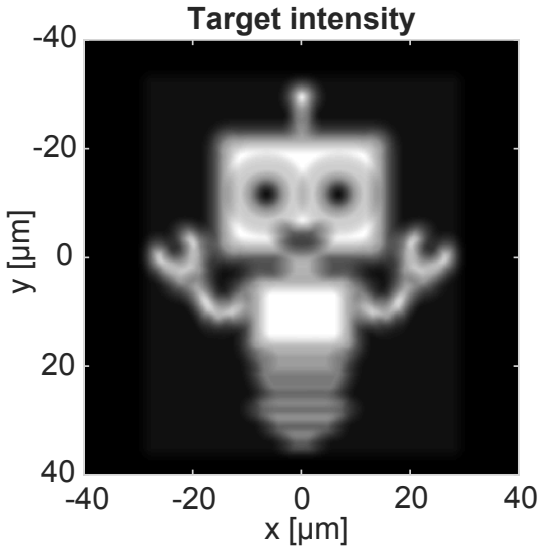

Figure 5.6: Filtered target field distribution used within the optimization algorithm to calculate an initial phase guess. The filtering procedure prevents the stagnation of the algorithm in local minima.

It turned out, that the optimization might stagnate in local minima by considering the target field distribution directly. In particular, fine details, e.g., steep edges in the profile, cannot be resolved properly by relying on the limited number of Zernike polynomials. In these cases parasitic interference effects emerged during the design. A Gaussian filtering of the original target field distribution helped to circumvent these problems. Then, this filtered field was used as a novel target intensity in the initial phase guess calculations (see Fig. 5.6). The RMS-error between the ideal and the current intensity distribution is used as a objective value for the merit function. The optimization in this case seemed less robust. In particular, interference fringes were immanent on a realized target intensity (see Fig. 5.7 (a)). To suppress their emergence an additional penalty criterion was introduced. To this end, the current field distribution E_{Current} was high-pass filtered by an adapted procedure prior to the RMS-calculation. Within this approach low-frequent features in the current field remain unaffected, while high frequent-features, i.e., the interference fringes, are artificially amplified. As a consequence, the parasitic interferences are weighted stronger within the RMS-error. Thus, the optimization converges to a result with reduced interference artifacts. The high-pass filter was heuristically optimized to achieve satisfying results and is defined in the Fourier-domain as $H = 1 + 5\left(1 - e^{-\left(\frac{\sqrt{{k_x}^2+{k_y}^2}}{\frac{k_0}{7}}\right)^{20}}\right)$. Roughly speaking, this filter corresponds to an inverted top-hat profile. On the one hand, for low spatial frequencies $k_x, k_y \ll \frac{k_0}{7}$ the filter takes a value of one. Hence, low spatial frequencies remain unaffected by the filter. On the other hand, for high spatial frequencies $k_x, k_y \gg \frac{k_0}{7}$ the filter takes a value of 6. Respectively, these frequency parts in the Fourier-transformed field $\tilde{E}_{\text{Current}}(k_x, k_y)$ are correspondingly amplified. This filter design yielded a significant improvement of the preoptimization. Nevertheless, there might be alternative filter designs that further improve the results.

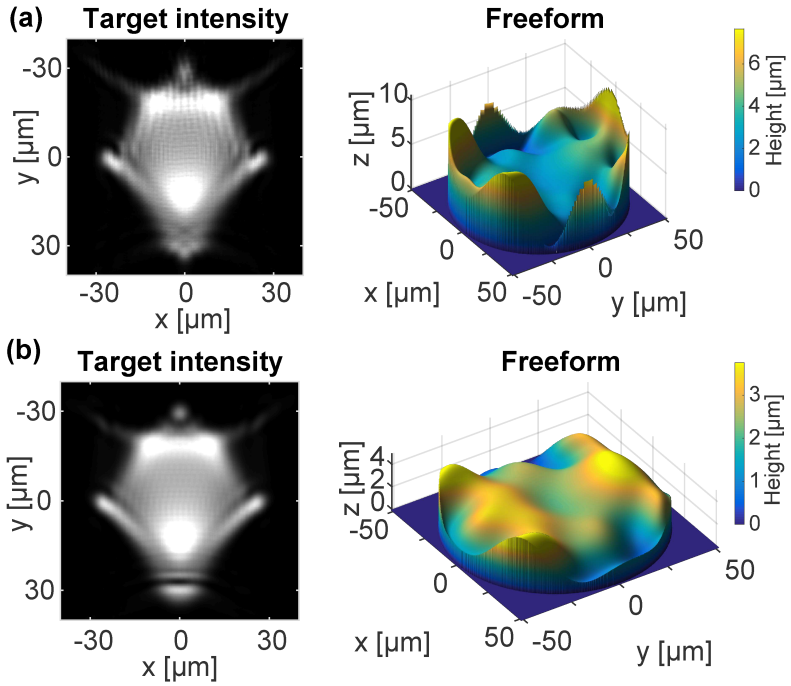

Figure 5.7: Preoptimization of the freeform hologram to calculate an initial phase guess $\Delta\varphi(x, y)$. The merit function is defined as the RMS deviation between target field distribution and current realization. (b) To avoid the emergence of parasitic interference effects the current field in the optimization is high pass filtered. This leads to a stronger weighting of the parasitic interference effects in the optimization.

5.2 Results

While in the previous section 5.1 the optical design of the freeform hologram was introduced, the realization of the integrated beam shaping unit will be discussed in the following. In particular, two photon direct laser writing is considered to realize the designed surface profiles. This additive manufacturing process is based on a non-linear photon absorption of photopolymers. In particular, a femtosecond laser-beam is tightly focused into a transparent photo-resist material and causes it to locally absorb light via a multi-photon absorption process. Then, the photopolymer molecules of the photo-resist absorb two or more photons simultaneously, which triggers a photo-chemical process. This selectively hardens the light-sensitive material and any unhardened photo-resist will be removed afterwards. Two-photon absorption is a second-order nonlinear process and therewith depends on the square of the light intensity $\propto I^2$ [175]. Hence, only inside the focal region of the tightly focused beam these material modifications take place. Moreover, due to the non-linear absorption mechanism, resolutions even below the diffraction limit are achieved. In the considered case, a Nanoscribe Professional GT setup in dip-in configuration will be used with a microscopic objective lens optimized for immersion applications and a numerical aperture of NA=1.4. This lens is immersed in the photo resist and lateral voxel sizes of approximately 200 nm and a typical length of 500 nm are ideally achieved. By moving the laser-beam along a predefined trajectory, arbitrary structures can be created. Hence, the process is similar to 3d-printing. Additional informations about the fabrication process are provided by Gissibl *et al.* in [154][2].

5.2.1 Vibrational disturbances during the manufacturing process

In this section, the first iterations to realize the beam shaping unit as introduced in Sec. 5.1 are discussed. To implement the conceptual idea, several requirements need to be fulfilled in a mechanical design. On the one hand, the fundamental eigenmode should increase its mode field diameter by free space diffraction. To this end, the freeform hologram needs to be realized in the specified distance of $\Delta z = 250\mu m$ to the actual tip of the fiber. Moreover, in the design a collimated beam was assumed. However, the wavefront of the expanded beam is curved. Hence, the beam should be collimated, which could be realized by an additional collimation lens prior to the hologram (see inset in Fig. 5.8 (b)). This requires a supporting structure to mount the lens. To realize the entire device in a single step, this supporting structure is also realized by direct laser writing and a corresponding CAD design is shown in Fig. 5.8 (a). At the bottom of the structure a hollow disc can be observed with a concentrically arranged hole, where the fundamental eigenmode enters the structure. This disc covers the area of the fiber and is of special importance to ensure the adhesive connection in between the fiber tip and the actual beam shaping unit. Hence, it is responsible for the mechanical stability of the entire device. A scaffold is attached to the disc, which mounts the actual freeform hologram. Individual struts need to be thin enough, that the diffracting eigenmode inside the scaffold is not affected.

[2]Overall, the design and the manufacturing of the integrated beam shaping unit are introduced rather independently from each other. While, this allows to display results coherently, it does not necessary follow a chronological order the individual insights were gathered. Actually, the design was developed and improved subsequently on the outcome of individual manufacturing iterations towards the final realization. In particular, it took nearly twenty iterations and subsequent refinements to achieve a satisfying performance of the beam shaping unit.

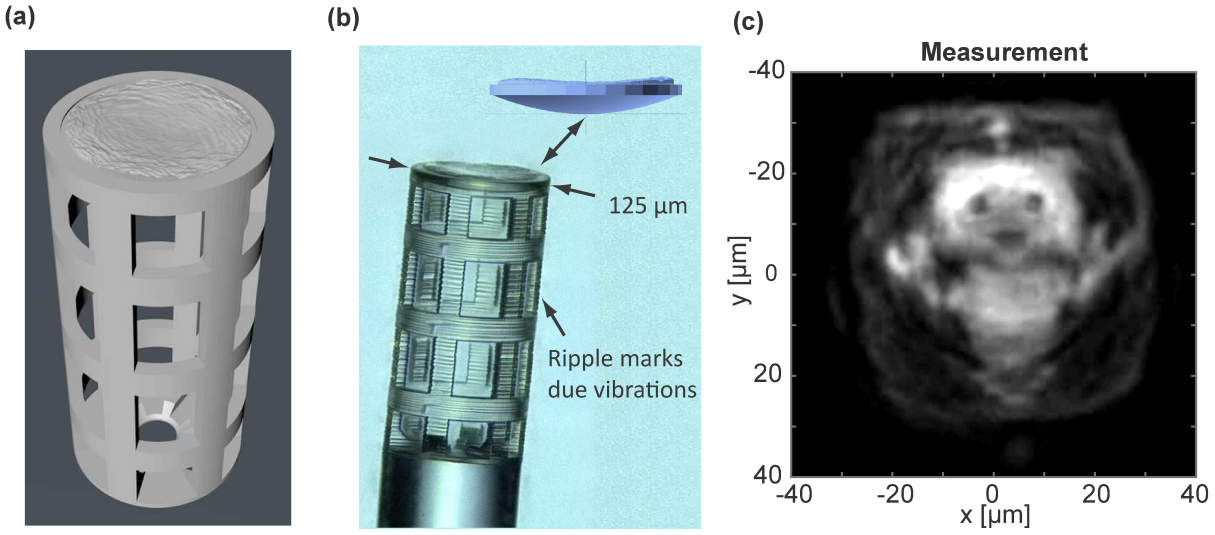

Figure 5.8: (a): CAD-design of the integrated beam shaping unit. A hollow supporting structure is considered to allow the fundamental eigenmode to diffract in air. This height equals $h = 250\mu m$. On top the beam shaping surface is attached. (b) Microscopic image of the realized structure on the tip of the optical fiber. (c) Measured focal field distribution of the integrated beam shaping unit. A fiber coupled LED (Thorlabs M625F2) with a spectral bandwidth of $\Delta\lambda \approx 15nm$ was used as the light source within the measurements.

Otherwise the nearly Gaussian beam gets perturbed, which, of course, degrades the quality of a focal field profile. In a subsequent step, the collimation lens is attached prior to the freeform hologram to flatten the spherical initial phase of the broadened fundamental eigenmode.
A microscopic measurement of a realized beam shaping unit is shown in Fig. 5.8 (b). Within the supporting structure, periodic disturbances in the individual scaffolds are evident. These are caused by vibrations within the manufacturing process and they result in a blurring of the realized freeform hologram. Hence, a degraded target intensity is expected. To assess the impact of the vibrations on the functionality of the beam shaping unit, Fig. 5.8 (c) shows a microscopic measurement of the realized field distribution in the target plane. Basic features of the robot image can be realized. Nevertheless, the overall accuracy of the realized focal field distribution is poor. These disturbances are explained by the vibrations of the fiber during the printing process. These vibrations only appear for the realization of micro-optical components on the tips of optical fibers. This suggests the fiber clamp or the fiber itself to be affected by any kind of a time-periodic vibration. To resolve the issue, different fiber clamps were investigated and compared. Moreover, additional experiments revealed, that the moving stage on which the fiber clamp is mounted, seems to be the most offending part. In particular, the fiber clamp is mounted at the edge of the stage. To position this clamp into the focus of the objective lens, the stage is moved nearly to its maximum traveling path. This might provoke additional disturbances resulting in the vibrations. Vibrational disturbances could significantly be reduced by changing the mounting of the fiber clamp and varying the actual position of the clamp on the stage. Based upon these results additional process parameters were investigated.

5.2.2 Accuracy assessment of the manufacturing process

The precision of finest feature details in femtosecond two-photon direct laser writing is influenced by environmental conditions, e.g., temperature, and process-related parameters. On the one hand, the initial laser power has a significant influence. In particular, the voxel size of the manufacturing process, i.e., the volume of hardened resist in a single shot, scales with the squared intensity $\propto I^2$ [176]. On the other hand, the photo-resist material used to create the intended structures has also a critical impact on finest feature sizes in a final structure. Hence, a strict definition of the accuracy is burdensome. To investigate these issues experimentally, the designed freeform hologram was imprinted for different photoresist materials and under different initial laser powers. In a subsequent step these surfaces were evaluated by confocal surface measurements (Nanofocus µsurf expert).

Exemplary, the impact of a photoresist material will be assessed in the following. In a first step, the beam shaping unit was realized by IP-S photoresist from Nanoscribe with a high viscosity. This latter aspect is of special significance for producing free hanging parts. For example, the collimation lens of the beam shaping unit is realized layer by layer in a bottom up approach. In the early stage of fabrication, the lens is not connected to the scaffold and therewith not fixated. Roughly speaking, it floats inside the liquid photoresist material. As a consequence, a high viscosity of the photoresist is desirable in fabrication to suppress a floating of the freely hanging structures. Hence, the beam shaping unit was realized by IP-S photoresist in a first step. However, after fabrication only a poor quality of the beam shaping unit was examined. Although, the vibrations of the fiber were significantly suppressed during the writing process, the measured

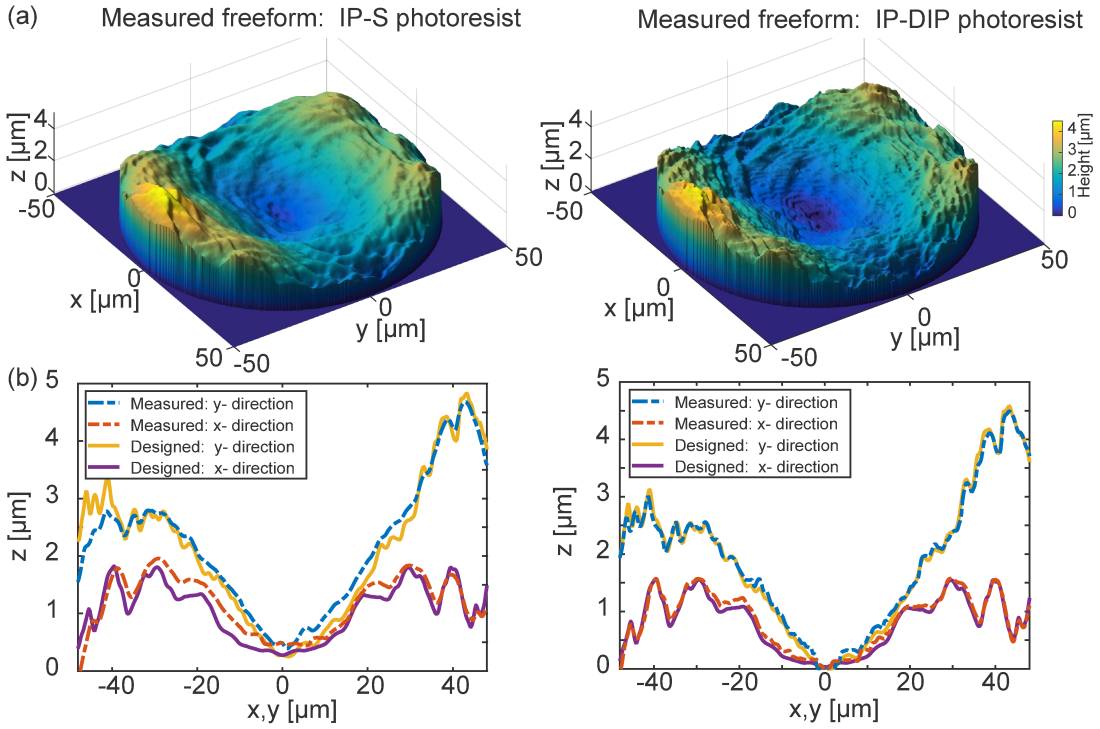

Figure 5.9: (a) Topography measurements of realized freeform hologram by different photoresist materials. (b) Direct comparison between a measured and designed freeform hologram along the coordinate axis, i.e., $z(x = 0, y)$, $z(x, y = 0)$.

focal field profile was inaccurate. To resolve the origin of these disturbances, the topography of the freeform hologram was measured. This revealed a significant blurring of the freeform hologram (see Fig. 5.9). While IP-S photoresist provides a high viscosity, the overall resolution of finest structure details is lowered and not accurate enough in the considered case. Alternatively, IP-DIP photoresist is optimized for highest resolution and shape accuracy. However, the viscosity is reduced and the realization of three-dimensional structures is more burdensome. To assess this photoresist for the fabrication of the beam shaping unit, the freeform hologram was realized on a substrate and inspected by a topographic measurement. In this case, additional influences due to a vibrating fiber are excluded. While this enables the assessment of an attainable accuracy, it slightly diminishes the comparability to the previous results with IP-S photoresist, where the freeform hologram was realized on the fiber tip. Nevertheless, connected deviations are expected to be small. Using IP-DIP as a photoresist provides a significant improvement in the realized accuracy of the freeform hologram. This aspect is even evident by visually comparing the measured surface profiles in the individual realizations in Fig. 5.9 (a). Clearly, the realization with IP-S as a photoresist material appears with a smoothened surface profile. To qualitatively assess this issue in more detail, Fig. 5.9 (b) shows the measured surface sag along the coordinate axis, i.e., $z(x = 0, y),\ z(x, y = 0)$, in comparison to the designed one. While IP-DIP can resolve also finest feature details in the designed freeform hologram, IP-S is less accurate.
As a consequence, the high-resolution IP-DIP photoresist needs to be used to realize the freeform hologram with a sufficient accuracy. However, the realization of freely hanging structures is more complicated in this case. To resolve this issue, one could modify the writing path generation of the optical 3d-printing process. Instead of a layered fabrication of the final micro-optical device, one should ensure a solid connection of freely hanging parts with the scaffold. In the considered example, the manufacturing of the collimation lens should start from the scaffold and subsequently approach the inner surface parts. However, this requires profound modifications of the software delivered with the commercial Nanoscribe Photonic Professional GT device. Alternatively, the beam shaping unit excluding the actual freeform hologram could be realized by IP-S photoresist. In an additional step, IP-DIP is used to realize the beam shaping surface. As a consequence, the entire device cannot be fabricated in a single manufacturing step. Alternatively, a modification of the optical design is considered in the following, where any free hanging parts are avoided.

5.2.3 Integrated beam shaping of complex focal field distributions

In the following section, the modified integrated beam shaping approach is discussed, which finally enabled to prove the conceptual idea. To this end, the design of the beam shaping unit needed to be adjusted to meet the modified requirements of using IP-DIP as a photoresist. In particular, any freely hanging parts should be removed. To this end, an entirely solid mechanical design was considered. Instead of a scaffold to mount the freeform hologram, a solid cylinder was taken into account. As a consequence, the divergence angle of the diffracting initial fiber mode inside the cylinder characterized by the refractive index of IP-DIP photoresist is lowered in comparison to free space. Hence, the cylinder has an increased height in comparison to the original design (see also Fig. 5.10). Moreover, the collimation lens prior to the freeform

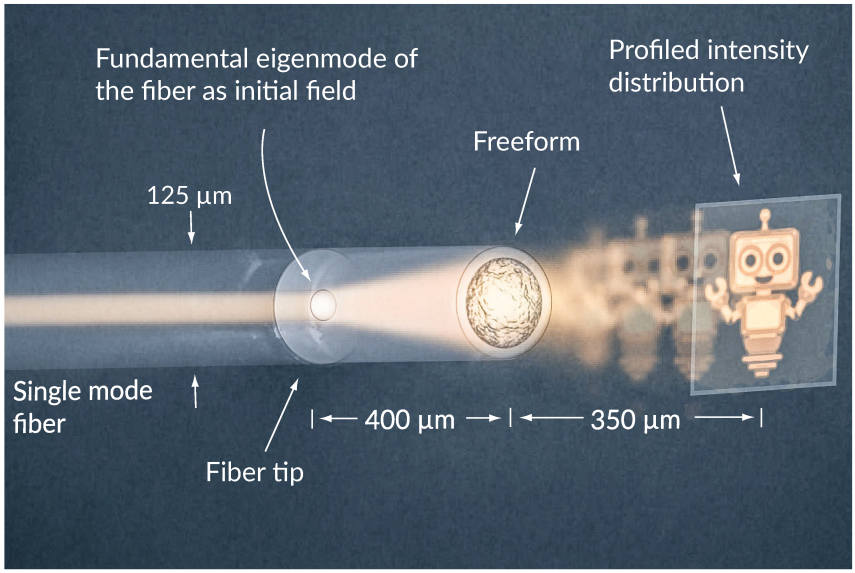

Figure 5.10: Schematic sketch of the integrated beam shaping setup: A freeform optical surface is imprinted onto a homogeneous cylinder on the tip of an optical fiber realized by femtosecond two-photon direct laser writing. The fundamental eigenmode of the fiber is used as initial field and inside the homogeneous cylinder the corresponding mode field diameter increases due to diffraction. This reduces alignment sensitivities and increases the resolution in the realized target intensity. The freeform profiles the phase of the incident beam and enables the redistribution of the field into the desired intensity. The diameter of the cylinder equals the fiber diameter of $D = 125\mu\text{m}$ with a height of $h = 400\mu\text{m}$. The distance between the freeform and the target plane equals approximately $z_{\text{Target}} \approx 350\mu\text{m}$.

hologram is removed. Hence, the incident beam is characterized by an initial spherical phase. Simulations of this modified scenario revealed, that in this case the realized target intensity gets magnified and shifted along the optical axis. Nevertheless, there is no significant qualitative degradation of the target intensity. As an advantage, the assessment of the magnified focal field profile by a microscopic measurement simplifies in this case, e.g., a reduced numerical aperture of the objective lens could be used.
This modified beam shaping unit was realized by optical 3d-printing. On the one hand, the freeform hologram with an approximate height of $\Delta z \approx 4$ µm is realized in a few minutes. On the other hand, the 400 µm long cylinder can take up to 5 hours. This part could potentially be replaced by a glass cylinder, e.g., a no core fiber, which could be spliced onto the existing fiber [173]. This approach could accelerate the fabrication process significantly.

To evaluate the realized beam shaping unit, the surface topography of the freeform hologram is again evaluated by a confocal surface measurement in a first step (see Fig. 5.11). The realized freeform hologram is in excellent agreement to the designed one. By comparing to the previous realization on the substrate (see Fig. 5.9) the current result appears even improved. In particular, along the coordinate axis deviations between measured and designed freeform hologram seem to be slightly reduced. To quantitatively judge the quality of the realized freeform hologram, a relative RMS error of the surface $\text{RMS} = \sqrt{\frac{\int_R |z_{\text{Meas}}(x,y) - z_{\text{Design}}(x,y)|^2 dx\, dy}{\int_R dx\, dy}}$ is examined. A value of RMS $\approx$ 60nm was achieved. This corresponds to a minor wavefront error of approximately $\frac{\lambda}{20}$ for the considered wavelength of $\lambda = 0.63\mu\text{m}$.

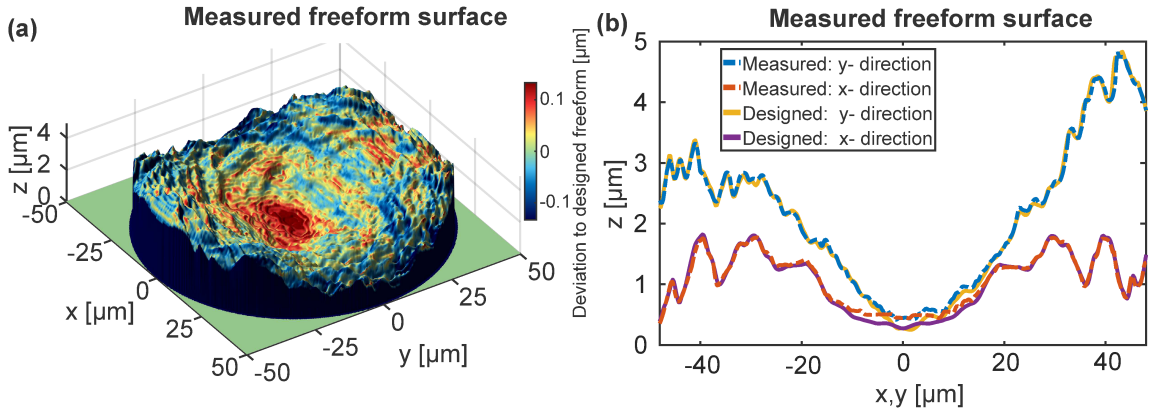

Figure 5.11: (a) The measured freeform is evaluated, where the measured surface sag is shown as the height profile overlaid with the color coded deviation to the designed surface sag. (b) Direct comparison between a measured and designed freeform along the coordinate axis, i.e., $z(x = 0, y)$, $z(x, y = 0)$.

In a next step, simulations with the wave propagation method of the measured surface are performed to predict the performance of the beam shaping unit. Thereby, the spectral characteristics of the illumination are considered. To this end, individual simulations at varying wavelengths weighted by the spectrum are added incoherently. In particular, a fiber coupled LED (Thorlabs M625F2) with a spectral bandwidth of $\Delta\lambda \approx 15$nm was used as the light source within the measurements and is evaluated here[3]. A comparison of the simulations for the ideal and measured freeform hologram is shown in Fig. 5.12 (a),(c). Even the small dots, e.g., at the wrist of the robot image, are resolved, which indicates the high accuracy of the manufactured freeform. In a final step, the target intensity was measured using a microscope setup consisting of a 50x/NA 0.55 Mitutoyo microscope lens, a tube system and a camera (IDS UI-3180CP-C-HQ). The corresponding result is shown in Fig. 5.12 (d). There is no zeroth order stray light apparent in the measurement. This is realized in conventional setups as an intensity peak on the optical axis, i.e., the coordinate origin $(x, y) = (0, 0)$. Moreover, there are no ghost images and no speckle effects in a measured intensity. However, a linear gradient of intensity is recognized. This is explained by a decentering of the Gaussian like field at the position of the freeform hologram with respect to the center of surface (see Fig. 5.12 (b)). This might be caused by a non-ideal cleave of the fiber tip, a tilt of the imprinted cylinder relative to the fiber or a decentered alignment. This changes the optical axis of the beam and causes a decentering on the freeform hologram. This issue could be resolved by an improved cleaving of the fiber or a more accurate alignment. Then, the origin of the surface needs a proper alignment to the center of the incident field. This could be realized, by a monitoring of the field during the manufacturing process. Currently, this adjustment procedure was only applied prior to the manufacturing process and was not refined during fabrication. At this stage, a digital adaptation of the measured intensity is considered by virtually applying a gradual intensity filter, i.e., the multiplication

[3] A measured spectrum of the LED is found in the specifications of the vendor. This spectral distribution was used as weighting for the incoherent summation of individual simulations.

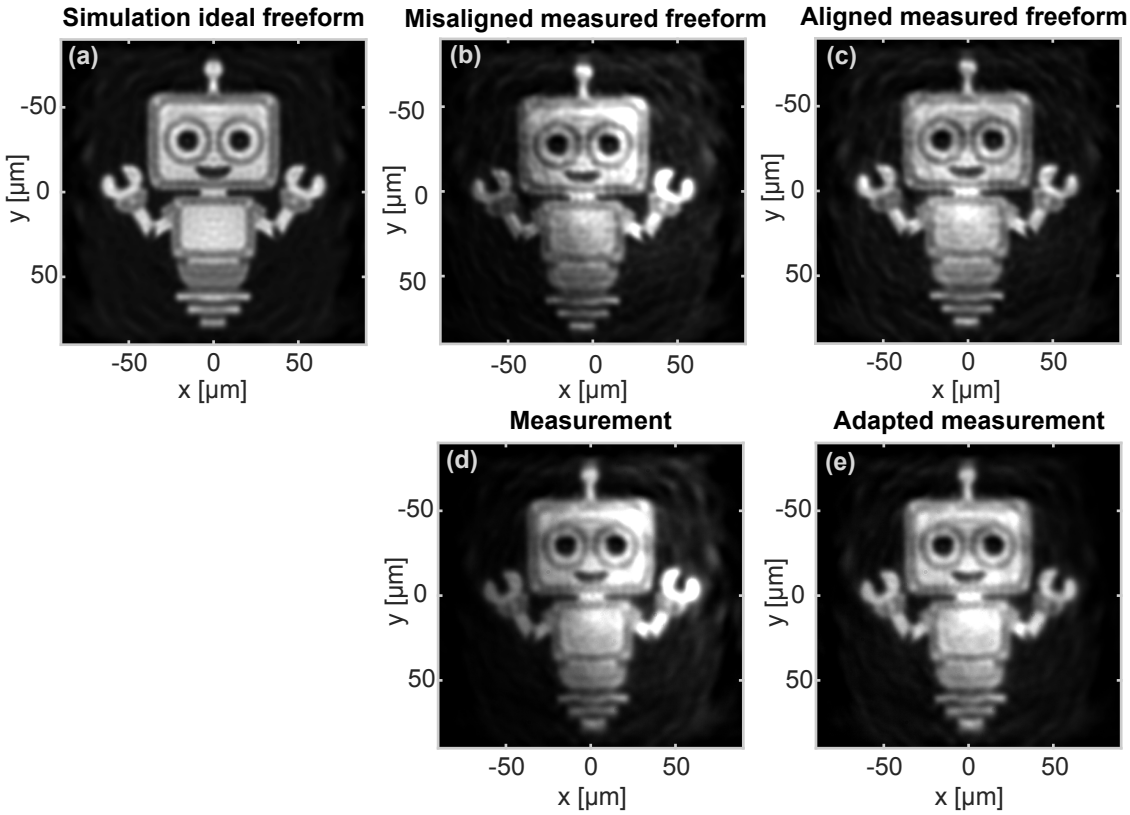

Figure 5.12: (a)-(c) Simulation of the designed and measured freeform with the wave propagation method. Individual simulations for different wavelengths are added incoherently to consider the spectral bandwidth $\Delta\lambda \approx 15$nm of the illumination source (Thorlabs LED M625F2). In subfigures (a), (c) a perfectly centered initial field is assumed. In subfigure (b) a decentering of the initial field of approximately 4.5µm with respect to the origin of the freeform hologram is considered. (d) Microscopic measurement of the profiled intensity distribution in the target plane of the realized beam shaping unit. (e) To enhance the visibility of the measured intensity, the recorded image was modified by a graduated intensity filter, which corresponds to the multiplication by a linear function. (a)-(e) The images are normalized by the total encircled power and share the same colormap.

of the measured intensity with a properly aligned linear function. This enhances the visibility of smallest realized feature details in the focal field distribution and improves the assessment. These results are shown in Fig. 5.12 (d). Again, the individual dots of the robot image are resolved, which underlines the accuracy of the approach. The measured intensity pattern visually even appears with an improved accuracy compared to the simulated results in Fig. 5.12 (c). This aspect might be explained by errors of the topography measurements, which lead to an increased deviation between the measured and designed surface, which, of course, influences the simulations.

5.3 Summary

In this chapter an integrated approach to realize complex illumination patterns in the focal region of an optical system was introduced. To this end, a freeform hologram was realized on the tip of an optical fiber, which enables the redistribution of the initial fundamental eigenmode

of the fiber into a custom focal field distribution. Within the approach straylight and speckle effects are significantly suppressed in the final target field distribution. This is achieved by a tailored design procedure, which results in a continuous and smooth surface profile. In an early optimization stage only coarse surface features are adapted and within subsequent optimization iterations also finer details are adjusted. This leads to a smooth convergence of the algorithm and reduced local surface gradients. Moreover, additional manufacturing constraints can easily be considered within the design process. The resulting surface profiles were realized by femtosecond two-photon direct laser writing. Fabricated beam shaping units were assessed by topographic measurements of realized freeform holograms and microscopic measurements of focal field distributions. Based on these evaluations, different parameters for the manufacturing process were optimized, which allowed to increase the resolution within the fabrication process. The final surface profiles showed a low figure error of approximately $\frac{\lambda}{20}$ in RMS deviation. Finally, microscopic measurements of the realized focal field profile verified the exceptional possibility to realize tailored field distributions in a highly integrated approach. This can pave the way for novel and unprecedented technological opportunities. In particular, the proposed approach might be utilized to use structured illumination in previously inaccessible domains. This is of particular importance in microscopy, material processing, optical trapping, and lab-on-a-chip devices.

Part IV

Conclusion and Outlook

Modern technological progress allows to manufacture micro-optical components with an unprecedented accuracy. In particular, femtosecond two-photon direct laser writing allows to realize true three-dimensional micro-optical structures without a coarse layering of the height profile [3]. This can significantly expand the possibilities that are feasible with conventional mask lithography. However, the possibility to take direct advantage out of these developments requires improved numerical simulation tools that can go beyond state-of-the-art modeling concepts in micro-optics. These enhanced modeling abilities are similarly needed for modern computational sensing concepts in holography, e.g., diffraction tomography. In these cases improved numerical models can expand the applicability of these measurement approaches [20, 27, 28].

It was the aim of this thesis to address these individual challenges and to develop extended numerical simulation concepts for the improved modeling of micro-optical structures. In addition, it was a second aim of this thesis to also discuss the practical potential of these improved simulation techniques for both the characterization and the design of micro-optical systems.
The individual algorithmic techniques for the improved modeling of micro-optical components were introduced in part II. Most importantly, a reformulated version of the wave propagation method for piecewise homogeneous media was discussed. Although the applicability is slightly limited since gradient index media can not directly be modeled, it, nevertheless, is valid in a majority of scenarios. It turned out, that this algorithm can outperform the different beam propagation methods for typical micro-optical scenarios as accurate simulations comparable to rigorous ones are achieved with an increased computational performance on even lower sampling densities. An additional improvement of the computational performance is achieved by exploiting additional underlying symmetries of the investigated structure. In particular, the algorithm was reformulated for an underlying rotational symmetry, which, then, is ideally suited for the description of e.g. micro-optical lenses. Consequently, this so-called Hankel-WPM was assessed for the evaluation of diffractive lenses. By comparing to rigorous simulations, it turned out that the Hankel-WPM can accurately model these diffractive lenses. Steep edges in the surface sag induce diffractive influences, which are not predicted by the TEA and cause diffractive false light. These insights were used later within the design process of the freeform holograms in order to overcome apparent limitations of conventional diffractive optical elements.
Future work, could concentrate on a further time improvement of the algorithms. The major computational effort of the reformulated WPM algorithm is connected to the application of fast Fourier transforms. Alternatively, for the Hankel-WPM the application of the fast Fourier transforms turns into matrix multiplications for the numerical evaluation of Hankel transforms. These individual computational steps can be parallelized. This suggests to use graphical processing units for these computations as they provide superior performance characteristics for parallel computing problems.

Overall, these numerical simulation tools enable the improved modeling of micro-optical components. This can open up novel abilities in their understanding, characterization and design. These aspects were discussed in part III of this thesis. The individual investigated scenarios in chapters 3-5 are highly diverse and include the metrological assessment of fibers, an integrated illumination concept and the assessment of the experimental inscription setup of fiber Bragg gratings (FBGs). The latter one was discussed in chapter 3, where glass matrix distortions

were discussed that might occur during the inscription. The origin of these glass defects was revealed by numerically modeling the experimental setup to realize the FBGs and by comparing these simulations to microscopic measurements of inscribed fibers. In particular, the distortions are caused by reflections at the rear surface of the fiber and spherical aberrations, which are induced by the cladding surface. In particular, these aberrations cause a field enhancement inside the fiber, which is the origin of the glass matrix distortions. Based on these insights, a possible solution strategy was developed. By embedding the actual fiber in a carefully tailored capillary with a higher index, the parasitic glass matrix distortions can be suppressed. However, this conceptual idea has not been realized and should be viewed as a potential outlook to this thesis.

Chapter 4 focused on the development of a non-invasive characterization technique of optical fibers, which potentially is suitable to be integrated into the fabrication process of optical fibers. In particular, an in-line holographic measurement principle was considered. To this end, the investigated fiber was side-illuminated by a coherent beam and the diffraction response was measured on a distant screen. By simulating the entire setup and by varying the structural parameters of the fiber in the simulations an optimal match with the measurements was examined. In a first step, the potential of this measurement idea was assessed. It turns out, that the wave propagation method can simulate this challenging scenario and enables a parameter retrieval in principle. Nevertheless, the signature of the inner structural composition of the fiber was weak in the measured signals and the parameter retrieval was challenging. In a second step, the limiting aspects of the original setup were analyzed and an improved setup was proposed. This refined setup allows to characterize the inner structural composition of the fiber more accurate. In particular, capillary fibers with capillary hole diameters in the deep micrometer range have been analyzed. These hole diameters were retrieved with a high accuracy of up to 100 nm. However, at the current stage only a proof-of-principle evaluation has been performed. In the future, the ability of the methodology to assess different fiber types should be investigated. For instance, the possibility to characterize photonic crystal fibers seems interesting. Their internal structural composition is more complex and thus the numerical assessment will be more challenging. Moreover, the setup needs to be further refined, to also use it in the harsh environment of a fabrication process. Especially the illumination should be improved. Currently, a single mode fiber placed in close vicinity to the investigated fiber is used as initial light source. Alternatively, a refined illumination unit should be designed to increase the distance between the source and the investigated fiber. Moreover, the influence of the temporal coherence of the initial light source should be investigated. In particular, it was suggested that the temporal coherence influences the appearance of local minima in the parameter retrieval process. Avoiding their appearance, would simplify the assessment of fibers.

Finally, in chapter 5 an integrated beam shaping concept was introduced. In particular, a freeform surface was realized on the tip of an optical fiber, which redistributes the initial fundamental eigenmode of the fiber into a desired target field distribution. This approach allows for a high degree of miniaturization. Additionally, it has the potential to overcome apparent restrictions of conventional diffractive beam shaping approaches. In particular, the proposed approach entirely suppresses parasitic false light, which otherwise is seen as a strong zeroth order peak

or as ghost images in realized intensity distributions. This strongly increases the diffraction efficiency and is achieved by a novel design methodology, which results in a continuous surface profile without steep edges and reduced surface gradients. These so-called freeform holograms were fabricated by two-photon direct laser writing, which allows to realize these surface profiles with a highest as build quality and without a coarse layering of the surface sag profile. To assess the manufactured beam shaping unit, topographic measurements of the fabricated surface profile and measurements of the realized focal intensity field distribution were evaluated. These measurements verified the exceptional quality of the beam shaping unit as a minor RMS-error of $\frac{\lambda}{20}$ for the surface profile and a high quality in the realized intensity profile were achieved. However, the methodology was currently only assessed as a proof-of-principle concept and there is space for improvement. From a design point of view it seems promising to include additional constraints from the manufacturing process within the optimization process. Currently, only the surface gradients were restricted due to the filtering process. However, one could additionally consider surface curvatures or certain random noise errors to mimic environmental disturbances. However, these additional refinements need to be founded on a deeper knowledge about the manufacturing process and its limitations. This requires profound additional investigations. Moreover, also from a manufacturing point of view there is potential to improve and accelerate the fabrication process. In particular, the realization could be improved by avoiding decentration errors between the freeform hologram and the incident initial field. Then, the origin of the surface needs a proper alignment to the center of the incident field, which could be realized by a monitoring of the field during fabrication. Moreover, the manufacturing process will be strongly accelerated if the homogeneous cylinder needs not to be imprinted by two-photon direct laser writing. Alternatively, one could splice end-caps onto the single mode fibers, which are state-of-the-art concepts for modern fiber laser systems. In addition, the replication and reproduction of freeform holograms should be investigated as this will be an essential aspect for the suitability of the approach in commercial application scenarios.

Finally, the most interesting future development might be the adaptation of the approach to novel applications. Overall, there are three major advantages: *(i)* A high degree of miniaturization; *(ii)* a high mechanical flexibility, i.e., equivalent to the mechanical properties of the fiber; *(iii)* high diffraction efficiencies and a high quality of realized field distributions. In particular, these advantages can open up novel possibilities in all scenarios, where structured illumination is used. For instance, this allows to use tailored field distributions in previously inaccessible domains and this approach could be used to merge structured illumination with endoscopy. This can open up improved resolutions in endoscopic imaging within the framework of ptychography or structured light microscopy. Moreover, the mechanical flexibility might be used to realize improved complex optical traps, which can easily be moved and adapted to varying experimental conditions. Finally, the approach might be utilized as the worlds smallest projection unit, for instance, to display the Batman logo, brighter than ever before, into the sky of Gotham city to save it from the forces of evil.

Bibliography

[1] L. Novotny and B. Hecht, *Principles of Nano-Optics* (Cambridge University Press, 2012).

[2] N. Yu and F. Capasso, "Flat optics with designer metasurfaces," Nat. Mater. **13**, 139 (2014).

[3] M. Malinauskas, A. Žukauskas, S. Hasegawa, Y. Hayasaki, V. Mizeikis, R. Buividas, and S. Juodkazis, "Ultrafast laser processing of materials: from science to industry," Light-Sci. Appl. **5**, e16133 (2016).

[4] F. Fang, X. Zhang, A. Weckenmann, G. Zhang, and C. Evans, "Manufacturing and measurement of freeform optics," CIRP Annals **62**, 823 (2013).

[5] N. Antipa, G. Kuo, R. Heckel, B. Mildenhall, E. Bostan, R. Ng, and L. Waller, "DiffuserCam: lensless single-exposure 3d imaging," Optica **5**, 1 (2017).

[6] G. Kim, K. Isaacson, R. Palmer, and R. Menon, "Lensless photography with only an image sensor," Appl. Opt. **56**, 6450 (2017).

[7] A. Sinha, J. Lee, S. Li, and G. Barbastathis, "Lensless computational imaging through deep learning," Optica **4**, 1117 (2017).

[8] M. Plöschner, T. Tyc, and T. Čižmár, "Seeing through chaos in multimode fibres," Nat. Photonics **9**, 529 (2015).

[9] T. Čižmár and K. Dholakia, "Exploiting multimode waveguides for pure fibre-based imaging," Nat. Commun. **3** (2012).

[10] A. P. Mosk, A. Lagendijk, G. Lerosey, and M. Fink, "Controlling waves in space and time for imaging and focusing in complex media," Nat. Photonics **6**, 283–292 (2012).

[11] I. M. Vellekoop and A. P. Mosk, "Focusing coherent light through opaque strongly scattering media," Opt. Lett. **32**, 2309 (2007).

[12] A. Liutkus, D. Martina, S. Popoff, G. Chardon, O. Katz, G. Lerosey, S. Gigan, L. Daudet, and I. Carron, "Imaging with nature: Compressive imaging using a multiply scattering medium," Sci. Rep. **4** (2014).

[13] O. Katz, P. Heidmann, M. Fink, and S. Gigan, "Non-invasive single-shot imaging through scattering layers and around corners via speckle correlations," Nat. Photonics **8**, 784 (2014).

[14] H.-Y. Liu, E. Jonas, L. Tian, J. Zhong, B. Recht, and L. Waller, "3d imaging in volumetric scattering media using phase-space measurements," Opt. Express **23**, 14461 (2015).

[15] W. Harm, C. Roider, A. Jesacher, S. Bernet, and M. Ritsch-Marte, "Lensless imaging through thin diffusive media," Opt. Express **22**, 22146 (2014).

[16] M. G. Gustafsson, "Nonlinear structured-illumination microscopy: wide-field fluorescence imaging with theoretically unlimited resolution," Proc. Natl. Acad. Sci. U.S.A. **102**, 13081 (2005).

[17] R. Heintzmann, T. M. Jovin, and C. Cremer, "Saturated patterned excitation microscopy—a concept for optical resolution improvement," J. Opt. Soc. Am. A **19**, 1599 (2002).

[18] E. Betzig, G. H. Patterson, R. Sougrat, O. W. Lindwasser, S. Olenych, J. S. Bonifacino, M. W. Davidson, J. Lippincott-Schwartz, and H. F. Hess, "Imaging intracellular fluorescent proteins at nanometer resolution," Science **313**, 1642 (2006).

[19] S. A. Benton and V. M. B. Jr., *Holographic Imaging* (Wiley-Interscience, 2008).

[20] U. S. Kamilov, I. N. Papadopoulos, M. H. Shoreh, A. Goy, C. Vonesch, M. Unser, and D. Psaltis, "Learning approach to optical tomography," Optica **2**, 517 (2015).

[21] P. S. Huang, "High-resolution, real-time three-dimensional shape measurement," Opt. Eng. **45**, 123601 (2006).

[22] G. B. Baer, J. Schindler, C. Pruss, and W. Osten, "Measurement of aspheres and free-form surfaces with the tilted-wave-interferometer," in "Fringe 2013," (Springer, 2014), pp. 87–95.

[23] A. Junker and K.-H. Brenner, "Achieving a high mode count in the exact electromagnetic simulation of diffractive optical elements," J. Opt. Soc. Am. A **35**, 377 (2018).

[24] T. Habisreuther, T. Elsmann, Z. Pan, A. Graf, R. Willsch, and M. A. Schmidt, "Sapphire fiber bragg gratings for high temperature and dynamic temperature diagnostics," Appl. Therm. Eng. **91**, 860 (2015).

[25] R. B. Jenkins, P. Joyce, and D. Mechtel, "Localized temperature variations in laser-irradiated composites with embedded fiber bragg grating sensors," Sensors **17**, 251 (2017).

[26] J. Ayers, T. Weerasooriya, A. Ghoshal, C. Pecora, A. Gunnarsson, B. Sanborn, and P. Turney, "Feasibility of component state awareness of high strain rate events using fiber bragg grating sensors," Int. J. Impact Eng. **100**, 166 (2017).

[27] X. Ma, W. Xiao, and F. Pan, "Optical tomographic reconstruction based on multi-slice wave propagation method," Opt. Express **25**, 22595 (2017).

[28] J. Lim, A. Wahab, G. Park, K. Lee, Y. Park, and J. C. Ye, "Beyond born-rytov limit for super-resolution optical diffraction tomography," Opt. Express **25**, 30445 (2017).

[29] A. Taflove and S. C. Hagness, *Computational electrodynamics: the finite-difference time-domain method* (Artech house, 2005).

[30] D. Ploss, A. Kriesch, H. Pfeifer, P. Banzer, and U. Peschel, "Generation and subwavelength focusing of longitudinal magnetic fields in a metallized fiber tip," Opt. Express **22**, 13744 (2014).

[31] M. Paulus and O. J. F. Martin, "Green's tensor technique for scattering in two-dimensional stratified media," Phys. Rev. E **63**, 066615 (2001).

[32] W. Shin and S. Fan, "Accelerated solution of the frequency-domain maxwell's equations by engineering the eigenvalue distribution of the operator," Opt. Express **21**, 22578 (2013).

[33] V. A. Soifer, *Diffractive Nanophotonics* (CRC Press, 2014).

[34] S. Mühlig and C. Rockstuhl, "Multipole analysis of self-assembled metamaterials," in "Amorphous Nanophotonics," (Springer Berlin Heidelberg, 2013), pp. 89–117.

[35] M. Decker, I. Staude, M. Falkner, J. Dominguez, D. N. Neshev, I. Brener, T. Pertsch, and Y. S. Kivshar, "High-efficiency dielectric huygens' surfaces," Advanced Optical Materials **3**, 813–820 (2015).

[36] B. D. Stone and G. Forbes, "Differential ray tracing in inhomogeneous media," J. Opt. Soc. Am. A **14**, 2824 (1997).

[37] O. Stolz, "Differentielles raytracing für spezielle beleuchtungssysteme," Ph.D. thesis, Friedrich-Alexander-Universität Erlangen-Nürnberg (2010).

[38] M. Mout, M. Wick, F. Bociort, J. Petschulat, and P. Urbach, "Simulating multiple diffraction in imaging systems using a path integration method," Appl. Opt. **55**, 3847 (2016).

[39] J. B. Keller, "Geometrical theory of diffraction," J. Opt. Soc. Am. A **52**, 116 (1962).

[40] J. D. Jackson, *Classical electrodynamics* (John Wiley & Sons, 2007).

[41] M. Born and E. Wolf, *Principles of optics: electromagnetic theory of propagation, interference and diffraction of light* (Elsevier, 2013).

[42] M. C. Teich and B. Saleh, "Fundamentals of photonics," Wiley Interscience (1991).

[43] J. Bures, *Guided optics* (John Wiley & Sons, 2009).

[44] E. Arbabi, A. Arbabi, S. M. Kamali, Y. Horie, and A. Faraon, "Controlling the sign of chromatic dispersion in diffractive optics with dielectric metasurfaces," Optica **4**, 625 (2017).

[45] D. Yevick, "A guide to electric field propagation techniques for guided-wave optics," Opt. Quant. Electron. **26**, 185 (1994).

[46] M. Kolesik and J. V. Moloney, "Nonlinear optical pulse propagation simulation: From maxwell's to unidirectional equations," Phys. Rev. E **70**, 036604 (2004).

[47] M. R. Teague, "Deterministic phase retrieval: a green's function solution," J. Opt. Soc. Am. A **73**, 1434 (1983).

[48] G. R. Hadley, "Wide-angle beam propagation using padé approximant operators," Opt. Lett. **17**, 1426 (1992).

[49] H. Lajunen, J. Tervo, J. Turunen, T. Vallius, and F. Wyrowski, "Simulation of light propagation by local spherical interface approximation," Appl. Opt. **42**, 6804 (2003).

[50] A. v. Pfeil, F. Wyrowski, A. Drauschke, and H. Aagedal, "Analysis of optical elements with the local plane-interface approximation," Appl. Opt. **39**, 3304 (2000).

[51] N. Lindlein and J. Schwider, "Local wave fronts at diffractive elements," J. Opt. Soc. Am. A **10**, 2563 (1993).

[52] N. Lindlein and H. P. Herzig, "Design and modeling of a miniature system containing micro-optics," in "Gradient Index, Miniature, and Diffractive Optical Systems II," T. J. Suleski, ed. (SPIE, 2001).

[53] J. R. Fienup, "Phase retrieval algorithms: a comparison," Appl. Opt. **21**, 2758 (1982).

[54] G. R. Hadley, "Multistep method for wide-angle beam propagation," Opt. Lett. **17**, 1743 (1992).

[55] M. Feit and J. Fleck, "Light propagation in graded-index optical fibers," Appl. Opt. **17**, 3990 (1978).

[56] Y. Chung and N. Dagli, "An assessment of finite difference beam propagation method," IEEE J. Quantum Electron. **26**, 1335 (1990).

[57] K. Kawano and T. Kitoh, *Introduction to Optical Waveguide Analysis* (John Wiley & Sons, Inc., 2001).

[58] "https://optiwave.com/category/optibpm-manuals/optibpm-tutorials/2-bpm-technical-background/," (2017).

[59] W. H. Press, *Numerical recipes 3rd edition: The art of scientific computing* (Cambridge university press, 2007).

[60] D. Yevick and B. Hermansson, "New formulations of the matrix beam propagation method: Application to rib waveguides," IEEE J. Quantum Electron. **25**, 221 (1989).

[61] G. R. Hadley, "Transparent boundary condition for beam propagation," Opt. Lett. **16**, 624 (1991).

[62] G. R. Hadley, "Transparent boundary condition for the beam propagation method," IEEE J. Quantum Electron. **28**, 363 (1992).

[63] J.-P. Berenger, "A perfectly matched layer for the absorption of electromagnetic waves," J. Comput. Phys. **114**, 185 (1994).

[64] G. R. Hadley and R. Smith, "Full-vector waveguide modeling using an iterative finite-difference method with transparent boundary conditions," IEEE J. of Lightwave Techn. **13**, 465 (1995).

[65] E. Bekker, P. Sewell, T. Benson, and A. Vukovic, "Wide-angle alternating-direction implicit finite-difference beam propagation method," IEEE J. Lightwave Techn. **27**, 2595 (2009).

[66] R. Ratowsky and J. Fleck, "Accurate numerical solution of the helmholtz equation by iterative lanczos reduction," Opt. Lett. **16**, 787 (1991).

[67] J. Shibayama, T. Takahashi, J. Yamauchi, and H. Nakano, "A three-dimensional horizontally wide-angle noniterative beam-propagation method based on the alternating-direction implicit scheme," IEEE Photon. Technol. Lett. **18**, 661 (2006).

[68] J. Shibayama, T. Takahashi, J. Yamauchi, and H. Nakano, "A three-dimensional multistep horizontally wide-angle beam-propagation method based on the generalized douglas scheme," IEEE Photon. Technol. Lett. **18**, 2535 (2006).

[69] C. Ma and E. Van Keuren, "A simple three dimensional wide-angle beam propagation method," Opt. Express **14**, 4668 (2006).

[70] S. H. Wei and Y. Y. Lu, "Application of bi-cgstab to waveguide discontinuity problems," IEEE Photon. Technol. Lett. **14**, 645 (2002).

[71] K.-H. Brenner and W. Singer, "Light propagation through microlenses: a new simulation method," Appl. Opt. **32**, 4984 (1993).

[72] W. Singer, M. Testorf, and K.-H. Brenner, "Gradient-index microlenses: numerical investigation of different spherical index profiles with the wave propagation method," Appl. Opt. **34**, 2165 (1995).

[73] M. Fertig and K.-H. Brenner, "Vector wave propagation method," J. Opt. Soc. Am. A **27**, 709 (2010).

[74] A. S. Rodriguez, "Evaluation of the trustworthiness of different beam propagation methods," Master's thesis, Abbe School of Photonics - Research Lab report (2015).

[75] S. Schmidt, T. Tiess, S. Schröter, R. Hambach, M. Jäger, H. Bartelt, A. Tünnermann, and H. Gross, "Wave-optical modeling beyond the thin-element-approximation," Opt. Express **24**, 30188 (2016).

[76] S. Schmidt, S. Thiele, A. Herkommer, A. Tünnermann, and H. Gross, "Rotationally symmetric formulation of the wave propagation method-application to the straylight analysis of diffractive lenses," Opt. Lett. **42**, 1612 (2017).

[77] L. Hörmander, *The analysis of linear partial differential operators iii* (Springer, 1980).

[78] M. V. de Hoop, J. H. Le Rousseau, and R.-S. Wu, "Generalization of the phase-screen approximation for the scattering of acoustic waves," Wave Motion **31**, 43 (2000).

[79] T. Op't Root and C. Stolk, "One-way wave propagation with amplitude based on pseudo-differential operators," Wave Motion **47**, 67 (2010).

[80] Y. M. Altman, *Accelerating MATLAB Performance: 1001 tips to speed up MATLAB programs* (CRC Press, 2014).

[81] D. Faklis and G. M. Morris, "Spectral properties of multiorder diffractive lenses," Appl. Opt. **34**, 2462 (1995).

[82] W. Huang and C. Xu, "Simulation of three-dimensional optical waveguides by a full-vector beam propagation method," IEEE J. Quantum Electron. **29**, 2639 (1993).

[83] J. Lim, T. Benson, E. Larkins, and P. Sewell, "Wideband finite-difference–time-domain beam propagation method," Microwave Opt. Technol. Lett. **34**, 243 (2002).

[84] H. Johnson, "An improved method for computing a discrete Hankel transform," Comput. Phys. Commun. **43**, 181 (1987).

[85] M. Guizar-Sicairos and J. C. Gutiérrez-Vega, "Computation of quasi-discrete Hankel transforms of integer order for propagating optical wave fields," J. Opt. Soc. Am. A **21**, 53 (2004).

[86] D. Lemoine, "The discrete Bessel transform algorithm," J. Chem. Phys **101**, 3936 (1994).

[87] A. W. Norfolk and E. J. Grace, "Reconstruction of optical fields with the quasi-discrete Hankel transform," Opt. Express **18**, 10551 (2010).

[88] N. Baddour and U. Chouinard, "Theory and operational rules for the discrete Hankel transform," J. Opt. Soc. Am. A **32**, 611 (2015).

[89] S. Thiele, T. Gissibl, H. Giessen, and A. M. Herkommer, "Ultra-compact on-chip LED collimation optics by 3D femtosecond direct laser writing," Opt. Lett. **41**, 3029 (2016).

[90] T. Gissibl, S. Thiele, A. Herkommer, and H. Giessen, "Sub-micrometre accurate free-form optics by three-dimensional printing on single-mode fibres," Nat. Commun. **7**, 11763 (2016).

[91] A. Koshelev, G. Calafiore, C. Piña-Hernandez, F. I. Allen, S. Dhuey, S. Sassolini, E. Wong, P. Lum, K. Munechika, and S. Cabrini, "High refractive index fresnel lens on a fiber fabricated by nanoimprint lithography for immersion applications," Opt. Lett. **41**, 3423 (2016).

[92] W. D. Furlan, V. Ferrando, J. A. Monsoriu, P. Zagrajek, E. Czerwińska, and M. Szustakowski, "3D printed diffractive terahertz lenses," Opt. Lett. **41**, 1748 (2016).

[93] T. Gissibl, M. Schmid, and H. Giessen, "Spatial beam intensity shaping using phase masks on single-mode optical fibers fabricated by femtosecond direct laser writing," Optica **3**, 448 (2016).

[94] G. Matz, B. Messerschmidt, and H. Gross, "Design and evaluation of new color-corrected rigid endomicroscopic high na grin-objectives with a sub-micron resolution and large field of view," Opt. Express **24**, 10987 (2016).

[95] D. Infante-Gómez and H. P. Herzig, "Design, simulation, and quality evaluation of micro-optical freeform beam shapers at different illumination conditions," Appl. Opt. **55**, 8340 (2016).

[96] M. Bawart, S. Bernet, and M. Ritsch-Marte, "Programmable freeform optical elements," Opt. Express **25**, 4898 (2017).

[97] V. A. Soifer, *Computer design of diffractive optics* (Elsevier, 2012).

[98] H. Gross, H. Zügge, M. Peschka, and F. Blechinger, *Handbook of Optical Systems* (Wiley-VCH Verlag GmbH & Co. KGaA, 2006).

[99] T. Ando, T. Korenaga, M.-a. Suzuki, and J. Tanida, "Diffraction light analysis method for a diffraction grating imaging lens," Appl. Opt. **53**, 2532 (2014).

[100] https://petapixel.com/2015/01/10/closer-look-nikons-new-phase-fresnel-pf-lens-technology/ .

[101] D. A. Buralli, G. M. Morris, and J. R. Rogers, "Optical performance of holographic kinoforms," Appl. Opt. **28**, 976 (1989).

[102] A. D. Kersey, M. A. Davis, H. J. Patrick, M. LeBlanc, K. Koo, C. Askins, M. Putnam, and E. J. Friebele, "Fiber grating sensors," IEEE J. of Lightwave Techn. **15**, 1442 (1997).

[103] K. O. Hill and G. Meltz, "Fiber bragg grating technology fundamentals and overview," IEEE J. of Lightwave Techn. **15**, 1263 (1997).

[104] G. P. Agrawal and S. Radic, "Phase-shifted fiber bragg gratings and their application for wavelength demultiplexing," IEEE Photon. Technol. Lett. **6**, 995 (1994).

[105] B. J. Eggleton, J. A. Rogers, P. S. Westbrook, and T. A. Strasser, "Electrically tunable power efficient dispersion compensating fiber bragg grating," IEEE Photon. Technol. Lett. **11**, 854 (1999).

[106] Z. Wei, H. Shalaby, and H. Ghafouri-Shiraz, "Modified quadratic congruence codes for fiber bragg-grating-based spectral-amplitude-coding optical cdma systems," IEEE J. of Lightwave Techn. **19**, 1274 (2001).

[107] G. Ball and W. Morey, "Compression-tuned single-frequency bragg grating fiber laser," Opt. Lett. **19**, 1979 (1994).

[108] T. Tiess, M. Becker, M. Rothhardt, H. Bartelt, and M. Jäger, "Discrete tuning concept for fiber-integrated lasers based on tailored fbg arrays and a theta cavity layout," Opt. Lett. **42**, 1125 (2017).

[109] H. G. Limberger, C. Ban, R. P. Salathé, S. A. Slattery, and D. N. Nikogosyan, "Absence of uv-induced stress in bragg gratings recorded by high-intensity 264 nm laser pulses in a hydrogenated standard telecom fiber," Opt. Express **15**, 5610 (2007).

[110] R. Buschlinger, S. Nolte, and U. Peschel, "Self-organized pattern formation in laser-induced multiphoton ionization," Phys. Rev. B **89**, 184306 (2014).

[111] S. D. Jackson, A. Sabella, A. Hemming, S. Bennetts, and D. G. Lancaster, "High-power 83 w holmium-doped silica fiber laser operating with high beam quality," Opt. Lett. **32**, 241 (2007).

[112] J. Limpert, T. Schreiber, S. Nolte, H. Zellmer, A. Tünnermann, R. Iliew, F. Lederer, J. Broeng, G. Vienne, A. Petersson, and C. Jakobsen, "High-power air-clad large-mode-area photonic crystal fiber laser," Opt. Express **11**, 818 (2003).

[113] J. Limpert, O. Schmidt, J. Rothhardt, F. Röser, T. Schreiber, A. Tünnermann, S. Ermeneux, P. Yvernault, and F. Salin, "Extended single-mode photonic crystal fiber lasers," Opt. Express **14**, 2715 (2006).

[114] O. Haeberlé, K. Belkebir, H. Giovaninni, and A. Sentenac, "Tomographic diffractive microscopy: basics, techniques and perspectives," J. Mod. Opt. **57**, 686 (2010).

[115] M. Debailleul, B. Simon, V. Georges, O. Haeberlé, and V. Lauer, "Holographic microscopy and diffractive microtomography of transparent samples," Meas. Sci. Technol. **19**, 074009 (2008).

[116] J. Kostencka, T. Kozacki, M. Dudek, and M. Kujawińska, "Noise suppressed optical diffraction tomography with autofocus correction," Opt. Express **22**, 5731 (2014).

[117] A. D. Yablon, "Multifocus tomographic algorithm for measuring optically thick specimens," Opt. Lett. **38**, 4393 (2013).

[118] W. Gorski and W. Osten, "Tomographic imaging of photonic crystal fibers," Opt. Lett. **32**, 1977 (2007).

[119] J. Kostencka, T. Kozacki, A. Kuś, and M. Kujawińska, "Accurate approach to capillary-supported optical diffraction tomography," Opt. Express **23**, 7908 (2015).

[120] A. C. Kak and M. Slaney, *Principles of computerized tomographic imaging* (SIAM, 2001).

[121] B. Chen and J. J. Stamnes, "Validity of diffraction tomography based on the first born and the first rytov approximations," Appl. Opt. **37**, 2996 (1998).

[122] C. Markos, "Photonic-crystal fibre: mapping the structure," Nat. Phot. **9**, 9 (2015).

[123] L. S. Watkins, "Scattering from side-illuminated clad glass fibers for determination of fiber parameters," J. Opt. Soc. Am. **64**, 767 (1974).

[124] F. Warken and H. Giessen, "Fast profile measurement of micrometer-sized tapered fibers with better than 50-nm accuracy," Opt. Lett. **29**, 1727 (2004).

[125] L. Zang, T. Euser, M. Kang, M. Scharrer, and P. S. J. Russell, "Structural analysis of photonic crystal fibers by side scattering of laser light," Opt. Lett. **36**, 1668 (2011).

[126] G. Świrniak, G. Głomb, and J. Mroczka, "Inverse analysis of light scattered at a small angle for characterization of a transparent dielectric fiber," Appl. Opt. **53**, 7103 (2014).

[127] G. Świrniak, G. Głomb, and J. Mroczka, "Inverse analysis of the rainbow for the case of low-coherent incident light to determine the diameter of a glass fiber," Appl. Opt. **53**, 4239 (2014).

[128] A. Stefani, M. H. Frosz, T. G. Euser, G. K. Wong, and P. S. J. Russell, "Real-time doppler-assisted tomography of microstructured fibers by side-scattering," Opt. Express **22**, 25570 (2014).

[129] S. Schmidt, T. Tiess, S. Schröter, A. Schwuchow, M. Jäger, H. Bartelt, A. Tünnermann, and H. Gross, "Noninvasive characterization of optical fibers," Opt. Lett. **42**, 4946 (2017).

[130] W. Xu, M. Jericho, I. Meinertzhagen, and H. Kreuzer, "Digital in-line holography for biological applications," Proceedings of the National Academy of Sciences **98**, 11301 (2001).

[131] J. Sheng, E. Malkiel, and J. Katz, "Digital holographic microscope for measuring three-dimensional particle distributions and motions," Appl. Opt. **45**, 3893 (2006).

[132] F. Shen and A. Wang, "Fast-fourier-transform based numerical integration method for the rayleigh-sommerfeld diffraction formula," Appl. Opt. **45**, 1102 (2006).

[133] D. Asoubar, S. Zhang, F. Wyrowski, and M. Kuhn, "Parabasal field decomposition and its application to non-paraxial propagation," Opt. Express **20**, 23502 (2012).

[134] A. Tuniz, M. Chemnitz, J. Dellith, S. Weidlich, and M. A. Schmidt, "Hybrid-mode-assisted long-distance excitation of short-range surface plasmons in a nanotip-enhanced step-index fiber," Nano Lett. **17**, 631 (2017).

[135] M. A. Schmidt, L. N. Prill Sempere, H. K. Tyagi, C. G. Poulton, and P. S. J. Russell, "Waveguiding and plasmon resonances in two-dimensional photonic lattices of gold and silver nanowires," Phys. Rev. B **77** (2008).

[136] S. Faez, Y. Lahini, S. Weidlich, R. F. Garmann, K. Wondraczek, M. Zeisberger, M. A. Schmidt, M. Orrit, and V. N. Manoharan, "Fast, label-free tracking of single viruses and weakly scattering nanoparticles in a nanofluidic optical fiber," ACS Nano **9**, 12349 (2015).

[137] M. Chemnitz, M. Gebhardt, C. Gaida, F. Stutzki, J. Kobelke, J. Limpert, A. Tünnermann, and M. A. Schmidt, "Hybrid soliton dynamics in liquid-core fibres." Nat. Commun. **8**, 42 (2017).

[138] B. Abaie, E. Mobini, S. Karbasi, T. Hawkins, J. Ballato, and A. Mafi, "Random lasing in an anderson localizing optical fiber," Light-Sci. Appl. **6**, e17041 (2017).

[139] E. Mobini, B. Abaie, M. Peysokhan, and A. Mafi, "Spectral selectivity in optical fiber capillary dye lasers," Opt. Lett. **42**, 1784 (2017).

[140] A. Fitt, K. Furusawa, T. Monro, C. Please, and D. Richardson, "The mathematical modelling of capillary drawing for holey fibre manufacture," J. Eng. Math. **43**, 201 (2002).

[141] L. Watkins, "Laser beam refraction traversely through a graded-index preform to determine refractive index ratio and gradient profile," Appl. Opt. **18**, 2214 (1979).

[142] M. Pasienski and B. DeMarco, "A high-accuracy algorithm for designing arbitrary holographic atom traps," Opt. Express **16**, 2176 (2008).

[143] R. Kowarschik, P. Ku, W. Schreiber, G. Notni *et al.*, "Adaptive optical three-dimensional measurement with structured light," Opt. Eng. **39**, 150 (2000).

[144] F. Chen, G. M. Brown, and M. Song, "Overview of three-dimensional shape measurement using optical methods," Opt. Eng. **39**, 10 (2000).

[145] J. M. Rodenburg, "Ptychography and related diffractive imaging methods," Adv. Imag. Electron Phys. **150**, 87 (2008).

[146] B.-C. Chen, W. R. Legant, K. Wang, L. Shao, D. E. Milkie, M. W. Davidson, C. Janetopoulos, X. S. Wu, J. A. Hammer, Z. Liu *et al.*, "Lattice light-sheet microscopy: imaging molecules to embryos at high spatiotemporal resolution," Science **346**, 1257998 (2014).

[147] C. Liberale, P. Minzioni, F. Bragheri, F. D. Angelis, E. D. Fabrizio, and I. Cristiani, "Miniaturized all-fibre probe for three-dimensional optical trapping and manipulation," Nat. Photonics **1**, 723 (2007).

[148] S. Juodkazis, "Manufacturing: 3d printed micro-optics," Nat. Photonics **10**, 499 (2016).

[149] I. T. Leite, S. Turtaev, X. Jiang, M. Šiler, A. Cuschieri, P. S. J. Russell, and T. Čižmár, "Three-dimensional holographic optical manipulation through a high-numerical-aperture soft-glass multimode fibre," Nat. Photonics (2017).

[150] K.-H. Brenner, "Method for designing arbitrary two-dimensional continuous phase elements," Opt. Lett. **25**, 31 (2000).

[151] H. Aagedal, M. Schmid, S. Egner, J. Müller-Quade, T. Beth, and F. Wyrowski, "Analytical beam shaping with application to laser-diode arrays," J. Opt. Soc. Am. A **14**, 1549 (1997).

[152] H. Aagedal, M. Schmid, T. Beth, S. Teiwes, and F. Wyrowski, "Theory of speckles in diffractive optics and its application to beam shaping," J. Mod. Opt **43**, 1409 (1996).

[153] S. Lightman, G. Hurvitz, R. Gvishi, and A. Arie, "Tailoring lens functionality by 3d laser printing," Appl. Opt. **56**, 9038 (2017).

[154] T. Gissibl, S. Thiele, A. Herkommer, and H. Giessen, "Two-photon direct laser writing of ultracompact multi-lens objectives," Nat. Photonics **10**, 554 (2016).

[155] A. Žukauskas, "Improvement of the fabrication accuracy of fiber tip microoptical components via mode field expansion," J Laser Micro Nanoeng **9**, 68 (2014).

[156] K. Weber, F. Hütt, S. Thiele, T. Gissibl, A. Herkommer, and H. Giessen, "Single mode fiber based delivery of OAM light by 3d direct laser writing," Opt. Express **25**, 19672 (2017).

[157] E. E. Morales-Delgado, L. Urio, D. B. Conkey, N. Stasio, D. Psaltis, and C. Moser, "Three-dimensional microfabrication through a multimode optical fiber," Opt. Express **25**, 7031 (2017).

[158] A. Balčytis, D. Hakobyan, M. Gabalis, A. Žukauskas, D. Urbonas, M. Malinauskas, R. Petruškevičius, E. Brasselet, and S. Juodkazis, "Hybrid curved nano-structured micro-optical elements," Opt. Express **24**, 16988 (2016).

[159] C. Bösel and H. Gross, "Ray mapping approach for the efficient design of continuous freeform surfaces," Opt. Express **24**, 14271 (2016).

[160] T. Kaempfe, E.-B. Kley, and A. Tünnermann, "Hybrid approach to the design of refractive beam shaping elements," in "Laser Beam Shaping VI," F. M. Dickey and D. L. Shealy, eds. (SPIE, 2005).

[161] J. R. Fienup, "Reconstruction of an object from the modulus of its fourier transform," Opt. Lett. **3**, 27 (1978).

[162] A. Jesacher, C. Maurer, A. Schwaighofer, S. Bernet, and M. Ritsch-Marte, "Near-perfect hologram reconstruction with a spatial light modulator," Opt. Express **16**, 2597 (2008).

[163] O. Ripoll, V. Kettunen, and H. P. Herzig, "Review of iterative fourier-transform algorithms for beam shaping applications," Opt. Eng. **43**, 2549 (2004).

[164] Y. Shechtman, Y. C. Eldar, O. Cohen, H. N. Chapman, J. Miao, and M. Segev, "Phase retrieval with application to optical imaging: a contemporary overview," IEEE Signal Process. Mag. **32**, 87 (2015).

[165] C. Zhang, Y. Hu, W. Du, P. Wu, S. Rao, Z. Cai, Z. Lao, B. Xu, J. Ni, J. Li, G. Zhao, D. Wu, J. Chu, and K. Sugioka, "Optimized holographic femtosecond laser patterning method towards rapid integration of high-quality functional devices in microchannels," Sci. Rep **6** (2016).

[166] A. L. Gaunt and Z. Hadzibabic, "Robust digital holography for ultracold atom trapping," Sci. Rep **2** (2012).

[167] R. W. Gerchberg and W. Saxton, "A practical algorithm for the determination of the phase from image and diffraction plane pictures," Optik **35**, 237 (1972).

[168] F. Wyrowski and O. Bryngdahl, "Iterative fourier-transform algorithm applied to computer holography," J. Opt. Soc. Am. A **5**, 1058 (1988).

[169] M. T. Gale, M. Rossi, H. Schütz, P. Ehbets, H. P. Herzig, and D. Prongué, "Continuous-relief diffractive optical elements for two-dimensional array generation," Appl. Opt. **32**, 2526 (1993).

[170] E.-B. Kley, M. Cumme, L.-C. Wittig, and A. Tünnermann, "Fabrication and properties of refractive micro-optical profiles for lenses, lens arrays and beam shaping elements," in "Advanced Optical Manufacturing and Testing Technology 2000," , vol. 4231 (SPIE, 2000), vol. 4231, p. 144.

[171] R. M. Goldstein, H. A. Zebker, and C. L. Werner, "Satellite radar interferometry: Two-dimensional phase unwrapping," Radio Science **23**, 713–720 (1988).

[172] J. W. Goodman, *Introduction to Fourier optics* (Roberts and Company Publishers, 2005).

[173] J.-B. Kim and K.-H. Jeong, "Batch fabrication of functional optical elements on a fiber facet using dmd based maskless lithography," Opt. Express **25**, 16854 (2017).

[174] B. Boehme and H. Gross, "Characterization of complex optical systems based on wavefront retrieval from point spread function," in "Optical Systems Design 2005," (International Society for Optics and Photonics, 2005), p. 596515.

[175] R. W. Boyd, *Nonlinear optics* (Academic press, 2003).

[176] H.-B. Sun and S. Kawata, "Two-photon photopolymerization and 3d lithographic micro-fabrication," Adv. Polym. Sci. **170**, 169 (2004).

[177] W. Singer, M. Totzeck, and H. Gross, *Handbook of Optical Systems*, vol. 2 (Wiley-VCH, 2005).

Appendices

A Derivation of the WPM algorithm

The WPM and the different BPMs describe the evolution of a field in space unidirectionally along a preferred direction, i.e., the z-axis, while neglecting backward propagating field components. The governing equations, which describe the scalar field evolution, are derived from the Helmholtz Equation

$$\begin{aligned} \left(\Delta + k_0^2\, n^2(x,y,z)\right)\, E &= 0 \quad , \\ \left(\partial_z^2 + \underbrace{\Delta_T + k_0^2\, n^2(x,y,z)}_{\mathcal{H}_T}\right)\, E &= 0 \quad , \\ \mathcal{H}_T &= \text{transverse Helmholtz operator} \quad , \end{aligned}$$

while splitting it into forward and backward propagating field components [45, 46]

$$\left(i\sqrt{\mathcal{H}_T} + \partial_z\right)\, \left(i\sqrt{\mathcal{H}_T} - \partial_z\right)\, E = 0 \; . \tag{A1}$$

Here, the square root Helmholtz operator $\sqrt{\mathcal{H}_T}$ is introduced, being formally defined in terms of a power-series. Moreover, it is assumed that the commutator $[\partial_z, \sqrt{\mathcal{H}_T}]$ can be neglected, which physically concludes the fact that back reflections within the inhomogeneous medium need not to be considered. Then, the forward Helmholtz-Equation can be rewritten as

$$\partial_z E = i\sqrt{\mathcal{H}_T} E \; , \tag{A2}$$

which obeys a formal solution according to

$$E(x,y,z_0+z) = e^{iz\sqrt{\mathcal{H}_T}} E(x,y,z_0) \; . \tag{A3}$$

On the one hand, the different BPMs can be derived by either expanding the square-root operator in Eqn. A2 or directly the exponential operator in Eqn. A3 into a Padé-series [48,54]. Depending upon the truncation order, the different formulations are distinguished. On the other hand, the WPM suggests to approximate the exponential operator in Eqn. A3 by an integral operator

$$\begin{aligned} E(x,y,z+\Delta z) &= \frac{1}{2\pi} \int \tilde{E}(k_x,k_y,z)\, e^{ik_z(k_x,k_y,x,y)\Delta z}\, e^{i(k_x x + k_y y)}\, dk_x\, dk_y \quad , \\ \tilde{E}(k_x,k_y,z) &= \frac{1}{2\pi} \int E(x,y,z)\, e^{-i(k_x x + k_y y)}\, dx\, dy \quad , \\ k_z(k_x,k_y,x,y) &= \sqrt{k_0^2 n^2\left(x,y,z+\tfrac{\Delta z}{2}\right) - {k_x}^2 - {k_y}^2} \; . \end{aligned}$$

A derivation of the algorithm can be performed with the aid of pseudo-differential operators PDO as outlined in [77–79]. In the following for simplicity with the calculations, they are restricted to only one transverse dimension. All the derivations can be extended for two transverse dimensions straightforward. The theory of PDO was introduced to study the properties of linear partial differential operators with non-constant coefficients in the form of $\mathcal{P} = \sum_m c_m(x)\partial_x^m$. By

introducing the Fourier-transformed field $u(x) = \frac{1}{\sqrt{2\pi}} \int \tilde{u}(k_x) e^{i(k_x x)} dk_x$, the application of the operator on $u(x)$ becomes

$$\begin{aligned}
\mathcal{P}\{u(x)\} &= \left(\sum_m c_m(x)\partial_x^m\right) \frac{1}{\sqrt{2\pi}} \int \tilde{u}(k_x)\, e^{i(k_x x)} dk_x \\
&= \frac{1}{\sqrt{2\pi}} \int \sum_m c_m(x)\, i^m\, k_x^m \underbrace{\tilde{u}(k_x)}_{\frac{1}{\sqrt{2\pi}}\int u(\tilde{x}) e^{-i(k_x\tilde{x})} d\tilde{x}} e^{i(k_x x)} dk_x \\
&= \frac{1}{2\pi} \iint \left(\sum_m c_m(x)\, i^m\, k_x^m\; u(\tilde{x}) e^{i(k_x(x-\tilde{x}))}\right) d\tilde{x} dk_x \\
&= \frac{1}{2\pi} \iint \left(p(x,k_x)\; u(\tilde{x}) e^{i(k_x(x-\tilde{x}))}\right) d\tilde{x} dk_x \qquad \text{(A4)}
\end{aligned}$$

The expression $p(x,k_x) = \sum_m c_m(x)\, i^m\, k_x^m$ is called the symbol of the operator $\mathcal{P}$. It is a polynomial of spatial frequencies k_x with coefficients depending on x. In case the symbol $p(x,k_x)$ is independent of x, Eqn. A4 reduces to the well known representation of a differential operator with constant coefficients in the Fourier-domain

$$\mathcal{P}\{u\} = \mathcal{F}^{-1}\left\{p(k_x)\mathcal{F}\left\{u(x)\right\}\right\} \ .$$

In the following, the specific case to derive the symbol $k_z^{sym}(x,k_x)$ related to the square root operator $\sqrt{\mathcal{H}_T} = \sqrt{k_0^2 n^2(x) + \partial_x^2}$ will be discussed. The symbol for the Helmholtz-Operator $\mathcal{H}_T$ is given as $h_T = k_0^2 n^2(x) - k_x^2$. To conclude onto the unknown symbol of the square root operator $\sqrt{\mathcal{H}_T}$ the calculations start from the identity $\sqrt{\mathcal{H}_T}\left\{\sqrt{\mathcal{H}_T}\left\{u\right\}\right\} \stackrel{!}{=} \mathcal{H}_T\left\{u\right\}$ and calculate the symbol of the composition of two operators $\mathcal{P}\left\{\mathcal{P}\left\{u(x)\right\}\right\}$.

$$\begin{aligned}
\mathcal{P}\left\{\mathcal{P}\left\{u(x)\right\}\right\} &= \frac{1}{2\pi} \iint\; p(x,k_x)\{\mathcal{P}\left\{u(x)\right\}\quad e^{i(k_x(x-x'))} dx' dk_x \\
&= \frac{1}{4\pi^2} \iiint\!\!\int p(x,k_x)\left(p(x',k_x') u(\tilde{x}) e^{ik_x'(x'-\tilde{x})}\right) + e^{k_x(x-x')} dx' dk_x d\tilde{x} dk_x' \\
&= \frac{1}{4\pi^2} \iint \left(\iint p(x,k_x) p(x',k_x') e^{-i(k_x'-k_x)(x-x')} dx' dk_x\right) u(\tilde{x}) e^{ik_x'(x-\tilde{x})} d\tilde{x} dk_x'. \qquad \text{(A5)}
\end{aligned}$$

In Eqn. A5 the symbol, which usually is referred to as $(p\#p)(x,k_x)$, of the composition operator $\mathcal{P}\left\{\mathcal{P}\left\{u\right\}\right\}$ can be identified with

$$(p\#p)(x,k_x) = \iint p(x,k_x) p(x',k_x') e^{-i(k_x-k_x')(x-x')} dx' dk_x' \stackrel{!}{=} h_T(x,k_x) \quad .$$

This integral expression, according to the theory of pseudo-differential operators, can be replaced by the equivalent expression [77]

$$\begin{aligned}
(p\#p)(x,k_x) &= \sum_{m=0}^{\infty} \frac{1}{i^m m!} \partial_{k_x}^m p(x,k_x) \partial_x^m p(x,k_x) \qquad \text{(A6)} \\
&= p(x,k_x)^2 \;-\; i\,\partial_x p(x,k_x) \partial_{k_x} p(x,k_x) + \sum_{m=2}^{\infty} \frac{1}{i^m\, m!} \partial_{k_x}^m p(x,k_x) \partial_x^m p(x,k_x) \quad .
\end{aligned}$$

This result can be applied for the discussion of the symbol $k_z^{sym}(x,k_x)$ related to the square root operator $\sqrt{\mathcal{H}_T}$ in Eqn. A3. In case the refractive index is constant $n(x,y) = n_0$ the symbol

related to the square root operator is given as $k_z^{sym}(x,k_x)=\sqrt{k_0^2n^2-k_x^2}$, which can be proven with the help of Eqn. A6. Therefore the final solution to propagate an initial field $E(x,z_0)$ reads as

$$\begin{aligned} E(x,z_0+\Delta z) &= \frac{1}{\sqrt{2\pi}}\int e^{i\sqrt{k_0^2n_0^2-k_x^2}\ \Delta z}\tilde{E}(k_x,z_0)e^{i(k_xx)}dk_x \quad , \\ \tilde{E}(k_x) &= \frac{1}{\sqrt{2\pi}}\int E(x,z_0)e^{-i(k_xx)}dx \quad . \end{aligned}$$

This resembles the well known angular spectrum of plane wave decomposition.
If the refractive index is not constant and varying along the transverse dimension, the symbol $k_z(x,k_x)=\sqrt{k_0^2n^2(x)-k_x^2}$ describes the leading order within the expansion in Eqn. A6. The leading error by approximating the symbol $k_z^{sym}(x,k_x)$ by $k_z(x,k_x)$ is then given as

$$\begin{aligned} \Delta k_z(x,k_x) &= \frac{(k_z\#k_z)(x,k_x)-h_T}{k_z(x,k_x)} \\ &= \frac{-i\,\partial_x k_z(x,k_x)\,\partial_{k_x}k_z(x,k_x)}{k_z(x,k_y)}+\frac{1}{k_z(x,k_x)}\sum_{m=2}\frac{1}{i^m\,m!}\partial_{k_x}^m k_z(x,k_x)\partial_x^m k_z(x,k_x) \\ &= i\,\frac{k_xk_0^2n(x)\partial_x n(x)}{k_z(x,k_x)^{\,3}}+\frac{1}{k_z(x,k_x)}\sum_{m=2}\frac{1}{i^m\,m!}\partial_{k_x}^m k_z(x,k_x)\partial_x^m k_z(x,k_x). \end{aligned} \tag{A7}$$

Therefore the leading error contribution is given as $\Delta {k_z}^0(x,k_x)=i\,\frac{k_xk_0^2n(x)\partial_x n(x)}{k_z(x,k_x)^{\,3}}$, which is an amplitude term for propagating waves characterized by $\Im\{k_z\}=0$. Therefore the phase propagation within the WPM is upto 2^{nd} order correct. Moreover, relying on this approach, more accurate derivations of the symbol related to the square-root operator $\sqrt{\mathcal{H}_T}$ can be derived on the base of a perturbation series [79].

B Propagation of harmonic light fields in a rotationally symmetric coordinate frame

An initial scalar light field $\mathcal{E}(x, y, z = 0, t) = E(x, y, z = 0)\, e^{-i\,\omega\, t}$, characterized by the frequency ω, is propagated inside a homogeneous medium specified by a refractive index n with the angular spectrum of plane wave decomposition in a rigorous way [177]. By introducing the Fourier transform and its inverse

$$\begin{aligned} \tilde{E}(k_x, k_y, z = 0) &= \mathcal{F}_{x,y}\{E(x, y, z = 0)\} \\ &= \frac{1}{2\pi} \iint E(x, y, z = 0)\, e^{-i(k_x x + k_y y)}\, dk_x\, dk_y \\ E(x, y, z = 0) &= \mathcal{F}^{-1}_{k_x,k_y}\{\tilde{E}(k_x, k_y, z = 0)\} \\ &= \frac{1}{2\pi} \iint \tilde{E}(k_x, k_y, z = 0)\, e^{i(k_x x + k_y y)}\, dx\, dy \end{aligned}$$

the field evolution is described by

$$\begin{aligned} E(x, y, z) &= \mathcal{F}^{-1}_{k_x,k_y}\{\mathcal{F}_{x,y}\{E(x, y, z = 0)\} e^{ik_z(k_x,k_y)z}\}, \\ k_z(k_x, k_y) &= \sqrt{{k_0}^2 n^2 - {k_x}^2 - {k_y}^2}. \end{aligned}$$

To describe also the field evolution in a rotationally symmetric coordinate frame the Fourier-transforms have to be evaluated in these coordinates. Therefore, the initial field is assumed to be decomposed into angular harmonics

$$\begin{aligned} E \quad & (x = r\cos(\varphi), y = r\sin(\varphi), z = 0) = \\ E \quad & (r, \varphi, z = 0) = \sum_{m=-\infty}^{\infty} E_m(r, z = 0) e^{im\varphi}, \end{aligned} \tag{A1}$$

where the individual $E_m(r, z = 0)$ are given as

$$E_m(r, z = 0) = \frac{1}{2\pi} \int_{-\pi}^{\pi} E(r, \varphi, z = 0) e^{-im\varphi}\, d\varphi\ .$$

Then the Fourier-transformed field

$$\tilde{E}(k_x = k_r\cos(k_\varphi), k_y = k_r\sin(k_\varphi), z = 0)$$

and its inverse are given as

$$\begin{aligned}
\tilde{E}(k_r, k_\varphi, z=0) &= \sum_{m=-\infty}^{\infty} \tilde{E}_m(k_r, z=0) e^{imk_\varphi} \ , \\
&= \sum_{m=-\infty}^{\infty} (-i)^m \, e^{imk_\varphi} \mathcal{H}_m\{E_m(r, z=0)\} \ , \\
\mathcal{H}_m\{E_m(r, z=0)\} &= \int_0^\infty E_m(r, z=0) \, J_m(k_r \, r) \, r \, dr \ , \\
E(r, \varphi, z=0) &= \sum_{m=-\infty}^{\infty} i^m \, e^{im\varphi} \mathcal{H}_m^{-1}\{\tilde{E}_m(k_r, z=0)\} \ , \\
\mathcal{H}_m^{-1}\{E_m(k_r, z=0)\} &= \int_0^\infty E_m(r, z=0) \, J_m(k_r \, r) \, k_r \, dk_r \ .
\end{aligned}$$

Here $\mathcal{H}_m\{E_m(r)\}$ and $\mathcal{H}_m^{-1}\{E_m(k_r)\}$ are respectively the Hankel-transform of order m and its inverse. The propagation of the light field then is described as

$$\begin{aligned}
E(r, \varphi, z) &= \sum_{m=-\infty}^{\infty} e^{im\varphi} \mathcal{H}_m^{-1}\{\mathcal{H}_m\{E_m(r, z=0)\} e^{ik_z z}\}, \\
k_z(k_r) &= \sqrt{{k_0}^2 n^2 - {k_r}^2} \ .
\end{aligned} \tag{A2}$$

Within Eqn. A2 a summation over angular harmonics occurs, which has to be truncated for numerical reasons. This truncation number strongly depends on the investigated scenario. For instance, the decomposition of a plane wave of the form $e^{ik_x x}$ into angular harmonics is described analytically by the Jacobi-Anger relations

$$e^{ik_x x} = e^{ik_x r \cos(\varphi)} = \sum_{m=-\infty}^{\infty} i^m J_m(k_x r) e^{im\varphi} \quad . \tag{A3}$$

In this case, the truncation order depends upon the propagation angle of the plane wave and the size of the computational domain. To this end, in Fig. B.1 the relative RMS-deviation

$$\mathrm{RMS} = \frac{\sqrt{\int_{-\frac{w}{2}}^{\frac{w}{2}} \left| e^{ik_x x} - \sum_{m=-M}^{M} i^m J_m(k_x r) e^{im\varphi} \right|^2}}{\sqrt{\int_{-\frac{w}{2}}^{\frac{w}{2}} \left| e^{ik_x x} \right|^2}}$$

is shown for varying widths w of the computational domain for a plane wave of wavelength $\lambda = 1\mu\mathrm{m}$ with a numerical aperture of NA$= \frac{k_x}{k_0} = 0.1$. The maximum order M which needs to be considered within the expansion of Eqn. 2.8 is growing with the overall size of the computational domain. Therewith, of course, also the computational effort rises. As a consequence, the applicability of the Hankel-WPM in general strongly depends upon an explicit scenario to be investigated.

However, often initial light fields obey an underlying rotational symmetry, which decreases the number of angular harmonics substantially. This is the case for fields that propagate parallel

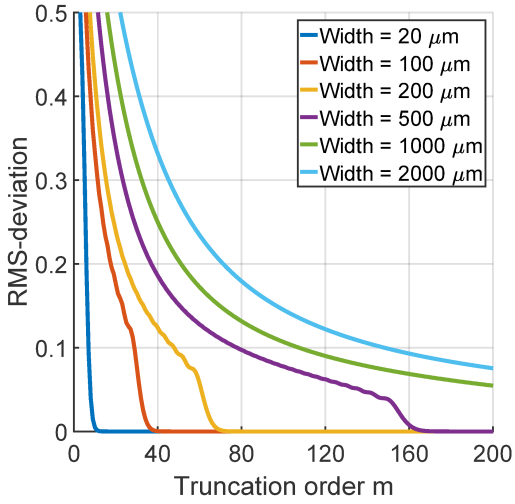

Figure B.1: Deviation between the Jacobi-Anger relation of truncation order M from a plane wave with numerical aperture NA= $\frac{k_x}{k_0} = 0.1$ for varying widths of the computational domain.

to the optical axis such as a gaussian beam. Moreover, the fields emitted by optical fibers are typically characterized by a low number of angular harmonics.

C Publications

Journal articles

1 S. Schmidt, T. Tiess, S. Schröter, R. Hambach, M. Jäger, H. Bartelt, A. Tünnermann, and H. Gross "*Wave-optical modeling beyond the thin-element-approximation*" in Opt. Express **24**, 30188 (2016)

2 S. Schmidt, S. Thiele, A. Herkommer, and H. Gross, "*Rotationally symmetric formulation of the wave propagation method - application to the straylight analysis of diffractive lenses*", in Opt. Lett. **42**, 1612 (2017)

3 S. Schmidt, T. Tiess, S. Schröter, A. Schwuchow, M. Jäger, H. Bartelt, A. Tünnermann, and H. Gross "*Noninvasive characterization of optical fibers*" in Opt. Lett. **42**, 4946 (2017)

Manuscripts in preparation

4 S. Schmidt, S. Thiele, A. Herkommer, A. Tünnermann, H. Giessen, and H. Gross "*3D freeform holograms on fiber tips*", manuscript prepared

5 T. Elsmann, S. Schmidt, A. Lorenz, J. Fiebrandt, A. Schwuchow, M. Rothhardt, H. Gross, and H. Bartelt "*Fiber induced field enhancement inside a fiber during fiber Bragg grating inscription*", manuscript in preparation

Journal articles not directly related to this thesis

6 S. Schmidt, A. E. Klein, T. Paul, H. Gross, S. Diziain, M. Steinert, A. C. Assafrao, T. Pertsch, H. P. Urbach, and C. Rockstuhl "*Image formation properties and inverse imaging problem in aperture based scanning near field optical microscopy*", in Opt. Express **24**, 4128 (2016)

7 A. E. Klein, N. Janunts, S. Schmidt, S. B. Hasan, C. Etrich, S. Fasold, T. Kaiser, C. Rockstuhl, and T. Pertsch "*Dual-SNOM investigations of multimode interference in plasmonic strip waveguides*", in Nanoscale **9**, 6695 (2017)

Patent applications in preparation

1 A patent application is planned regarding the integrated beam shaping concept.

International conferences

1 S. Schmidt, T. Paul, and H. Gross "*Assessment of the wave propagation method for the simulation of micro-lenses* ", Oral presentation, in EOS Conference on Light Engineering (EOSLE), Munich (2015)

2 S. Schmidt, U. Lippmann, M. M. Guenther, and H. Gross "*Diffraction effects in laser beam shaping systems*", Oral presentation, SPIE Optical Systems Design, Jena (2015)

3 N. Janunts, A. Klein, S. Schmidt, S. Bin Hasan, C. Etrich, S. Fasold, T. Kaiser, C. Rockstuhl, A. Tünnermann, and T. Pertsch "*Polarization-Sensitive Dual-SNOM for Investigation of Plasmonic Propagation*", Conference on Surface Plasmon Photonics SPP7, Tel Aviv (2015)

4 S. Thiele, K. Arzenbacher, T. Gissibl, S. Schmidt, H. Gross, H. Giessen, and A.M. Herkommer "*Design, simulation and 3D printing of complex micro-optics for imaging*", International Conference on Optical MEMS and Nanophotonics (OMN), Singapore (2016)

5 S. Schmidt, T. Tiess, S. Schröter, and H. Gross "*Numerical and experimental evaluation of inline holographic measurements for the metrology of optical fibers*", Oral presentation, European Optical Society Annual Meeting (EOSAM) 2016, Berlin (2016)

6 S. Schmidt, S. Thiele, A. Herkommer, and H. Gross "*Integrated point spread function engineering*", Poster presentation, 634. WE-Heraeus-Seminar: Merging Micro- and Nano-Optics: 3D Printing for Advanced and Functional Optics, Bad Honnef, (2017)

7 S. Schmidt, T. Tiess, S. Schröter, and H. Gross "*Inverse scattering approach to characterize capillary optical fibers*", Oral presentation, OSA Imaging and Applied Optics Congress, San Francisco, (2017)

8 S. Schmidt, S. Thiele, A. Herkommer, H. Giessen, and H. Gross "*Integrated approach to realize top hat focal field distributions*", Poster presentation, OSA Imaging and Applied Optics Congress, San Francisco, (2017)

D Curriculum Vitae

Persönliche Daten

Name	Sören Schmidt
Geburtsdatum	03.08.1987
Geburtsort	Schleiz

Ausbildung und wissenschaftlicher Werdegang

1994-1998	Grundschule Oettersdorf
1998-2006	Dr.-Konrad-Duden-Gymnasium Schleiz
Juni 2006	Abitur
2006-2007	Work-and-Travel Neuseeland
2007-2010	Bachelorstudium Physik an der Friedrich-Schiller-Universität Jena
Sept. 2010	B.Sc. in Physik
2010-2013	Masterstudium Physik an der Friedrich-Schiller-Universität Jena
Aug. 2013	M.Sc. in Physik
2013-2018	Wissenschaftlicher Mitarbeiter am Fraunhofer-Institut für Angewandte Optik und Feinmechanik, AG Optisches Design - Prof. Dr. Herbert Gross

Jena, den 5. August 2018

Sören Schmidt

E Ehrenwörtliche Erklärung

Ich erkläre hiermit ehrenwörtlich, dass ich die vorliegende Arbeit selbständig, ohne unzulässige Hilfe Dritter und ohne Benutzung anderer als der angegebenen Hilfsmittel und Literatur angefertigt habe. Die aus anderen Quellen direkt oder indirekt übernommenen Daten und Konzepte sind unter Angabe der Quelle gekennzeichnet.

Bei der Auswahl und Auswertung folgenden Materials haben mir die nachstehend aufgeführten Personen in der jeweils beschriebenen Weise unentgeltlich geholfen:

- Prof. Dr. Herbert Gross hat das Promotionsvorhaben betreut und in diesem Rahmen die in der Arbeit dargestellten Themen sowie die Dissertationsschrift mit mir diskutiert.
- Das rotationssymmetrische COMSOL-Modell, welches zur Simulation diffraktiver Linsen verwendet wurde, ist von Simon Thiele aus der Gruppe von Prof. Herkommer (Institut für Technische Optik, Universität Stuttgart) entwickelt worden.
- Das Modell zur Beschreibung und Analyse der Beam-Propagation-Methods in Kapitel 2.3.1 wurde zusammen mit Asis Saad Rodriguez im Rahmen einer Qualifizierungsarbeit (Research Labwork) entwickelt.
- Die Implementierung der numerischen Hankel-Transformation basiert auf den öffentlich zur Verfügung gestellten Programmen von Marcel Leutenegger (https://documents.epfl.ch/users/l/le/leuteneg/www/MATLABToolbox/HankelTransform.html)
- Die experimentellen Messungen zur Untersuchung der Glasmatrixstörungen während des Einschreibens von Faser-Bragg-Gittern wurden von Tino Elsmann und Adrian Lorenz aus der Gruppe von Prof. Bartelt (Leibniz Institute of Photonic Technology (IPHT), Jena) vorgenommen. Dies umfasst die Einschreibevorgänge der Faser-Bragg-Gitter und die mikroskopischen Vermessungen der Fasern.
- Die experimentellen Aufbauten zur in-line holografischen Vermessung optischer Fasern wurden von Tobias Tieß und Siegmund Schröter aus der Gruppe von Prof. Bartelt (Leibniz Institute of Photonic Technology (IPHT), Jena) vorgenommen. Die einzelnen Messungen wurden gemeinsam mit Tobias Tieß durchgeführt.
- Die gesamte experimentelle Realisierung und Charakterisierung des integrierten Strahlformungskonzeptes in Kapitel 5 wurde von Simon Thiele aus der Gruppe von Prof. Herkommer (Institut für Technische Optik, Universität Stuttgart) durchgeführt. Dies umfasst insbesondere die *(i)* Realisierung der Freiformhologramme auf Faserstirnflächen, *(ii)* die Vermessung realisierter Oberflächen, *(iii)* die mikroskopischen Messungen erzeugter Feldverteilungen.
- Im Übrigen waren jeweils die Koautoren der angeführten Veröffentlichungen (s. Anhang "Publications") an der Interpretation und der Diskussion der Ergebnisse beteiligt.

Weitere Personen waren an der inhaltlich-materiellen Erstellung der vorliegenden Arbeit nicht beteiligt. Insbesondere habe ich hierfür nicht die entgeltliche Hilfe von Vermittlungs- bzw. Beratungsdiensten (Promotionsberater oder andere Personen) in Anspruch genommen. Niemand hat von mir unmittelbar oder mittelbar geldwerte Leistungen für die Arbeiten erhalten, die im Zusammenhang mit dem Inhalt der vorgelegten Dissertation stehen. Die Arbeit wurde bisher weder im In- noch im Ausland in gleicher oder ähnlicher Form einer anderen Prüfungsbehörde vorgelegt. Die geltende Prüfungsordnung der Physikalisch-Astronomischen Fakultät ist mir bekannt. Ich versichere ehrenwörtlich, dass ich nach bestem Wissen die reine Wahrheit gesagt und nichts verschwiegen habe.

Jena, den 5. August 2018

Sören Schmidt

F Danksagung

Mit dem Schreiben dieser letzten Zeilen, blicke ich zurück auf die letzten viereinhalb Jahre der Arbeit an dieser Dissertation und auf all die Personen die mich hierbei unterstützt und begleitet haben. Viele der vorgestellten Ergebnisse in dieser Arbeit wäre ohne die Unterstützung von vielen Seiten nicht möglich gewesen. Oftmals waren es einzelne Diskussionen, die den Blickwinkel auf verschiedene Probleme änderten und damit neue Wege eröffnen konnten. Darüber hinaus war es die gemeinsame Arbeit in den Kollaborationen, die aus groben Ideen echte Ergebnisse machten. Aber auch neben der eigentlichen Arbeit, waren es all die gemeinsamen Abende mit Freunden und der Familie, die dafür sorgten, dass man immer den nötigen Abstand zur eigenen Arbeit wahrt. Ich möchte mich daher bei allen bedanken, die mich innerhalb der letzten viereinhalb Jahre unterstützt haben.

Allen voran möchte ich mich bei Herbert Gross für die Chance bedanken meine Dissertation in der Gruppe "Optical System Design" schreiben zu können. Ich möchte mich bei dir für all das entgegengebrachte Vertrauen bedanken; Für die Möglichkeit meine Thematik weitgehend frei entwickeln zu können und in dieser offenen Arbeitsatmosphäre eigene Ideen umsetzen zu können. Gleichzeitig war deine Tür stets geöffnet und du hattest ein offenes Ohr, um Probleme zu diskutieren. Ich möchte mich auch dafür bedanken, dass ich in meiner Zeit viel über klassisches Optikdesign lernen konnte, obwohl mein eigenes Arbeitsthema doch relativ weit davon entfernt war. Es ist nicht selbstverständlich, dass du dir immer wieder die Zeit genommen hast, uns Doktoranden in den "Zemax-Seminaren" auch für die Zeit außerhalb der Universitätswände vorzubereiten.

Ein Großteil dieser Arbeit wäre ohne dem gemeinsamen Zusammenspiel mit großartigen Kollaborationspartnern unmöglich gewesen. Es war immer eine äußerst konstruktive Zusammenarbeit, die nicht davon geprägt war schnelle Ergebnisse zu erzeugen. Vielmehr ging es darum Zusammenhänge zu verstehen und zu ergründen, um damit die eigentlichen Ergebnisse stets zu verbessern. Ich möchte mich hierfür zuerst bei allen Kollegen am IPHT in Jena bedanken. Bei Siegmund, Tino, Adrian und Anka für jeden Rat und die gemeinsamen Messungen und Untersuchungen an den verschiedensten Fasern. Es war ein faszinierender Einblick zu sehen, was hier alles möglich ist. Ich möchte mich bei Prof. Hartmut Bartelt und Dr. Matthias Jäger bedanken für die Unterstützung bei all den Experimenten zur Charakterisierung optischer Fasern. Zuletzt möchte ich mich noch bei Tobi bedanken. Ohne deine Bereitschaft und deine Initiative wäre unser gemeinsames Projekt der Fasercharakterisierung sicher nie entstanden. Du hast dir immer die Zeit genommen unsere Ideen voran zu treiben, obwohl du eigentlich nie die Zeit dazu hattest. Auch abseits unserer gemeinsamen Arbeit standest du immer mit Rat und Tat zur Seite und hast neue gemeinsame Projekte initiiert. Diese Dissertation wäre ohne deine Hilfe nie in dieser Art und Weise entstanden - Vielen Dank!

Ich möchte mich auch bei Simon Thiele, Prof. Harald Giessen und Prof. Alois Herkommer von der Universität in Stuttgart bedanken. Es war die äußerst konstruktive und offene Arbeitsatmosphäre, die viele Ergebnisse erst möglich gemacht hat. Vieles hat sich sehr dynamisch entwickelt und die vielen konstruktiven Ideen haben immer neue Möglichkeiten und Wege aufgezeigt.

Mein ganz besonderer Dank gilt Simon - Es ist faszinierend zu sehen, wie sich unser Projekt der integrierten Strahlformung innerhalb der letzten eineinhalb Jahre entwickelt hat. Wie sich aus einer ersten Mail mit "*Wir hatten ja schon seit längerem die Idee einmal etwas gemeinsam zu machen.*" eine Eigendynamik entwickelte und wir mittlerweile sagen können, den weltweit kleinsten "Diaprojektor" realisiert zu haben. Nicht alles hat von Anfang an funktioniert und es mussten viele Steine aus dem Weg geräumt werden. Dies hat die Arbeit nie ausgebremst, sondern war vielmehr Ansporn diese Herausforderungen zu bewältigen. Unsere Diskussionen waren hier immer aufschlussreich und es sind dabei stets neue Ideen entstanden, um die einzelnen Probleme anzugehen.

Ein großes Dankeschön geht auch an die gesamte Optik-Design Gruppe in Jena für die schöne Zeit hier und den gemeinsamen Austausch verschiedenster Ideen. Ein großer Dank geht insbesondere an Ralf. Du hast dir immer die Zeit für verschiedenste Diskussionen genommen und warst eine große Stütze im Erstellen dieser Arbeit. Ich möchte mich auch bei allen Kollegen am IOF bedanken. Bei Gunther für die Möglichkeit ein Teil der A2 zu sein und bei Uwe, Britta und Conni für all die schönen Diskussionen bei euch im Büro. Darüber hinaus möchte ich mich auch bei der gesamten Mittagsrunde für all die erhellenden Einsichten bedanken. Basti, Tobi, Ralf, Johannes und Christoph - Dank euch weiß ich, dass ein offenes Autofenster eine ganze Klimaanlage ersetzen kann; ein 5:0 Kantersieg im Hinspiel die denkbar schlechteste Ausgangslage für ein Rückspiel ist und Gurkenwasser die Antwort auf alles ist.

Die Erstellung einer Dissertation wäre sicher auch nie möglich gewesen ohne den Rückhalt von Freunden und all die wunderbare Zeit, die wir gemeinsam verbringen konnten. Diese Zeit mit euch, all die Ausflüge, die gemeinsamen Abende und das gemeinsame Lachen lassen den gewöhnlichen Arbeitsalltag vergessen und ermöglichen es sich den besten Seiten des Lebens zu widmen. Mein größter Dank geht an Herry, Tobi, Robert, Marvin, Christin, Manuel, Mandy, Janek und Anne; Die gesamte 3G-Crew, die Löhmaer und die beste Burgercrew aka die beste Fluffcrew.

Jetzt, am Ende der Danksagung, kommt der wohl wichtigste Teil - Ich möchte meiner Familie danken. Liebe Eltern, vielen Dank für all die Unterstützung, die Geduld und die Nachsicht in so vielen Etappen meines Lebens. Vielen Dank, dass Ihr mein Studium ermöglicht habt und immer bei allen Fragen mit Rat und Tat zur Seite standet.

Zum Schluss - es ist schwer hier die richtigen Worte zu finden - Liebe Claudi, vielen Dank für einfach alles; für all die Unterstützung und die wunderbare gemeinsame Zeit.